Physik-Department
der Technischen Universität München
Lehrstuhl für Biophysik E22

Wetting and Interdiffusion: Establishment of a Bio-compatible System and Studies of its Dynamics

Anja-Katrin Prechtel

Vollständiger Abdruck der von der Fakultät für Physik der Technischen Universität München zur Erlangung des akademischen Grades eines

Doktors der Naturwissenschaften (Dr. rer. nat.)

genehmigten Dissertation.

Vorsitzender:		Univ.-Prof. Dr. M. Kleber
Prüfer der Dissertation:	1.	Univ.-Prof. Dr. M. Rief
	2.	Univ.-Prof. Dr. R. Merkel, Rheinische Friedrich-Wilhelms-Universität Bonn

Die Dissertation wurde am 31.05.2005 bei der Technischen Universität München eingereicht und durch die Fakultät für Physik am 12.07.2005 angenommen.

Contents

List of Figures

List of Tables

I know it is wet
And the sun is not sunny.
But we can have
Lots of good fun that is funny!

Dr. Seuss

Chapter 1

Abstract

The final goal of this work was to introduce a fluid substrate for future studies with living cells. Such a substrate would offer unique possibilities for quantitative investigations as fluid surfaces exhibit no static surface defects. Wetting of fluids on transparent substrates in ambient water was employed to realize such a substrate. The fluid must be insoluble in water and bio-compatible. As no studies on comparable systems were available, a suitable combination of fluid and substrate had to be identified first. In a next step, its wetting behavior had to be investigated in detail. Here static and dynamic aspects as well as material interdiffusion turned out to be important aspects.

The search for a suitable system was challenging. It was observed that under water most combinations of fluid and substrate exhibited quite large contact angles, i.e. only partial wetting occurred. Finally polydimethylsiloxane (PDMS) oil on a substrate covered with a thin film of cross-linked PDMS was identified as the most promising system. This system was found to be close to its wetting transition. As bio-compatibility is of utmost importance for future applications, the effects of PDMS oils on cultivated endothelial cells from human umbilical cord were tested. No adverse effects on these delicate cells were observed.

PDMS drops on solid substrates were observed using optical reflection interference contrast microscopy (RICM) which is an accurate technique for the determination of the shapes of micron sized objects. This technique had to be optimized for the reconstruction of drop shapes. Moreover, a detailed evaluation of the resolution and a rigorous error analysis were performed.

For meaningful experiments droplets smaller than the field of view of the microscope ($\sim$100 μm) had to be deposited onto the substrate. Such tiny droplets exhibiting picoliter volumes were applied using a semi-automated micro-injector. Within seconds after deposition the droplets adopted the shape of a spherical cap and remained so during their further evolution. This shape is in full accord with theory. Following deposition the oil spread on the surface which resulted in decreasing contact angles. At the same time, the droplets lost volume. This lead to a remarkable behavior of the drop base area. After a steady increase, the drop bases shrank again before the drops finally vanished.

Employing fluorescence labelled PDMS oil as tracer, diffusion of oil into the cross-linked PDMS film was identified as reason for the volume loss. The diffusion constants of PDMS oil in the pure phase and within the cross-linked substrate were determined by photobleaching experiments. Both diffusion constants agreed well with literature values. Based on these data a quantitative description of the volume loss was approached.

Unfortunately, the diffusion equation cannot be solved analytically for this situation which is greatly complicated by the movement of the drop base. However, for short times when the drop base radius is essentially stationary, an existing semi-analytical solution can be used. This approximate solution described the data quantitatively for up to two decades of time without any adjustable parameter. To model the volume loss during the entire evolution of the droplets, a numerical simulation of the diffusion process was implemented. Here major problems with numerical instabilities were encountered. These originated from the high sensitivity of diffusion processes on boundary conditions and are also well documented in literature. Nevertheless it was possible to reproduce the overall kinetics of the volume loss over several orders of magnitude in time.

As the droplets evolved, their contact angles decreased. This could be described by a power law with exponents of approximately 0.3 and 0.05 for two different substrates of cross-linked PDMS. Moreover, it was observed that simultaneously with the reversal of the drop base motion from advancing to receding the contact angles went through a minimum at values of about 1°. This behavior was not seen before and could be attributed to the diffusion of polymers into the substrate and the accompanying gradient of the chemical potential of the polymers.

In conclusion, it was found that PDMS oil on cross-linked PDMS films exhibits a rich wetting dynamics driven by the interplay of spreading on the substrate and diffusion into it.

Chapter 2

Motivation

There are many aspects of the interaction between solids and fluids, and their applications are everywhere. Paint that forms a homogenous layer even on smooth plastic surfaces, non-stick pans, and anti-graffiti coatings that mimic the self-cleansing properties of plant leaves, are just a few examples of a whole range of applications that are common to our everyday lives.

Scientific attention to the interaction between solid surfaces and liquids first sprang up in the early nineteenth century. It was then that famous physicists such as Gibbs and Young addressed this issue and started a thriving field of science that is still in lively discussion [Gibbs, 1928; Young, 1805].

They developed the concept of the interfacial energy γ, also known as interfacial tension, which is defined as the free energy necessary to increase the area of the interface between two media by one unit area. Using this scheme to successfully describe the spherical cap shape of small drops on a solid substrate, they further established the well-known relationship between interfacial energies and equilibrium contact angle θ_E, the so-called Young's Law (see Fig. 2.1(a)):

$$\gamma_{LV} \cos\theta_E = \gamma_{SV} - \gamma_{LS} \qquad \text{Young's Law} \tag{2.1}$$

The interactions between solids and fluids, however, are generally more complex. Taking Young's Law as a prominent example, even this most fundamental relationship will not translate smoothly from theory to experiment. A drop deposited on a real substrate will regularly exhibit a static contact angle that is dependant on its history and might not equal the equilibrium contact angle.

This is due to the fact that a real drop deposited on a substrate will not be in equilibrium right away, but will move towards equilibrium in a decelerated motion. A moving contact line, however, shows a different contact angle depending on whether it is advancing or receding (see Fig. 2.1(b)). As the drop will normally get stuck in a local minimum of energy created by any tiny surface defect before reaching its equilibrium shape, the value of the static contact angle will lean towards the advancing or receding contact angle, depending on the contact line's direction of motion.

a) Equilibrium contact angle b) Advancing/receding contact angle

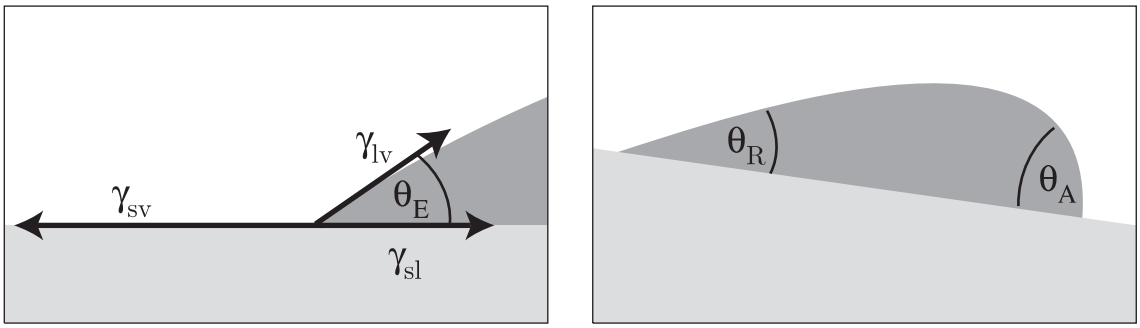

Figure 2.1: a) Static contact angle between solid S, liquid L and vapour V as described by Young's Law: $\gamma_{LV} \cos\theta_E = \gamma_{SV} - \gamma_{LS}$, where γ is the interfacial free energy between the respective substances (s: solid, l: liquid, v: vapour).
b) The static contact angle may deviate from the equilibrium angle. A liquid drop moving infinitesimally slowly on a substrate will exhibit an advancing contact angle θ_A in front and a receding contact angle θ_R at the rear. These angles will always obey $\theta_A > \theta_R$.

This example also demonstrates the underlying difficulty in any kind of experiment in the field of wetting: the measured quantities are very sensitive to impurities of the chosen substances. Because the methods of surface preparation improved over time, however, today we possess a whole range of meaningful data covering many aspects of the interaction between fluids and solids, which support advanced theories on the kinetics of wetting [Berg, 1993b; de Gennes, 1985; Leger and Joanny, 1992].

In recent years a lot of effort was put into experiments with drops on porous membranes where the interplay between the imbibition of the liquid and its simultaneous wetting was tested [Bacri and Brochard-Wyart, 2001; Blake and Coninck, 2004; Starov et al., 2003]. This field of research is not only scientifically interesting, but is also motivated by a number of important applications in industry, such as oil recovery, printing and textile technology.

When a liquid drop is placed on a porous substrate, it will wet the surface to attain its equilibrium shape and simultaneously lose volume (see Fig. 2.2 (a)); this leads to dynamics of drop base radius and contact angle that is completely different than in the case of wetting on a non-penetrable substrate.

In this case it is the capillary force that causes the liquid to enter the porous substrate. The kinetics of the resulting volume loss are well described by Darcy's Law and the Lucas-Washburn equation. Generally a fluid drawn into a porous substrate will fill the pores of this substrate up to a distance x that depends on the time t as $x \propto \sqrt{t}$ [Darcy, 1856; Schoelkopf et al., 2002; Washburn, 1921].

Experimental as well as theoretical studies of the wetting on porous substrates have been successfully performed in the last few years [Bacri and Brochard-Wyart, 2001; Blake and Coninck, 2004; Starov et al., 2003]. Before this work, however, there have been no experiments of any kind using networks of cross-linked polymers as a penetrable substrate. This is surprising as these materials are a favorite substance in biophysics and material science. In these fields a lot of attention is directed toward all kinds of polymer networks, those occurring in nature as well as those being used

for a multitude of applications such as medical implants, contact lenses, etc.

Both kind of substrates, that of a porous film and that of a cross-linked polymer, are penetrable for specially chosen liquids. As the driving force of liquid suction in cross-linked polymers is not the capillary force, but rather a diffusive force (see Fig. 2.2 (b)), this implies that a different behaviour of all experimental quantities may be possible.

It is therefore the aim of this work to extend the knowledge on wetting behaviour of liquids on solids and to study a system with a polymer substrate as the (penetrable) solid surface. With the perspective of possible applications in bioscience, the system was designed in such a way as to allow further use in such biophysical studies.

As possible biophysical studies would most likely include experiments with living cells, all substances used have to be bio-compatible. Living cells also demand an aqueous medium. Those two requirements were met with the setup used in this dissertation.

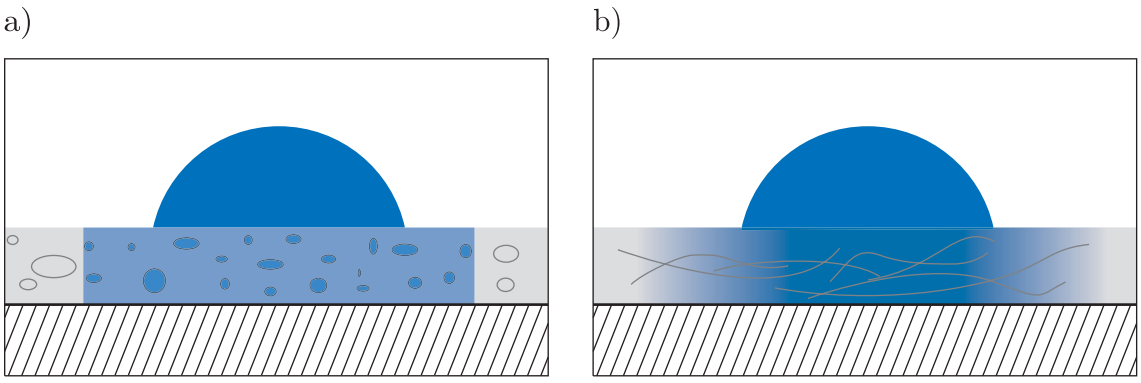

Figure 2.2: a) Liquid drop wetting a porous film on a supporting substrate. The liquid is drawn into the porous film by capillary forces. The boundary between the inner region where the pores are already filled with liquid and the dry region is sharp and moves with a velocity $v \propto \sqrt{t}$.
b) Liquid drop wetting a film of cross-linked polymers on a supporting solid substrate. The liquid is drawn into the film by diffusive forces resulting from a gradient in concentration of the liquid between drop ($c_{rel} = 1$) and polymer film ($c_{rel} = 0$ for $t = 0$). The liquid in the film diffuses outward resulting in a concentration profile of the liquid in the cross-linked network that decreases smoothly in the outward direction.

To account for bio-compatibility, the chosen class of substances was siloxanes (PDMS). Siloxanes are used for a variety of medical applications, such as implants and contact lenses, because of their outstanding bio-compatibility. Moreover they are also good candidates for wetting studies as their contact angles on solid surfaces in aqueous solutions can be set to low values by specially preparing the solid surface therefore facilitating wetting studies near the wetting transition.

The additional requirement of an aqueous ambient medium also presented the possibility to easily check for the influence of the interfacial energy $\gamma_{liquid/water}$ between drop and surrounding medium. The interfacial energy between water and liquid polymer $\gamma_{water/polymer}$ can be changed by more than a factor of two by either adding

polymers with specific side groups to the drop or by adding surface active components to the aqueous solution.

The chosen setup consisted of a cross-linked network of PDMS as the penetrable solid, fluid PDMS and water as the surrounding medium. This setup allowed for experiments of liquid drops on a permeable polymer network that tested the interplay between wetting and diffusion in a biophysically relevant setup.

The insights gained in these experiments are not only valuable from a purely scientific point of view, but will also be of interest for a number of technological applications. The most straightforward application can be found in printing technology, where small paint droplets that penetrate into a polymer substrate represent a typical printing process.

An interesting branch of biotechnology that might also profit from this work is the development of the so called *lab on a chip*. Especially where bio-compatibility is of importance the features studied in this work might facilitate improved processes, like cell separation by electrostatic pumping.

Chapter 3

Theory of Wetting and Diffusion

3.1 Simple Theory of Wetting

Wetting phenomena have been studied for a long time and have attracted more and more scientific attention since the 70ies especially. Since then there has been substantial progress in the understanding of wetting and non-wetting phenomena both experimentally as well as theoretically (for example [de Gennes, 1985; Leger and Joanny, 1992]). Today wetting is a very active field of research and many open questions remain: on the theoretical side, for example, a quantitative description of hysteresis and a good concept of wetting transitions, whereas on the experimental side surface reproducibility is still a problem. A good introduction to the general concepts of wetting can be found in [Berg, 1993b], which is one of the main sources for the following theory section.

3.1.1 Interfaces at Equilibrium

The Concept of Interfacial Energy

The behaviour of the interface between two immiscible phases can be described by the concept of interfacial energies or interfacial tensions. The interfacial energy density γ_{ij} between two interfaces is the free energy necessary to increase the area between these two interfaces by one unit area. This free energy results from the excess free energy that can be assigned to the atoms at the surfaces when compared to the bulk [Gibbs, 1928].

The interfacial energy density is therefore defined as

$$\gamma_{ij} = \left(\frac{\partial G}{\partial A_{ij}}\right)_{T,P,N_i,\ldots N_j} \tag{3.1}$$

where G is the Gibbs free energy of the interface, A_{ij} the interfacial area, T is the temperature, P the pressure and N_i the number of surface excess moles of the ith component.

γ_{ij} can also be considered as force per unit length. This line tension is usually referred to as interfacial tension. However this might lead to confusion as γ_{ij} does not include any elastic energy contributions, whereas the total tension γ_{ij}^{total} of a solid/fluid or solid/solid interface will include a contribution γ^s from the elastic energy stored in the tangential strain field in the solid near the interface:

$$\gamma_{ij}^{total}(\text{solid/fluid interface}) \quad = \quad \gamma^s + \gamma_{ij} \tag{3.2}$$

Only for interfaces between fluids, which by definition are incapable of supporting shear stresses, can γ_{ij} be truly referred to as an interfacial *tension* [Berg, 1993a]. Note that in literature the expressions *interfacial stress*, *interfacial tension* and *interfacial energy* are not always clearly distiguished.

The surface free energy $\gamma_{S0} = \gamma_S$ of a solid refers to the reversible work of forming a unit area of surface of the solid in a vacuum. This compares to the solid-vapour interfacial energy γ_{SV} as

$$\gamma_{S0} \quad = \quad \gamma_{SV} + \pi_{SV} \tag{3.3}$$

where π_{SV} is the spreading pressure of the vapour of the liquid on the solid.

The spreading pressure obeys the Gibbs adsorption equation

$$\pi_{SV} \quad = \quad RT \int_0^{P_0} \frac{\Gamma_{SV}}{P}\, dP \tag{3.4}$$

where R is the universal gas constant, T is the temperature, Γ_{SV} is the Gibbs surface excess of the vapour on the solid (i.e., the adsorbed molecules in moles per area), P is the pressure and P_0 is the saturation vapour pressure of the liquid.

The spreading pressure π_{SV} is usually assumed to be negligible. This assumption is supported by experiments on various surfaces: Fowkes et al. [1980] studied the possibility of spreading pressures arising with high-energy liquids (e.g., water vapor) deposited on low-energy solids, and found that this did not occur. Also Van Oss et al. [1992] found that with non-spreading apolar as well as polar liquids (including water), no spreading pressure occurs on polymers or on clay. There is however still discussion going on and there are also clues that the spreading pressure might be of importance in some cases [Schlangen et al., 1994; Yildirim, 2001].

In the following the interfacial energy γ_{SV} is used whenever possible as this quantity is easily accessible in experiments. However one should keep in mind that the quantities and γ_{SV} and γ_{S0} are often used interchangeably in literature.

Young Equation

If a small liquid drop is deposited on a solid in equilibrium with vapour, the resulting geometry can be described adequately by the interfacial energies. Here the corresponding interfacial energies are: γ_{SL}, the solid-liquid interfacial energy, γ_{SV}, the solid-vapour interfacial energy and γ_{LV}, the liquid-vapour interfacial energy.

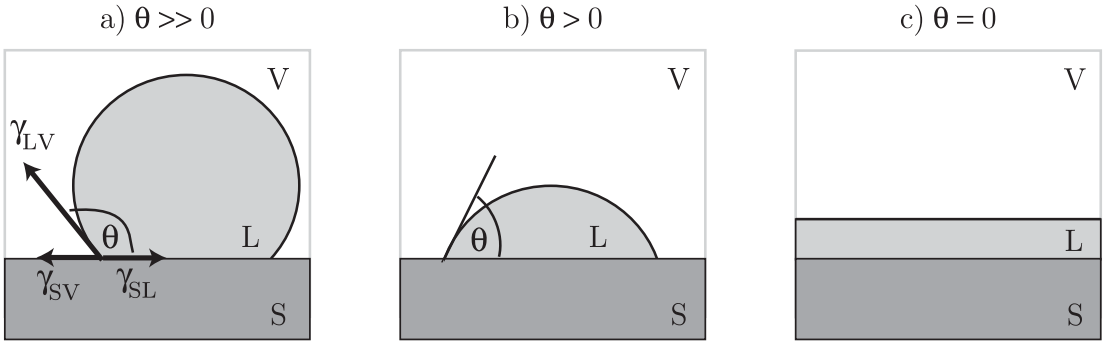

Figure 3.1: Sketch of a small droplet in equilibrium on a solid surface. The contact angle Θ depends on the interfacial energies γ_{ij} via the Young equation (Eq. 3.5). The situation in a) and b) is called partial wetting, c) is referred to as complete wetting with a contact angle of $\Theta = 0°$.

As early as 1805, Thomas Young [1805] stated that when a liquid makes contact with a solid surface it will approach the contact line following an angle that depends only on the interfacial tensions of the involved surfaces according to his famous equation

$$\gamma_{SV} - \gamma_{SL} = \gamma_{LV} \cos\Theta \qquad \text{Young Equation} \tag{3.5}$$

for a drop of liquid L on a solid surface S in vapour V (see Fig. 3.1 a)).

He derived this equation by considering the static forces that are applied to the liquid at the contact line between the three phases by the interfacial tensions (see Fig. 3.1 a). This equation can also be deduced from a thermodynamical consideration by minimizing the energy of a virtual displacement of the contact line [Gibbs, 1928]. Today there are still improvements being made in deriving this equation in a more general way [Roura and Fort, 2004].

If the contact angle $\Theta = 0°$ the liquid will form a thin film on the substrate. This situation is called *complete wetting*. For non-zero contact angles the situation is referred to as *partial wetting* (see Fig. 3.1). For small drops that are hardly affected by gravity the hydrostatic pressure $\Delta P = \gamma_{LV}(1/R_1 + 1/R_2)$ (R_1, R_2: local radii of curvature) will equilibrate according to Young's Law and the resulting shape will be that of a spherical cap.

This is only true on a macroscopic scale though, as the three-phase molecular interactions at the contact line are not accounted for. In a more detailed analysis thin-film forces like Van-der-Waals forces, steric repulsion or electrostatic interactions will alter the free energy as the solid will start to interact with the phase above the first liquid layer. This results in a so-called thin-film pressure $P(h)$ for a film of thickness h and will alter the shape of the drop at the rim [Brochard-Wyart et al., 1991; Cazabat et al., 1990; Yeh et al., 1999a,b].

Some other phenomena that occur at the rim region are line tension effects which have to be considered for small drops [Marmur, 1997] and the deformation of the local shape of viscoelastic substrates at the contact line [Carré et al., 1996; Shanahan and Carre, 2000].

Young equation for a solid/liquid/fluid system:

For a situation with a fluid F as the ambient medium, the Young equation becomes:

$$\gamma_{SF||L} - \gamma_{SL||F} = \gamma_{LF} \cos\Theta_{LF} \tag{3.6}$$

where $\gamma_{SF||L}$ is the interfacial tension at the solid/fluid interface with the interface in equilibrium with bulk liquid, $\gamma_{SL||F}$ the interfacial tension at the solid liquid interface with the interface in equilibrium with bulk fluid.

If adsorption is neglected Eq. 3.6 becomes:

$$\gamma_{SF} - \gamma_{SL} = \gamma_{LF} \cos\Theta_{LF} \tag{3.7}$$

Considering the systems depicted in Fig. 3.2 the respective Young equations can be merged into the Bartell-Osterhof equation:

$$\gamma_{LF} \cos\Theta_{LF} = \gamma_{LV} \cos\Theta - \gamma_{FV} \cos\Theta_{FV} \qquad \text{Bartell-Osterhof Equation} \tag{3.8}$$

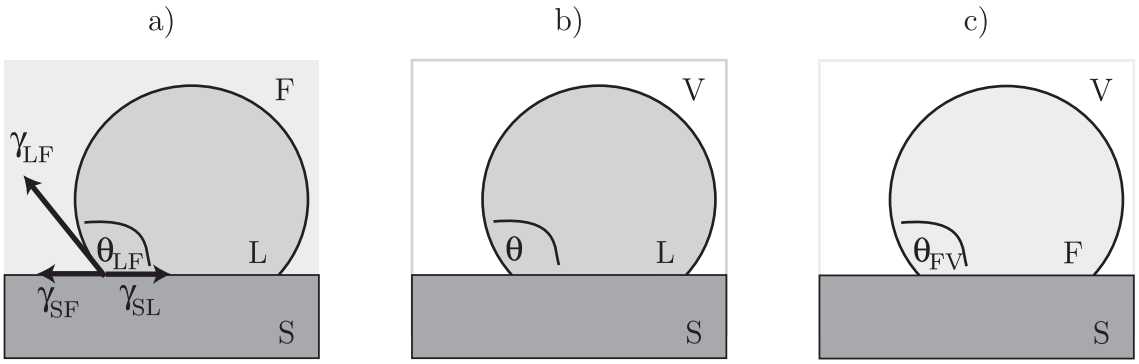

Figure 3.2: Sketch of small droplets in equilibrium on a solid surface. The contact angles Θ_{ij} depend on the interfacial energies γ_{ij} via the Young equations shown below the respective drawings. The Young equations can then be put together to give the Bartell-Osterhof-Equation, Eq. 3.8.

Wetting Parameters

There are three different expressions for the thermodynamic free energy of interaction between a liquid and a solid [Johnson and Dettre, 1993]. They are summarized

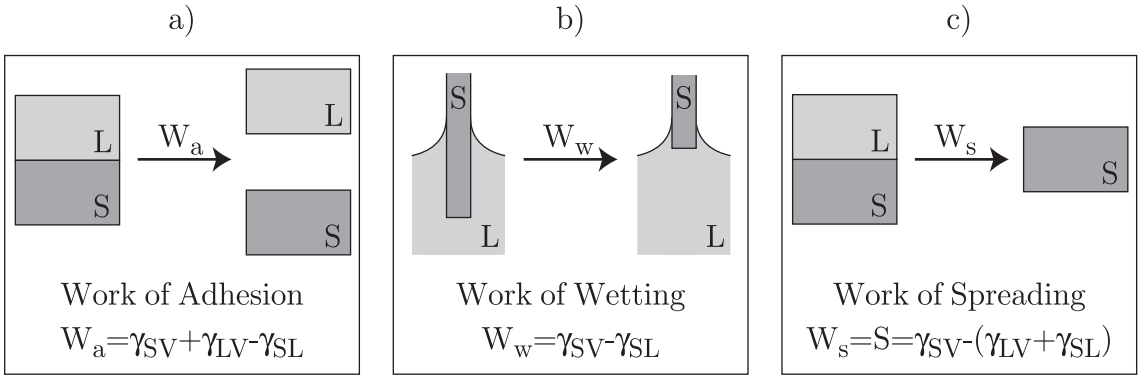

Figure 3.3: Thermodynamic quantities for solid/liquid interactions. All systems are in equilibrium with vapour.

in the following (see Fig.3.3). It is assumed in all three cases that the wetting system is in equilibrium with vapour and all separation procedures leave an adsorbed vapour layer on the solid surface. This is a reasonable assumption as this is also the case in all experimental setups. In contrast some authors use the same parameters to describe systems in vacuum [Berg, 1993a].

Work of Adhesion W_a The equilibrium work of adhesion W_a is the reversible work to separate a unit area of liquid from a solid. This can be described by:

$$W_a = \gamma_{SV} + \gamma_{LV} - \gamma_{SL} \qquad \text{Dupré Equation} \tag{3.9}$$

This equation reflects the fact that when a unit area of liquid is separated from a solid, a unit of solid/vapour interface and a unit of liquid/vapour interface are created and a unit of solid/liquid interface disappears. For a drop of liquid on a solid this equation then becomes:

$$\begin{aligned} W_a &= \gamma_{SV} + \gamma_{LV} - \gamma_{SL} \\ &= \gamma_{LV}\,(\cos\Theta + 1) \end{aligned} \tag{3.10}$$

For the situation of a liquid on a solid surrounded by a fluid, this equation becomes:

$$W_{a\,SL||F} = \gamma_{LF}\,(\cos\Theta_{LF} + 1) \tag{3.11}$$

where $SL||F$ denotes that the solid/liquid interface is in equilibrium with the fluid.

Work of Wetting W_w The work of wetting or wetting tension W_w is defined as the work needed to eliminate a unit area of solid/liquid interface while producing a unit area of solid/vapour interface (see Fig.3.3 b)):

$$W_w = \gamma_{SV} - \gamma_{SL} \tag{3.12}$$

Work of Spreading W_S: The Spreading Parameter S For a small liquid drop on a solid surface the important parameter is the spreading parameter S, where

$$S = \gamma_{SV} - (\gamma_{LV} + \gamma_{SL}) \tag{3.13}$$

for a system with vapour as the ambient medium.

S is the difference in free energy between a bare solid in contact with vapour and a solid covered with a flat thick layer of liquid. For $S \geq 0$ the last situation is energetically favourable and the drop will spontaneously spread to cover the whole surface. Such a situation is called *total wetting*. The case of $S < 0$ is referred to as *partial wetting* (compare to Fig. 3.1).

The spreading parameter can be described in terms of the contact angle via the Young equation:

$$S = \gamma_{LV} \quad (\cos\Theta \quad -1) \qquad \text{solid-liquid-vapour} \tag{3.14}$$

$$S = \gamma_{LF} \quad (\cos\Theta_{LF} \; -1) \qquad \text{solid-liquid-fluid} \tag{3.15}$$

Surface Free Energy and Molecular Interactions

The reason for a free energy contribution of any surface lies in the nature of molecular interactions between molecules. In wetting theories these interactions are usually divided into physical interactions like Van der Waals forces and chemical acid-base interactions. As it is assumed that those interactions are additive, the respective energies like the work of adhesion W_a (see Eq. 3.9) can be written as [Berg, 1993a]:

$$W_a = W_a^{physical} + W_a^{acid-base} \tag{3.16}$$

Even though the theoretical reasoning behind this model can be questioned, it successfully describes wetting phenomena and is therefore justified as a good approximation.

Physical Interactions Excluding Coulomb interaction and metallic bonding, the physical interactions between molecules are dipole/dipole (Keesom force), dipole/induced dipole (Debye force) and induced dipole/induced dipole (London dispersion force) interactions, known as Van der Waals forces [Israelachvili, 1985]. As the contribution of permanent dipoles to the relevant thermodynamic properties of interfaces is essentially negligible [Berg, 1993a], the Hamaker approach can be used for calculating those thermodynamic properties of interfaces between different substrates.

In the Hamaker approach the interaction between macroscopic bodies is computed by summing over the interactions of all possible pairs of molecules within those bodies. For semi-infinite half spaces interacting across a vacuum of distance s_0 the so derived potential Φ_{11} is

$$\Phi_{11} = -A_{11}\frac{1}{12\pi s_0^2} \tag{3.17}$$

where A_{11} is the Hamaker constant for a substance 1. The surface tension of this substance can now be calculated considering the work of separating two identical phases up to a distance $s_0 = s_m$ corresponding to the effective molecular spacing s_m across planes. As two planes are formed by this, the surface tension will then be:

$$2\gamma_1 = A_{11}\frac{1}{12\pi s_m^2} \tag{3.18}$$

As the Hamaker constant for interactions between unlike substances behaves like $A_{12} = \sqrt{A_{11}A_{12}}$ (*Berthelot's rule*) the surface tension of a system that is solely governed by Van der Waals forces is:

$$\gamma_{12} = \gamma_1 + \gamma_2 - 2\sqrt{\gamma_1\gamma_2} = (\sqrt{\gamma_1} - \sqrt{\gamma_2})^2 \tag{3.19}$$

If a substance is inert for chemical acid-base interactions (e.g., hydrocarbons) then it will interact with any other substances by Van-der-Waals forces only. For a drop of such a dispersion-force-only liquid on any solid substance the dispersion force contribution γ_S^d to the solid surface free energy γ_S can then be derived using Eq. 3.19 and Eq. 3.10:

$$\begin{aligned} W_a &= \gamma_L\,(1+\cos\theta) = \gamma_S + \gamma_L - \gamma_{SL} \qquad \text{(Eq. 3.10)} \\ \gamma_S^d &= \frac{1}{4}\,\gamma_L\,(1+\cos\theta)^2 \end{aligned} \tag{3.20}$$

Chemical Acid-Base Interactions The only chemical reactions that are important when regarding wetting phenomena are those that can be described within the concept of acid-base reactions. In the classical concept of the Brønstedt-Lowry theory, an acid is defined as a substance that is capable of donating a proton whereas a base is defined as a substance that is capable of accepting a proton. A wider definition, however, of an acid-base reaction is that of Lewis, stating that within an acid-base reaction electron density is transferred from the base to the acid.

The contribution of the Brønstedt-Lowry acid-base interactions to the work of adhesion can be estimated using the Bolger-Michaels theory [Bolgers and Michaels, 1968]. A more general and frequently used theory however is the van Oss-Chaudhury-Good correlation [Van Oss et al., 1988] that applies the Lewis acid theory and gives the acid-base part W_a^{AB} of the work of adhesion W_a as

$$W_a^{AB} = 2\sqrt{\gamma_S^{\oplus}\gamma_L^{\ominus}} + 2\sqrt{\gamma_L^{\ominus}\gamma_S^{\oplus}} \tag{3.21}$$

where $\gamma_S^{\oplus}$ and $\gamma_S^{\ominus}$ are defined as the characteristic acid and base parameters of the solid surface and $\gamma_L^{\oplus}$ and $\gamma_L^{\ominus}$ are defined as the characteristic acid and base parameters of the liquid. A good introduction to those theories can also be found in [Berg, 1993a].

Lifshitz-Van der Waals/Acid-Base Approach Combination of the physical and chemical interactions using Eq. 3.19 and Eq. 3.21 gives:

$$W_a^{AB} = \gamma_L (1 + \cos\theta) = 2\sqrt{\gamma_S^d \gamma_L^d} + 2\sqrt{\gamma_S^\oplus \gamma_L^\ominus} + 2\sqrt{\gamma_L^\ominus \gamma_S^\oplus} \tag{3.22}$$

with $\gamma = \gamma^d + \gamma^\oplus + \gamma^\ominus$.

This Lifshitz-Van der Waals/acid-base approach however has a major theoretical drawback. According to [Lyklema, 1999] all the derived equations have a weak thermodynamic background as thermodynamic quantities, here the surface tensions, are mixed up with mechanical ones, i.e. internal energies. The description of thermodynamic parameters involves temperature, while the mechanical quantity does not [Chibowski and Perea-Carpio, 2002].

Determining the Interfacial Energies

Interfacial energies of fluids can be measured directly by a multitude of methods such as the drop weight method (see App. C), the pendant drop method ([Boucher and Kent, 1978; Río and Neumann, 1997; Song and Springer, 1996a]), rotating drop method or the Wilhelmy plate method [Vold and Vold, 1983] even though one might encounter problems applying these methods towards substances with a higher viscosity.

The "surface energy" of a solid, on the other hand, cannot be measured directly. It can be calculated, though, from several semi-empirical approaches which try to evaluate the surface free energy of a solid from its contact angles with one or more liquids. Usually the static contact angle (or the slowly advancing contact angle as a substitute) is used. Other methods exist, for example only recently a method was proposed which uses the value of contact angle hysteresis [Chibowski and Perea-Carpio, 2002].

A common characteristic of all methods is that even though the theoretical reasoning might be questionable [Johnson and Dettre, 1993], the resulting equations fit the data reasonably well with the tested substances ranging over a multitude of polymer surfaces [Della Volpe et al., 2004; Shimizu and Demarquette, 2000; Siboni et al., 2004]. This in itself is a valid justification for using them as a means for determining the solid surface tension.

A few methods for determining the solid surface energy which were employed to characterize the substrate used in the experiments will be discussed in the following.

The Zisman Approach A widely used approach was set up by Zisman [1964] who showed that the cosines of the contact angles formed by drops of homologous liquids on a solid surface vary linearly with their surface tensions. The critical surface tension can then be found extrapolating the linear function to $\cos\Theta = 1$. Moreover the cosines of the contact angles formed by drops of different liquids vary linearly with $\sqrt{\gamma_{LV}^d/\gamma_{LV}}$ (where γ_{LV}^d and γ_{LV} are the dispersion component of the

surface tension and the surface tension of the different liquids used for contact angle measurements). It can be shown that the critical surface tension corresponds to the surface energy of the solid.

This method was then extended to incorporate the whole Lifshitz-Van der Waals--acid-base approach using Eq. 3.22. Now the dispersive and the acid-base components of the probe liquids have to be known to determine the solid surface free energy.

The so determined solid surface free energy γ_S however is still questionable as the contact angle in itself is dependent on the history of the system. Moreover, γ_S depends strongly on the chosen liquids although formally there should be no such a dependency [Chibowski and Perea-Carpio, 2002; Della Volpe et al., 2004]. Nevertheless, this method can give reproducible results especially when paying attention to the selection of test liquids [Della Volpe et al., 2003] and is therefore still the most commonly used method for solid surface energy determination.

Modified Zisman Approach The Zisman method demands a set of measurements with various liquids of known polar and dispersive components of the surface tension. According to Siboni et al. [2004] the original Zisman hypothesis can be easily modified to give a good fit to the data while reducing the number of the parameters to one:

$$\cos\Theta = \frac{1}{2\sqrt{\gamma_{LV}}}\left(2\sqrt{\gamma_{SV}} + \frac{\gamma_{SV}}{4} - \frac{\gamma_{LV}}{4}\right) \tag{3.23}$$

Regarding the limitations of the original Zisman approach, the reduction of the required measurements to one will largely reduce the significance of the so calculated values.

Equation of State Approach Another approach to calculating the surface free energy of a solid is the so called *Neumann's equation* [Kwok and Neumann, 2000]. This approach is based on the idea that the number of degrees of freedom of a two-component three-phase solid-liquid-vapor system is two and therefore any two of the intensive variables (like γ_{SV} or γ_{LV}) used to describe this system are sufficient to characterize the system completely $\gamma_{SL} = F(\gamma_{SV}, \gamma_{LV})$. This implies that the surface free energy cannot be divided without ambiguity in dispersive and acid-base parts. Using Berthelot's rule and several assumptions on the character of the interaction between the substances they set up the following equation:

$$\cos\Theta \;=\; -1 + 2\sqrt{\frac{\gamma_S}{\gamma_{LV}}}\; e^{-\beta(\gamma_{LV}-\gamma_S)^2} \tag{3.24}$$

where $\beta = 124.7\,\mathrm{m}^4/\mathrm{J}^2$ is an empirical parameter.

This approach has been discussed controversially for theoretical [Morrison, 1991] as well as for experimental reasons [Chibowski and Perea-Carpio, 2002] and it seems that the values calculated with the Neumann formula should be considered with caution.

Surface Energy from Contact Angle Hysteresis Even on smooth and chemically homogenous materials a liquid drop on a surface will exhibit contact angle hysteresis. If one considers this hysteresis to be due to a liquid film that is left behind the drop's receding contact line, it is possible to calculate the surface free energy γ_S [Chibowski, 2003]. Using the Young equation $\gamma_S - \gamma_{SL} = \gamma_{LV} \cos\Theta_A$ (Eq. 3.5) for the advancing contact angle Θ_A and a modified Young equation $\gamma_S + \pi - \gamma_{SL} = \gamma_{LV} \cos\Theta_R$, which includes the film pressure π, for the receding contact angle Θ_R, the surface energy of a solid γ_S can be expressed as:

$$\gamma_S = \gamma_{LV} \left(\cos\Theta_R - \cos\Theta_A\right) \frac{\left(1+\cos\Theta_A\right)^2}{\left(1+\cos\Theta_R\right)^2 - \left(1+\cos\Theta_A\right)^2} \tag{3.25}$$

Here, the theoretical reasoning is based on first principles. Nevertheless, values of γ_S obtained with this equation are in good agreement with those obtained by the commonly used Van-der-Waals/Acid-Base approach [Radelczuk et al., 2002]. Therefore this contact angle hysteresis approach seems to be a reasonable alternative for the determination of surface free energies of solids.

3.1.2 Wetting as a Dynamic Process

The very moment a drop of a liquid is deposited on a solid surface it will not be in equilibrium but relax into an energetically favorable state. Its kinetics are governed by the interfacial energies as well as by hydrodynamics.

Static Contact Angle Hysteresis

Even the universal Young equation has limits regarding its application to real systems as the *equilibrium* contact angle may not equal the measured *static* contact angle, which depends on the history of the sample. Generally the contact angle Θ_A of an advancing front will be larger than the contact angle Θ_R of a receding front (see Fig. 3.4 a)).

It is mostly agreed upon that contact angle hysteresis is due to several different mechanisms [Blake, 1993], which are usually given as surface roughness [de Gennes, 1985], microscopic chemical heterogeneity of the surface [Joanny and de Gennes, 1984], drop size effect [Gu, 2001; Marmur, 1997; Milchev and Milchev, 2001], molecular re-orientation and deformation at the surface [Carré et al., 1996; Yasuda et al., 1994] and the size of the liquid molecules penetrating into the pores and crevices of the solid surface. Moreover even if the surface is atomically flat and chemically homogenous contact angle hysteresis will occur due to liquid absorption, retention or swelling [Chibowski, 2003].

To illustrate one possible reason for contact angle hysteresis, a simple model of the effect of surface roughness on the contact angle is explained in Fig. 3.4. In this model Young's law is applied locally leading to the equilibrium contact angle Θ_E between the local slope of the solid and the liquid-vapour interface. The apparent

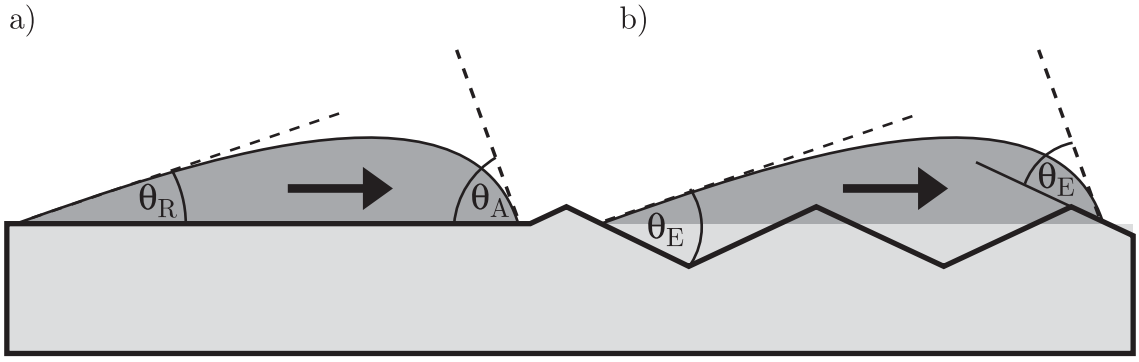

Figure 3.4:

a) As a drop moves infinitesimally slowly on a surface, it will exhibit the advancing contact angle Θ_A on one side as well as the receding contact angle Θ_R on the other.

b) In a simple model of contact angle hysteresis on a rough surface, Young's law is applied locally leading to an equilibrium contact angle Θ_E between the local slope of the solid and the liquid-vapour interface. Therefore the apparent contact angle between the average solid surface and the liquid will exhibit different values for advancing and receding situations.

contact angle Θ is, however, the angle between the average solid surface and the liquid-vapour interface. Therefore the contact angle Θ will exhibit different values Θ_A for advancing and Θ_R for receding situations.

Even though this model is based on a crude simplification it already shows the main feature of different contact angles for advancing and receding situations. Also this model can be appended to more realistic situations and even though it is not possible to relate contact angle hysteresis to microscopic roughness with a simple formula, the contact angle appears to be a sensitive parameter to characterize surface roughness.

Dynamic contact angle of a spreading drop

A drop that is deposited onto a substrate will generally not be in its equilibrium shape, but will exhibit a contact angle Θ that is not equal to its equilibrium contact angle Θ_E. This means that the interfacial tension forces acting at the wetting line will not cancel as in the equilibrium case (see Fig. 3.5(a)). Instead the forces will generate a driving force F (see Fig. 3.5(b)) that drags the wetting line in such a way that the drop moves towards its equilibrium configuration [Blake et al., 1997]. The *unbalanced Young force* F per unit length of the wetting line is therefore:

$$\begin{aligned} F &= \gamma_{SV} - \gamma_{SL} - \gamma_{LV}\cos\theta \\ &= \gamma_{LV}\cos\theta_E - \gamma_{LV}\cos\theta \\ &= \gamma_{LV}\left(\cos\theta_E - \cos\theta\right) \end{aligned} \tag{3.26}$$

The irreversible work expended in moving the wetting line can now be determined using the force F. If the mechanism of the dissipation of this energy is known, a relationship between the velocity of the moving contact line v and the non-equilibrium

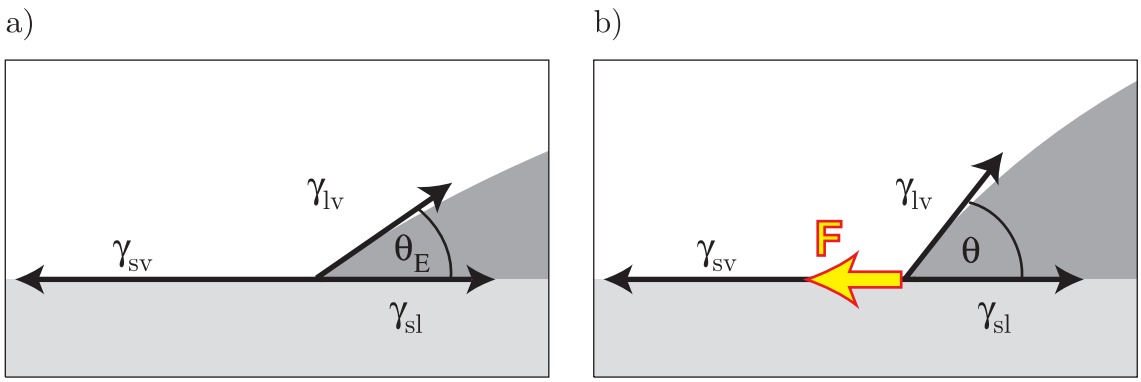

Figure 3.5:
a) Drop in equilibrium. The forces at the wetting line generated by the interfacial energies cancel.
b) Drop in a non-equilibrium conformation. The forces at the wetting line generated by the interfacial energies do not cancel but give rise to a force F per unit length that acts on the wetting line.

contact angle Θ can be established.

There are several ways how the energy can be dissipated at a moving contact line. Generally two types of models are used: *hydrodynamic* models that focus on the dissipation of energy due to viscous flow within the droplet and *molecular kinetic* models that focus on the dissipation due to binding/unbinding processes within the vicinity of the moving contact line.

Within the *hydrodynamic* approach the Navier-Stokes equation for slow viscous flow $\nabla P = \eta \triangle V$ (viscosity η, velocity V, pressure difference P) is used to generate a relationship between the value of the contact angle $\Theta(t)$ and the capillary number $Ca = \eta V/\gamma_{lv}$ (viscosity η, mean velocity of the contact line V). In the case of spreading droplets this leads to a simple scaling law [de Gennes, 1985]:

$$\begin{aligned} R(t) &\sim t^{1/10} \\ \Theta(t) &\sim t^{-3/10} \end{aligned} \tag{3.27}$$

In the form $\Theta \sim V^{1/3}$ these equation are also known as *Tanner's Law* [Tanner, 1979].

The *molecular kinetic* approach, on the other hand, concentrates on the dissipation of energy due to continuous binding and unbinding processes at the contact line [Blake et al., 1997]. Applying this theory to the case of spreading drops, the time dependence of the contact angle Θ and the drop base radius R can be described as:

$$\begin{aligned} R(t) &\sim t^{1/7} \\ \Theta(t) &\sim t^{-3/7} \end{aligned} \tag{3.28}$$

Both theories have been used to successfully describe data from various experiments [Blake, 1993; Cazabat et al., 1997]. To overcome this discrepancy a combined model

was proposed by de Ruijter et al. [2000, 1999] which takes into account both channels of dissipation. Within this model the spreading of a drop will exhibit four stages:

1. A fast early stage where the drop base radius and the contact angle will change linearly with time.
2. A later stage which is dominated by a molecular-kinetic behaviour and can be described by Eq. 3.29.
3. The molecular-kinetic behaviour reverts to a hydrodynamic behaviour, which can be described by Eq. 3.28 later on.
4. A long-time relaxation to equilibrium in which the contact angle and the drop base radius will exhibit an exponential behaviour.

The times for which the kinetics will move from one stage to the next are functions of several variables such as the volume of the drop, the viscosity and the surface tension.

3.2 Diffusion

3.2.1 General Theory

Diffusion of particles is a process that is driven by a gradient in concentration. Considering a particle that performs a three-dimensional random walk in an isotropic, homogenous medium, the probability density $c(\mathbf{r},t)$ of the location of the particle is a Gaussian distribution

$$c(\mathbf{r},t) = \frac{1}{(4\pi\, D\, t)^{3/2}} \exp\left(\frac{-\mathbf{r}^2}{4\, D\, t}\right) \tag{3.29}$$

with a mean square displacement of

$$\langle r^2 \rangle = 6\, D\, t \tag{3.30}$$

where D is the diffusion coefficient.

The behaviour of any system with an arbitrary initial concentration profile is governed by the following equations, which were established by Fick [1855]:

$$\mathbf{J} = -D\, \nabla c(\mathbf{r},t) \qquad \text{Fick's } 1^{st} \text{ law} \tag{3.31}$$

$$\frac{\partial c(\mathbf{r},t)}{\partial t} = D\, \Delta c(\mathbf{r},t) \qquad \text{Fick's } 2^{nd} \text{ law} \tag{3.32}$$

where $\mathbf{J}$ is the flow and $c(\mathbf{r},t)$ is the concentration.

These equations are universal and can be applied to particles of any sizes. The diffusion coefficient D however depends strongly on the system. Generally the diffusion coefficient D relates to the viscous friction coefficient ζ as

$$\zeta\, D = k_B\, T \quad \text{Einstein Relation} \tag{3.33}$$

where ζ is the viscous friction coefficient, k_B is the Boltzmann constant and T the temperature [Einstein, 1905].

For spherical particles the viscous friction coefficient can be related to its size as

$$\zeta = 6\pi\eta R \quad \text{Stokes Formula} \tag{3.34}$$

where R is the radius the particle and η is the viscosity of the surrounding liquid. Regarding Eq. 3.33 and Eq. 3.34 it is easy to see that the diffusion coefficient D becomes smaller for larger particles. This implies that for macroscopic particles the diffusion process becomes irrelevant as the process will be too weak to notice on any reasonable scales. A good introduction to the basics of diffusion can be found in [Crank, 1975] or [Nelson, 2003].

3.2.2 Diffusion of Polymers

The diffusion coefficients for the diffusion of polymers cannot be as easily connected to measurable parameters as is the case for spherical objects. A good review of the multitude of theories and physical models describing aspects of diffusion in polymeric networks can be found in [Masaro and Zhu, 1999].

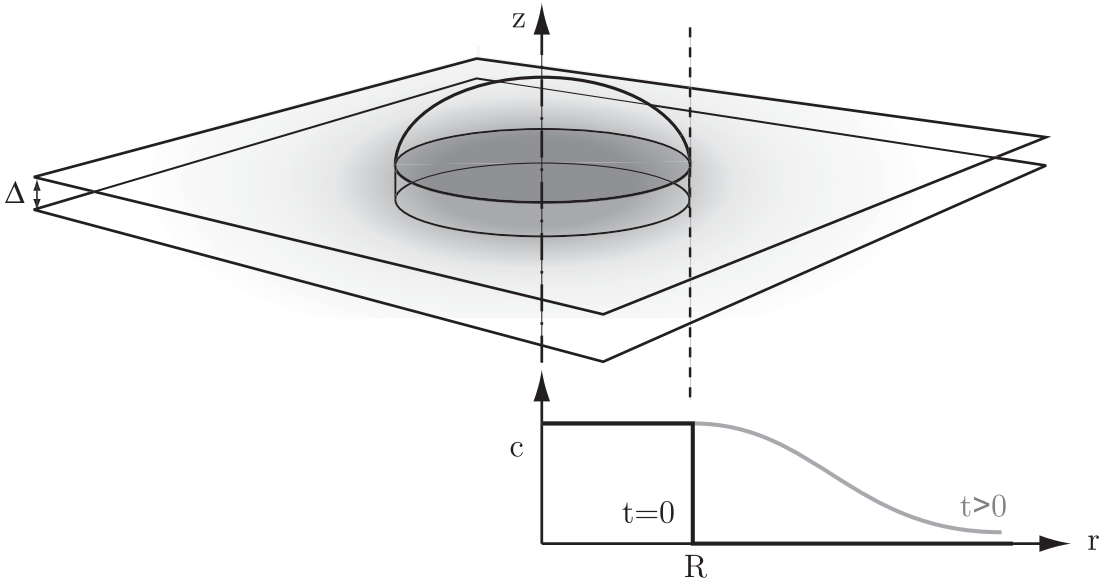

Figure 3.6: Sketch of a drop diffusing into a thin film (top). Also shown is the concentration profile of the fluid polymer in the thin film (bottom). Underneath the drop the concentration of the fluid polymer in the thin film can be treated as constant.

3.2.3 Solving the Diffusion Equation for an Axis-symmetric Drop with Constant Radius on a Thin Substrate

A sketch of the experimental setup is shown in Fig. 3.6. The diffusion process of a drop of liquid polymers into the thin film of cross-linked polymers can be analyzed more easily if we take into account that the thickness $\Delta = 200\,\text{nm}$ of the cross-linked film is small. The time an average PDMS polymer with a diffusion constant $D = 3.5\,\mu\text{m}^2/\text{s}$ (as determined experimentally, see Appendix D) will need to cross this distance is

$$t \;=\; \frac{\langle r^2 \rangle}{6 \cdot D} \;=\; \frac{(0.2\,\mu\text{m})^2}{6 \cdot 3.5\,\mu\text{m}^2/\text{s}} \;\sim\; 10^{-3}\,\text{s} \quad .$$

This can be considered as nearly instantaneous when compared to the time scale of changes in measurable experimental parameters, which is well above a second. This means that the liquid polymer of the drop should equilibrate within the underlying substrate quasi-instantaneously and the diffusion process in the cross-linked network is independent on the z-coordinate.

As the whole system is axial-symmetric, the diffusion process can be best described in cylindrical coordinates. The Laplace operator in cylindrical coordinates is given by

$$\Delta c(r, \varphi, z) \;=\; \frac{1}{r}\frac{\partial}{\partial r}\left(r \frac{\partial c}{\partial r}\right) + \frac{1}{r^2}\frac{\partial^2 c}{\partial \varphi^2} + \frac{\partial^2 c}{\partial z^2} \tag{3.35}$$

As shown above, it is reasonable to assume that the concentration of liquid PDMS within the thin film of cross-linked PDMS will equilibrate and be constant with

regard to the z-coordinate. Also the whole system is axis-symmetric in itself, which implies that the concentration is also independent of the angle. Therefore only the first term of the Laplace operator will enter the diffusion equations Eq. 3.31 and Eq.3.32:

$$\mathbf{J} = -D \frac{\partial c(r,t)}{\partial r} \cdot \mathbf{e_r} \tag{3.36}$$

$$\frac{\partial c(r,t)}{\partial t} = D \left(\frac{\partial^2 c}{\partial r^2} + \frac{1}{r} \frac{\partial c}{\partial r} \right) \tag{3.37}$$

This problem has the same governing equations as those for heat flow on a two-dimensional disk or the heat flow around a circular cylinder. Even though the equations are straightforward, solving them analytically as well as numerically is challenging. Nevertheless: analytical solutions for simple boundary conditions have been published [Carslaw and Jaeger, 1940; Goldstein, 1931; Jaeger, 1942].

Assuming that the film of cross-linked PDMS directly under the drop of fluid PDMS will be saturated with fluid PDMS for all times and the drop base radius R remains constant, the boundary conditions will be:

$$c(r < R, t) = c_0 \tag{3.38}$$

$$c(r > R, t = 0) = 0 \tag{3.39}$$

where c_0 is the maximal concentration of fluid PDMS in the matrix of the cross-linked PDMS.

The solution of the diffusion equation with these boundary conditions is given as [Goldstein, 1931]:

$$c(r,t) = \frac{2c_0}{\pi} \int_0^\infty \left(e^{-Du^2 t} - 1 \right) \frac{J_0(uR)\, Y_0(ur) - J_0(ur)\, Y_0(uR)}{J_0^2(uR) + Y_0^2(uR)} \frac{\mathrm{d}u}{u} \tag{3.40}$$

where J_0 is the Bessel function of the first kind of zero order, Y_0 is the Bessel function of the second kind of zero order and R is the drop base radius.

It is not possible to solve this integral analytically and even a numerical solution is not possible in a straightforward manner. Following [Razi Naqvi, 1974], however, the flux across the perimeter of the circle at $r = R$ can be given as :

$$\begin{aligned} \Phi(R,t) &= 2\pi\, D \left(r \frac{\partial c}{\partial r} \right)_{r=R} \\ &= \frac{8D\, c_0}{\pi} \int_0^\infty \frac{e^{-Du^2 t}}{u \left(J_0^2(uR) + Y_0^2(uR) \right)} \frac{\mathrm{d}u}{u} \\ &= \frac{8D\, c_0}{\pi}\, I(0,1,\alpha) \end{aligned} \tag{3.41}$$

where

$$\alpha = Dt/R^2 \tag{3.42}$$

and $I(0,1,\alpha)$ is a function that has been evaluated by Jaeger and Clarke [1942]. They present a table of values for $I(0,1,\alpha)$ and approximations for the case of small and large α:

$$\Phi(R,t) = 2\pi D\, c_0 \left\{ (\pi\alpha)^{-1/2} + \frac{1}{2} - \frac{1}{4}\left(\frac{\alpha}{\pi}\right)^{1/2} + \frac{1}{8}\alpha \ \ldots \right\} \qquad \text{small } \alpha \tag{3.43}$$

$$\Phi(R,t) = 4\pi D\, c_0 \left\{ \frac{1}{y} - \frac{\gamma}{y^2} + \frac{\pi^2/6 - \gamma^2}{y^3} + \mathcal{O}\left(1/y^4\right) \right\} \qquad \text{large } \alpha \tag{3.44}$$

where $\gamma = 0.57722$ is Euler's Constant and

$$y = \ln(4\alpha) - 2\gamma\ . \tag{3.45}$$

Regarding the used setup of a liquid drop on a thin film of cross-linked polymer, this calculation has limitations as it relies on the fact that the radius R of the drop stays constant. In the experiment this only holds true for short times. Nevertheless for short times this calculation should give a good approximation of the loss of volume through diffusion.

Chapter 4

Introducing a Bio-compatible System for Wetting Studies

4.1 Bio-compatibility as a Goal in Wetting Studies

Most of the published studies on the behaviour of wetting liquids on solid substrates have been done with air as the ambient medium (see [Leger and Joanny, 1992] for references). This is mainly due to two reasons. Firstly these systems only depend on the interaction of two materials and are therefore the best choice when probing the fundamentals of wetting. Secondly those systems can be observed more easily than systems with a fluid as an ambient medium.

However biophysics is a broad field where knowledge of wetting phenomena in an aqueous ambient medium would be of great importance as this is the natural environment for most biologically relevant processes. There have been a few studies on wetting phenomena in aqueous media, but most have been done with alkanes as the wetting liquid [Callaghan et al., 1983; Steinmaßl, 2000]. Alkanes have one major drawback for further use in biophysics: They are not bio-compatible (see Appendix A).

A class of substances which are not soluble in water and are well known for their bio-compatibility are siloxanes [Malchiodi-Albedi et al., 2002]. They are widely used in medicine for a variety of applications such as implants, contact lenses, etc. Moreover they are also good candidates for wetting studies as their contact angles on solid surfaces in aqueous solutions can be set to low values by specially preparing the solid surface.

The bio-compatibility of a series of polydimethylsiloxanes with different side groups compared to that of alkanes was specially tested using human umbilical vein endothelial cells (HUVEC). HUVECs are primary mammalian cells and therefore very sensitive. This recommends them for stringent tests regarding bio-compatibility. Details of the test are shown in Appendix A.

In this study polydimethylsiloxanes (PDMS) with and without additional side groups

were used for the wetting liquid as well as for the preparation of the solid substrate. The ambient medium for the wetting experiments was doubly deionised water in all cases, prepared by first purifying tap water by ion exchange (SERADEST, SERAL, ERICH ALHÄUSER GMBH, RANSBACH-BAUMBACH) and then further cleaning by carbon adsorption and ion exchange (Milli-Q Reagent Grade Water System, R>18 $M\Omega cm^{-1}$, pH 5.5, MILLIPORE, MOLSHEIM, FRANCE). Because of its purity, water of this quality is also commonly used for film balance studies, a technique that is very sensitive to contamination with surface active substances (for example [Demé et al., 2000]).

4.2 Identifying a PDMS-based System for Studying Wetting Under Water

Polydimethylsiloxanes have been widely used in studies of wetting behaviour with air as the ambient medium [Ausserré et al., 1986; Chen and Wada, 1989; Leger et al., 1988]. The solid substrates used in these studies are varied and range from oxidized silicon wafers to glass covered with a covalently bound monolayer of PDMS.

As the aim was to study wetting behaviour near the wetting transition, a first task was to identify a solid substrate on which such wetting experiments with PDMS could be performed. This was checked by testing the behaviour of a thin film of fluid PDMS on the substrate upon immersion in water. If the thin film dewetted fast and with a large contact angle the substance was rejected for further use, whereas a desired substrate exhibited no dewetting or a slow dewetting with a small contact angle.

Different types of substrates were tested as a solid surface for the wetting of PDMS oil in an aqueous environment. The fluid PDMS oil which was put on top of the substrates was mixed with siloxanes with different side groups to check for the influence of the thus altered interfacial energies. The experimental details are described in Appendix B.

The only substrate that allowed a film of fluid PDMS to be stable under water for a reasonable time and showed a small contact angle of only a few degrees was a cross-linked film of PDMS.

4.3 Properties of Fluid PDMS

Polydimethylsiloxanes are flexible polymers with a backbone of Si–O bonds (see Fig. 4.1). They are a good example of a Gaussian coil. The statistical segment length of $b = 0.561\,\text{nm}$ is only a few Si–O bond lengths (0.164 nm). The persistence length is less than 10 Å [Beaucage et al., 1996].

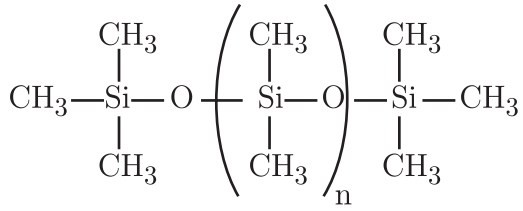

Figure 4.1: Chemical structure of polydimethylsiloxane (PDMS).
PDMS has a backbone of Si–O bonds. It is bio-compatible and widely used for various medical applications.

Fluid PDMS was used as the wetting liquid in all experiments. Two batches of PDMS differing in molecular weight (DMS-T22. DMS-T21, Gelest, ABCR, Karlsruhe) were used. These two batches were the only commercially available batches that had a molecular weight big enough to be non-volatile and a low enough viscosity to be deposited with micropipettes.

To test the influence of the interfacial energy γ_{PDMS/H_2O} on the wetting kinetics a mixture of pure polydimethylsiloxane (DMS-T22) with a 0.1% fraction of polar (carboxylate-pyrolidonepropyl)-methylsiloxane-dimethylsiloxane copolymer (YBD-125, Gelest, ABCR, Karlsruhe) was used.

A few physical parameters of the PDMS polymers used are shown in Table 4.1. The refractive index of the polar mixture was measured as 1.403 with an Abbé refractometer and is in good agreement with the refractive index of the main component DMS-T22. The interfacial energy γ_{PDMS/H_2O} of both DMS-T21 and the mixture of DMS-T22 with 0.1% YBD-125 was measured with the drop weight method. The value of the interfacial energy $\gamma_{PDMS/H_2O} = 36.8\,{}^{mJ}/_{\text{m}^2}$ for DMS-T21 is in good agreement with data taken from literature (see Table 4.1). A more detailed description of this measurement with the drop weight method can be found in Appendix C.

	DMS-T22	DMS-T21	YBD-125
Viscosity in cSt = mm^2/s	200	100	400–600
Dynamic viscosity in µsPa	1.936	0.966	3.9–5.9
Density in kg/l	0.968	0.966	0.98
Molecular weight in Da	9430	5970	2000
Average number of repeat units n	125	78	
Refractive index	1.4030	1.4025	1.4052
Surface tension γ_{LV} in $^{mJ}/_{m^2}$	21.0^a 20.9^a 21.8^b, 20.6^c		

	DMS-T22	DMS-T21	DMS-T22 + 0.1% YBD-125
Interfacial tension γ_{LF} to water in $^{mJ}/_{m^2}$	38.4^d (5.64^e)	36.8^f	27.7^f

a ABCR catalogue
b [Drummond and Chan, 1997]
c [Sauer and Dee, 1991]
d [Reiter and Khanna, 2000]
e [Binks et al., 1999]
f measured, see App. C

Table 4.1: Physical properties of the different fluid batches of PDMS used in the experiments. Data taken from the manufacturer if not otherwise stated. The value of $5.64\,^{mJ}/_{m^2}$ for the interfacial energy γ_{LF} to water as measured by Binks et al. [1999] seems to be a factor of 10 too small when compared to other measurements.

4.4 A Substrate of Cross-linked PDMS

To avoid problems due to unknown ingredients no commercially available prefabricated formula (such as Sylgard™) was used for the preparation of the layer of cross-linked PDMS. Instead the cross-linked film of PDMS was prepared with a procedure taken from Hillborg et al. [2000] and modified to suit the task.

Experiments were performed on a film of cross-linked polydimethylsiloxane prepared from a vinyl terminated polydimethylsiloxane (DMS-V31, Gelest, ABCR, Karlsruhe) with a cross-linker of methylhydrosiloxane - dimethylsiloxane copolymer (HMS-301, Gelest, ABCR, Karlsruhe) and platinum - divinyltetramethyldisiloxane complex as catalyst (SIP 6830.0, Gelest, ABCR, Karlsruhe) (see Fig. 4.2).

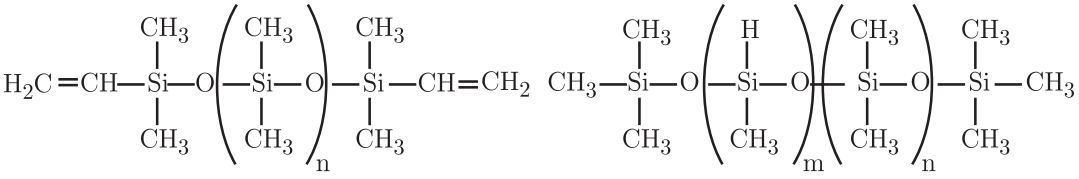

(a) **(b)**

Figure 4.2: Thin films of cross-linked PDMS were produced using vinyl terminated polydimethylsiloxane (a) with a cross-linker of methylhydrosiloxane - dimethylsiloxane random copolymer (b). The reaction was set forth by a platinum catalyst (not shown).

The bond forming chemistry is a platinum catalysed hydrosilylation reaction which is shown in Fig. 4.3.

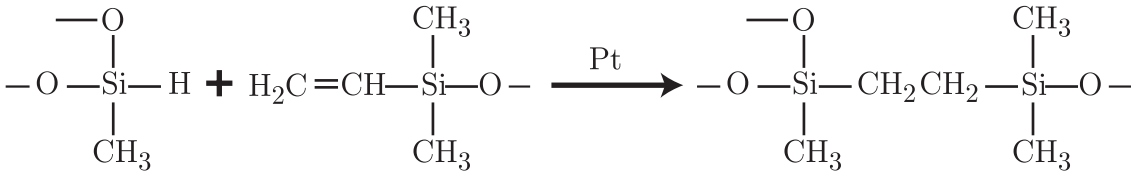

Figure 4.3: The cross-linked film of PDMS is formed by a platinum catalysed hydrosilylation reaction. Notice the absence of any byproducts.

For some experiments a film prepared from vinyl terminated polydimethylsiloxanes with a shorter chain length was used (DMS-V21, Gelest, ABCR, Karlsruhe). Cross-linker and catalyst were the same as mentioned above.

A few physical properties of the used polymers are listed in Table 4.2.

Concentration, the ratio of ingredients and spin-coating speed all affect the surface structure and the thickness of the film. As reproducible experiments on wetting demand a homogeneous surface and the employed technique of Reflection Interference Contrast Microscopy (RICM) demands a certain film thickness to gather enough

	Order no. ABCR	Molecular weight in g/mol	Repeat units n	Repeat units m
Vinyl terminated polydimethylsiloxane	DMS-V31	28000	375	
	DMS-V21	6000	78	
Methylhydrosiloxane–dimethylsiloxane copolymer	HMS-301	1900-2000	25	14

Table 4.2: Physical properties of the polymers used for preparing the cross-linked film. n and m are the average numbers of repeat units as depicted in Fig. 4.2. All data taken from the manufacturer.

contrast for reliable data interpretation, the details of the preparation had to be determined accordingly.

Various combinations of concentration, ratio of ingredients and spin-coating speed were tested. Only a narrow regime of mixing ratios gave good results of the cross-linked film in terms of surface stability and homogeneity. For mixing ratios outside this region the film showed undesired features: dewetting behaviour once immersed in water (insufficient cross-linking) or an inhomogeneous surface with a lot of point-like or crystalline defects when checked with RIC microscopy.

The speed and time of spin-coating was also optimised as slow spin-coating leads to a wave-like oscillating height structure whereas excessive speed of spin-coating leads to an instable spinning process due to the eccentricity of the chuck disk and the square cover slip.

Simultaneously we checked whether the RICM contrast could be enhanced by introducing a contrast layer of magnesium fluoride (MgFl). Clean cover slips were first coated with MgFl in varying thickness (0, 25, 50, 75 nm) and then coated with the film of cross-linked PDMS. The contrast is surprisingly good even without an additional contrast layer, so in all further experiments no additional contrast layer was used.

The details of the preparation that turned out to produce the best results in terms of surface homogeneity and film thickness will be described below.

4.5 Preparation of the Substrate

The best combination in terms of surface homogeneity and contrast was a mixture of 5% weight/weight solutions of hydride:vinyl in the ratio 2.8 : 100 which approximately complies with a ratio of between 1:1 and 1:2 hydride groups per vinyl group as mentioned in literature [Hillborg et al., 2000; Kim et al., 1997; Silberzan et al., 1994].

The 5% weight/weight solutions of vinyl terminated polydimethylsiloxane (DMS-

V31, DMS-V21) and methylhydrosiloxane-dimethylsiloxane copolymer (HMS-301) were prepared in heptane (puriss., >99.5%, SIGMA-ALDRICH CHEMIE GMBH, STEINHEIM, GERMANY). Both were stored at room temperature. A $1\,^{mg}/_{ml}$ solution of platinum catalyst in heptane was prepared. It was stored under argon at -18°C. No chemicals were stored longer than one year.

	Cross-linked PDMS with long polymers	Cross-linked PDMS with short polymers
Vinyl terminated polydimethylsiloxane, DMS-V31, 5%⋆ in heptane	1 ml	
Vinyl terminated polydimethylsiloxane, DMS-V21, 5%⋆ in heptane		1 ml
Methylhydrosiloxane-dimethylsiloxane copolymer, HMS-301, 5%⋆ in heptane	28 µl	125 µl
Platinum catalyst, $1\,^{mg}/_{ml}$ in heptane	25 µl	150 µl

(⋆ weight percent)

Table 4.3: Mixing ratios for the two different films of cross-linked PDMS used in the experiments.

The cover slips were cleaned as follows[1]:

1. Immersing cover slips in a 2% solution of Hellmanex (HELLMA, MÜLLHEIM, GERMANY) in double deionized water and sonicating for 15 minutes.
2. Exchanging the cleansing solution with millipore water 7 times.
3. Sonicating for 15 min.
4. Exchanging water 7 times.
5. Sonicating for 15 min.
6. Exchanging water 7 times.
7. Pouring out water and drying the cover slips at 70°C overnight.

To prepare a film of cross-linked PDMS on a cover slip the platinum catalyst solution was added to the 5% weight solution of DMS-V31 and thoroughly shaken. Afterwards the cross-linker solution HMS-301 was added and mixed by shaking. Only glass containers and glass syringes (HAMILTON BONADUZ AG, BONADUZ, SWITZERLAND) were used during the preparation to prevent any contamination

[1]This cleansing procedure was also used to clean measurement chambers and other equipment.

from soluble plastic residuals. The used amounts of the respective solutions are shown in Table 4.3. The resulting solution was kept at 0℃ to slow down the cross-linking process. The working time for the uncooled mixture is given by ABCR (GELEST, ABCR, KARLSRUHE) as 5–10 minutes. Nevertheless the whole spin-coating process was performed within seven minutes.

A clean cover slip was put into the spin-coater (Delta 10 TT, B.L.E. LABORATORY EQUIPMENT GMBH, SINGEN) and approximately 0.3ml of the solution was deposited onto it with a pasteur pipette. Immediately afterwards the spin coating process was started. The duration of spinning was 30 s at 6000 cycles/second with a device-dependent acceleration parameter of 5.

The specimens were then cured at 70℃ for three days. No experiment was performed later than two days after removal from 70℃.

4.6 Characterization of the Substrate

The so prepared specimen were subjected to various methods of surface investigation.

Ellipsometry

Ellipsometry enables the measurement of both refractive index and film thickness at the same time. Here wafers of oxidised silicon (thickness 1 mm, WACKER SILTRONIC, BURGHAUSEN, GERMANY) were coated with cross-linked PDMS as described above. As glass and oxidised silicon have a chemically similar surface and are both very smooth, films prepared in a similar way on these substances should resemble each other. Film thickness and refractive index of six samples were measured at three to twelve points under different angles of incident light. The refractive index of the cross-linked film was determined as 1.4196 with a standard deviation of 0.0014. The film thickness proved to be extremely homogeneous with an average film thickness of 207 nm. The overall standard deviation was 1.6 nm, the standard deviation within the single samples even less than 1nm. This shows that the spin-coating process is very reliable and leads to samples with a reproducible film thickness and a constant film thickness within the single sample.

Scanning Electron Microscopy

Samples of cross-linked PDMS on glass were observed by scanning electron microscopy (Philips CM 10, 20kV) with the help of Marianne Hanzlik at the Department of Electron Microscopy of the Technische Universität München. After metallisation (sputtering) with gold the samples were observed at 40° with a acceleration voltage of 20 kV. The samples reveal a smooth surface even on length scales below µm. The surface can be easily deformed, a scratch of metal forceps is clearly visible and exhibits a rim of surplus material (see Fig. 4.4).

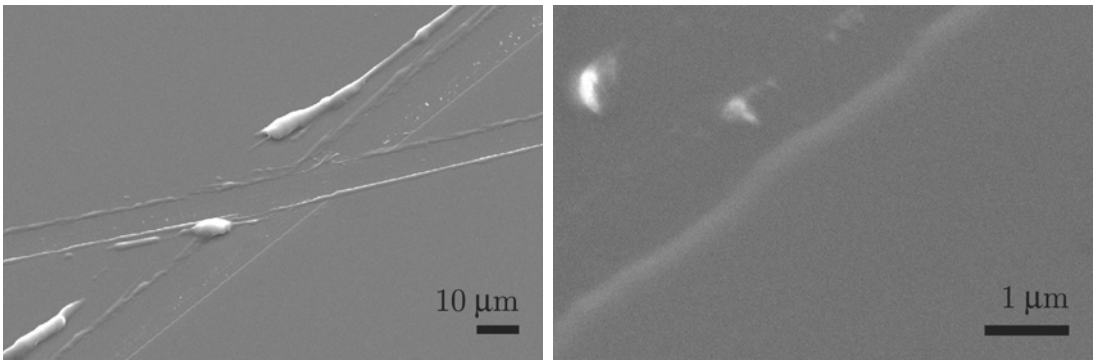

(a) (b)

Figure 4.4: SEM micrograph of a film of cross-linked PDMS on glass. The surface appears to be very smooth.
(a) Scratches of metal forceps on cross-linked PDMS.
(b) Picture of the same spot at higher magnification. The surface appears to be smooth even on length scales below 1 µm.

Atomic Force Microscopy

A sample of cross-linked PDMS on glass was observed with atomic force microscopy (AFM) in tapping mode. The AFM is an instrument that scans the surface of a sample with a tip that is attached to the end of a cantilever [Hansma and Hoh, 1994]. When the tip comes into contact with the sample, it deflects. This deflection is then detected by a laser beam that is reflected at the lever onto a segmented photodiode. As the cantilever deflection should be small to reduce the force applied to the sample, the height of the sample is adjusted in a feedback loop. The x-y scanning and height adjustment are all accomplished using a piezoelectric crystal. In tapping mode AFM the cantilever oscillates at a high frequency and the change in amplitude when the cantilever approaches the substrate is monitored.

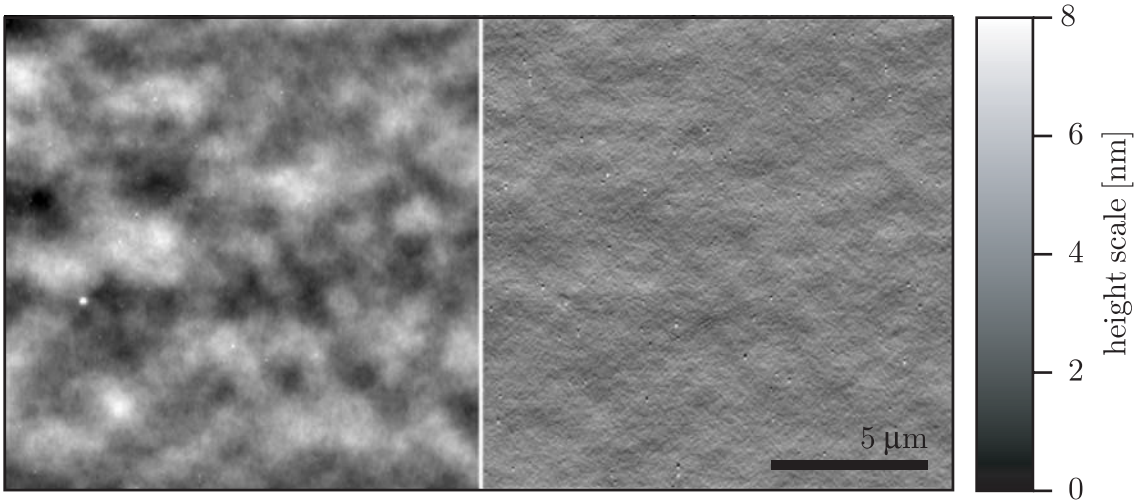

Figure 4.5: AFM micrograph of a film of cross-linked PDMS on glass. The picture was acquired in tapping mode and flattened afterwards. The height image is shown on the left, the error signal on the right. The maximal height fluctuation is less than 12 nm per 100 µm (height image, left side). The surface is smooth. The error signal (right side) shows electronic noise with no point defects.

In AFM measurements two images are obtained: a height image that displays the changes in sample height during scanning (Figure 4.5, left) and an error signal image that reflects the small changes in the cantilever oscillation due to the finite speed of height adjustment (Figure 4.5, right). The error signal image accentuates edges and can be used to check for surface roughness on a small scale.

AFM images of cross-linked PDMS on glass were taken with the help of Dirk Mayer at the Forschungszentrum Jülich ISG-2 on a MultiMode AFM/STM with Nanoscope 4 Controller (Veeco Instruments GmbH, Mannheim, Germany) and Si-Tapping Mode Cantilever (270kHz,Veeco Instruments GmbH, Mannheim, Germany). The film of cross-linked PDMS proved to be very sticky under water and could not be observed properly so the sample was observed in ambient air where stickiness did not pose a problem. Two samples were observed at several spots. All measured patches were very homogeneous with a maximal height deviation of less than 12 nm per 100 µm (see Figure 4.5, left). The surface was very smooth. No point defects could be seen, the error signal image showed mainly electronic noise with an amplitude of 0.8 nm (see Figure 4.5, right).

Contact Angle Measurements

The equilibrium contact angle of a drop of water on the thin film of cross-linked PDMS was determined using a Krüss DSA-10 angiometer located at the Lehrstuhl für Makromolekulare Stoffe of the TU München. Digital images of a drop on a surface were obtained and the contact angle was afterwards determined with an analysis tool from the manufacturer. This tool fits the drop shape with a minimal energy surface and can therefore determine the contact angle very accurately. A typical picture of a drop on the surface with the calculated fit is shown in Fig. 4.6

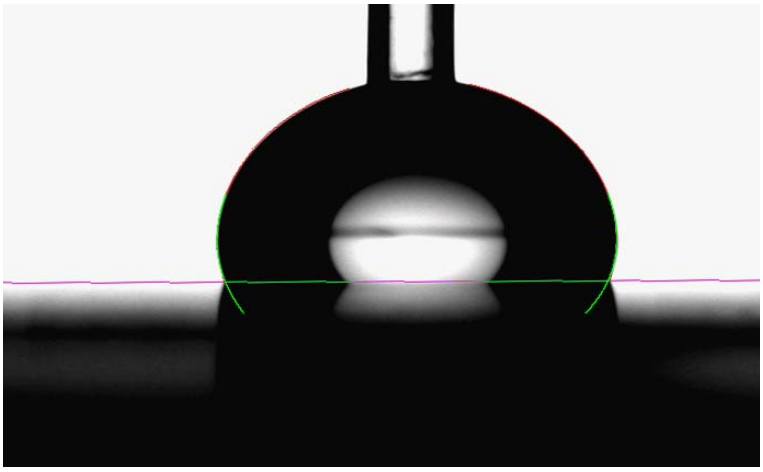

Figure 4.6: Contact angle measurement of water on cross-linked PDMS. The contact angle is determined by a fit of the drop shape according to the Young equation. Therefore the contact angle can be determined very accurately.

Films of cross-linked PDMS made with vinyl terminated PDMS with different chain lengths (DMS-V31 and DMS-V21) were prepared on glass. For each of the two different coatings three specimens were tested by measuring the contact angles of two drops at different spots. As the volume of each drop was slowly increased ($v \leq 10\,\mu l/min$) advancing contact angles were measured app. 10 times. Receding

	Θ_{adv}	N(adv)	Θ_{rec}	N(rec)	$\Delta\Theta$
DMS-V31	113.2 ± 1.7	31	109.4 ± 1.3	22	3.95 ± 0.09
DMS-V21	111.9 ± 2.6	25	110.9 ± 2.6	23	1.0 ± 0.5

Table 4.4: Contact angles of water on films of cross-linked PDMS. The contact angle hysteresis is small which indicates a smooth and homogeneous surface. Also shown are the total numbers of measurements.

contact angles were measured accordingly while slowly decreasing the volume of the drop.

The advancing contact angle of each drop did not vary by more than 0.5° between those measurements. The same holds true for the respective receding contact angles. The measured contact angles are shown in Table 4.4. The contact angle hysteresis of $\Delta\Theta \leq 4°$ is even smaller than values from literature on smooth and hydrophobic substances (20° on polytetrafluoroethylene [Extrand, 1998], 10°–20° on self-assembled monolayers of hexadecylchlorosilane [Lander et al., 1993]). This indicates a very homogeneous surface of the cross-linked PDMS.

The surface tension γ_{SV} was first calculated from the measurements of the slowly advancing contact angle and is shown in Table 4.5.

	γ_{SV}(Zismann) in mJ/m^2	γ_{SV}(Neuman) in mJ/m^2	γ_{SV}(Chibowski) in mJ/m^2
DMS-V31	14.7	15.0	20.8 ± 1.8
DMS-V21	16.0	16.3	22.3 ± 1.9

Table 4.5: The surface energy of a film of cross-linked PDMS was determined from the measurement of contact angle and contact angle hysteresis. For the determination of the surface energy the modified Zismann approach, the Neumann formula and the contact angle hysteresis approach were used. Errors resulting from the uncertainty of the contact angle measurement could only be estimated for the Chibowski method.

This was done with the use of the modified Zismann approach and the Neumann equation (see Eq. 3.23 and Eq. 3.24 in section 3.1.1). The surface tension was also determined from the contact angle hysteresis with the method described by Chibowski [2003] as the measured contact angle hysteresis was small enough to justify the assumption of a smooth and chemically homogeneous surface (see Eq. 3.25). The method of Chibowski assumes a thin film of oil left behind the receding drop which, in the case of a polymer oil on a network of cross-linked polymer, is a reasonable assumption as the polymers might entangle.

The surface energy of $\gamma_{SV} = 14.9 - 16.3\,{}^{mJ}/_{\mathrm{m}^2}$, determined by the methods of Zismann and Neumann, is lower than the interfacial free energy of the liquid polymer $\gamma_{LV} \approx 21\,{}^{mJ}/_{\mathrm{m}^2}$ which is a questionable result.

However the value of $\gamma_{SV} = 21 - 22\,{}^{mJ}/_{\mathrm{m}^2}$ obtained by Chibowski's method resembles the interfacial free energy of the liquid polymer γ_{LV}. Chaudhury and Whitesides

[1991] also determined the solid surface energy of cross-linked PDMS (Sylgard 170, Dow Corning Corp., Midland, MI., USA) to $\gamma_S = 21.1\,{}^{mJ}/_{\mathrm{m}^2} \approx \gamma_{LV}$ and account this to the fact that the surface groups (in this case methyl groups) of the polymers in both the liquid and cross-linked solid state have a similar orientation. They state that this might be possible as the backbone of the PDMS is highly flexible.

As the underlying assumptions of Chibowskis's method are reasonable and the data determined with this method resemble similar data from literature, the values of the interfacial energy $\gamma_{SV_DMS-V31} = 20.8\,{}^{mJ}/_{\mathrm{m}^2}$ and $\gamma_{SV_DMS-V21} = 22.3\,{}^{mJ}/_{\mathrm{m}^2}$ calculated with the method of Chibowski seem to be trustworthy.

Reflection Interference Contrast Microscopy

Reflection interference contrast microscopy (RICM) detects variations of the optical pathway with a height resolution of nanometers and a lateral resolution of less than one micrometer (see Section 5.4.1 and 5.5.4). A detailed description of the working principles of RIC microscopy is given in Chapter 5. In contrast to the previously mentioned methods like AFM that only work in air or even vacuum, RICM allows the sample to be observed with air or with water as the ambient medium. As the surface of the thin film of cross-linked PDMS might change upon immersion in water, it is important to check whether the surface stays smooth once brought into contact with water.

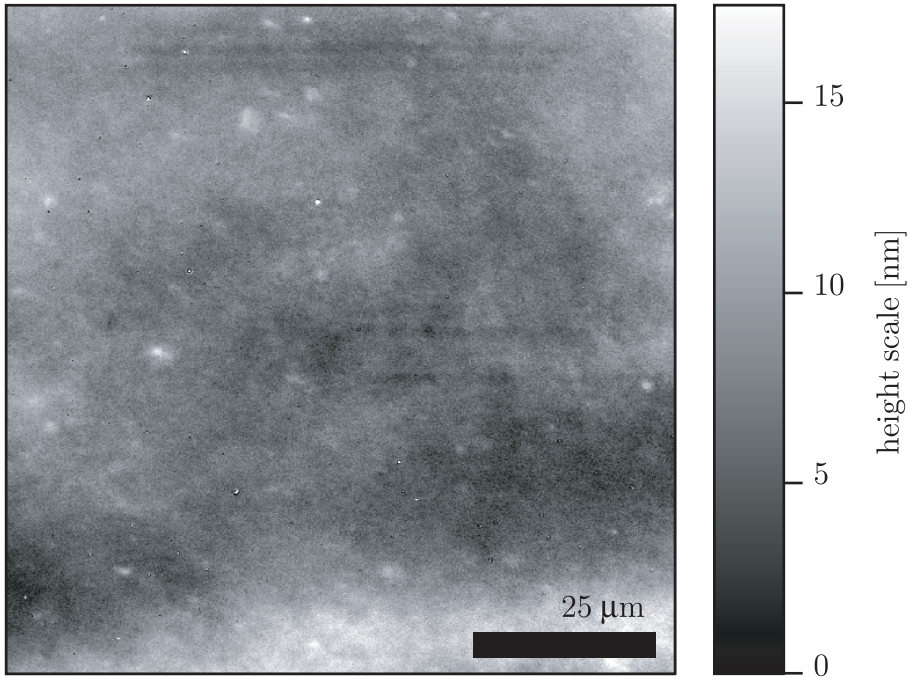

Figure 4.7: Height reconstruction of a RICM image of a film of cross-linked PDMS on glass immersed in water. The maximal deviation of the height from the average value of a profile line of 100 µm length is 14±8 nm on average.

A sample of cross-linked PDMS on glass was put on the stage of a RIC microscope. The measurement chamber was filled with water during observation. No change in its structure (like dewetting) could be seen upon immersion. The height of the film's surface under water was reconstructed (see Fig. 4.7).

The surface appears to be very smooth. The lateral pixel-to-pixel fluctuation has a magnitude of 1.7 nm which is in the same order of magnitude as the time-dependent fluctuations of the height of a single pixel (1.8 nm, see Section 5.5.4). Moreover when observing a drop of PDMS on a substrate, the standard deviation of the lateral fluctuations of the solid surface and the lateral fluctuations of the smooth surface of the static drop both match this value. This implies that the surface of the cross-linked PDMS is as smooth as that of the drop of liquid PDMS, i. e. completely smooth within the resolution of the RICM. An illustration of these fluctuations of the height profile is shown in Fig. 4.8 (a) – (b).

Apart from these pixel-to-pixel fluctuations the surface exhibits smooth height fluctuations on length scales of 100 µm. The maximal deviation of these fluctuations from the average value of a profile line of 100 µm length is 14±8 nm on average. An example is given in Fig. 4.8 (c) – (d). These smooth variations are in the same order of magnitude as determined by AFM. These fluctuations are far too smooth to play an important role in a wetting process.

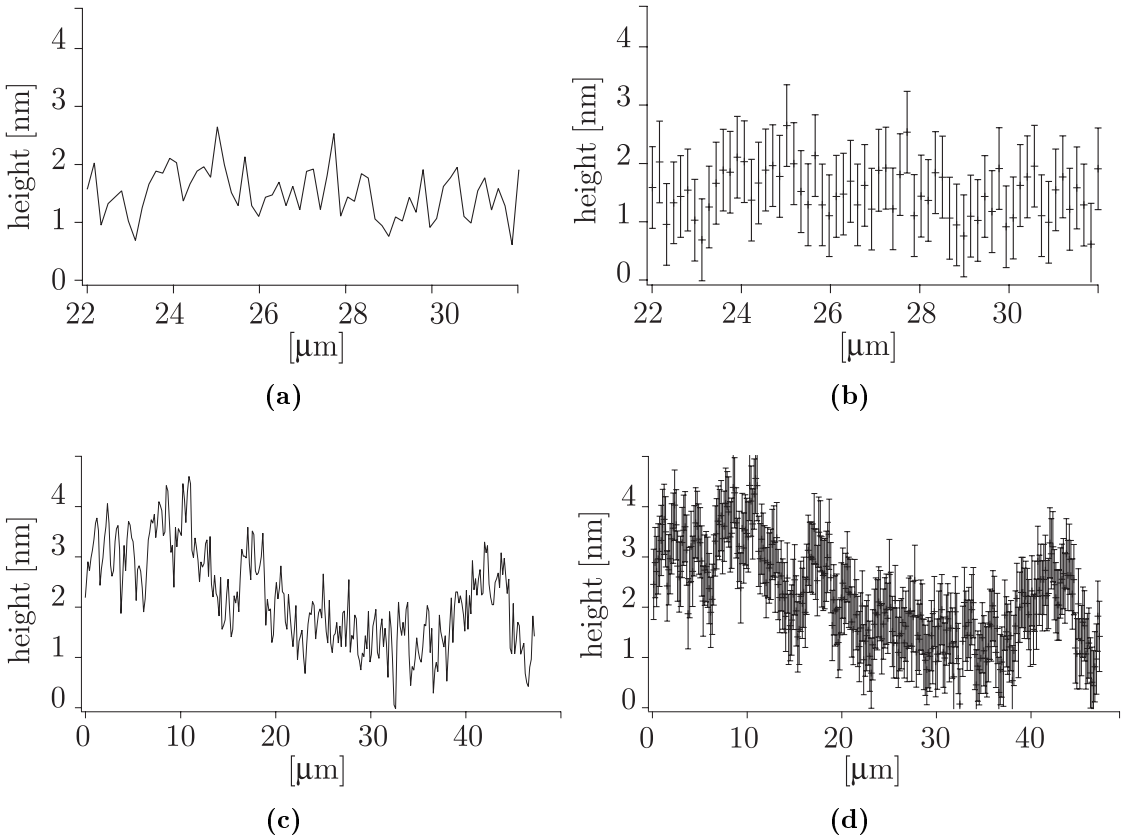

Figure 4.8: RICM height reconstruction profile of a film of cross-linked PDMS on glass immersed in water with ((b) and (d)) and without error bars ((a) and (c)).

a) – b) Fluctuations in height on length scales of 1 µm are in the same order of magnitude as the error and are therefore mainly due to time-dependent variations in intensity. The surface is smooth.

c) – d) Fluctuations in height on length scales of 10 µm are on the order of nm and resemble data from AFM measurements.

4.7 Method of Drop Deposition

Most publications about the behaviour of drops deposited onto a solid substrate deal with drops in the mm range. The deposition of drops in the μm range is not easy to facilitate. For our experiments we used a semi-automated micro-injection system comprising a pressure generating tool (FemtoJet, Eppendorf, Hamburg) and a micro-injector (InjectMan, Eppendorf, Hamburg) which is depicted in Fig. 4.9.

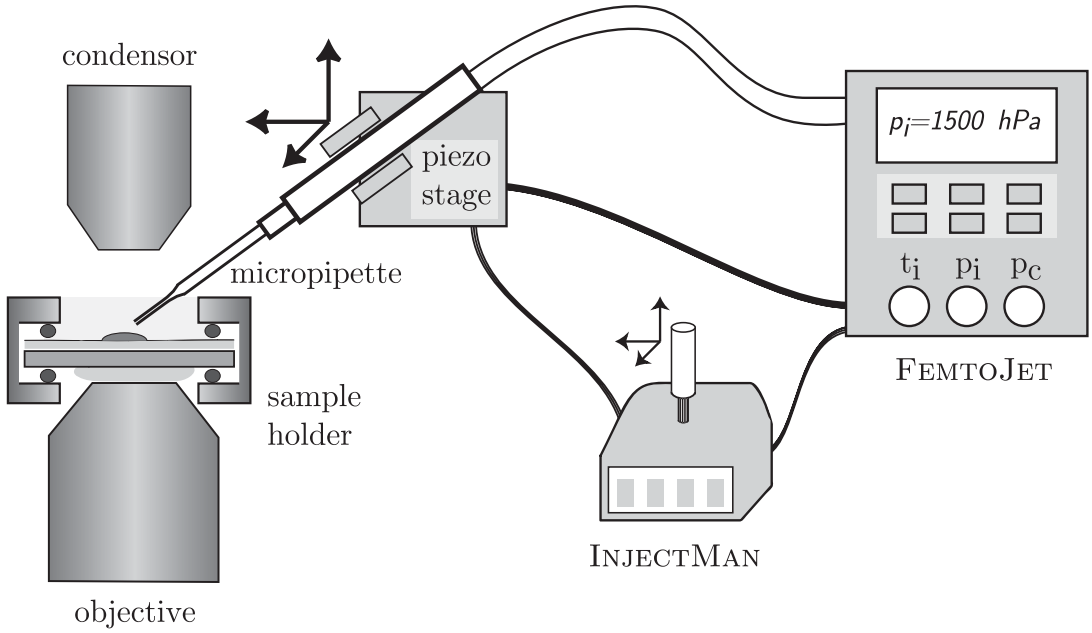

Figure 4.9: The micro-injection setup consists of a pressure generating FemtoJet and a micromanipulation unit, the InjectMan. The micropipette is moved by a piezo stage which is controlled either by joystick or by a semi-automated injection programme. The injection pressure p_i, time of infection t_i and compensating pressure p_c can be set digitally.

The FemtoJet is regularly used as a micro-injector for injecting aqueous solutions into cells [Graessmann and Graessmann, 1983]. It features an integrated compressor as an independent pressure supply. In combination with the InjectMan it is possible to perform semi-automatic micro-injection into adherent cells. The micropipette can be either moved by a piezo stage electronically connected to the InjectMan joystick or a "semi-automatic" micro-injection can be performed which allows a coordinated process of manipulation and injection. This includes a high speed axial injection movement towards the substrate/the cell, the injection of liquid into the cell and a backwards motion.

As the PDMS oil used has a much higher viscosity than water, the filling of the micropipette and the injection had to be performed in a different way than described in the manual.

The micropipettes used (Femtotips, Eppendorf, Hamburg) had an inner diam-

eter of 0.5 µm. A 1 ml single-use syringe (HENKE-SASS, WOLF GMBH, TUTTLINGEN, GERMANY) was filled with app. 0.2 ml of the fluid PDMS. A thin hypodermic needle (STERICAN, Size 18, 0.45 × 25 mm, BRAUN, MELSUNGEN, GERMANY) was attached. A teflon tape folded ten times (PTFE Gewindedichtband) was pierced with the needle to form a soft seal to prevent air leakage when pressing the PDMS into the Femtotip. The needle was then carefully plunged into the Femtotip until its plastic top touched the top of the Femtotip with the teflon tape in between as a seal. The needle was pressed against the Femtotip to prevent air leakage. The PDMS was then deposited into the very end of the micropipette by applying maximum pressure with the syringe.

The cover slip coated with cross-linked PDMS was put into a measurement chamber that held it and had a rim that allowed water to be added from above. The substrate was put onto the stage of an inverted microscope AXIOVERT 200 (ZEISS, Göttingen, Germany). All measurements were performed at room temperature.

The Femtotip was attached to the InjectMan and brought into the field of view of the microscope. An Achroplan 10 × /0.25 objective (ZEISS, Göttingen, Germany) was used to find the end of the pipette and focus. The pipette was then adjusted so the tip was only slightly above the cover slip. The measurement chamber was then filled with app. 1 ml of millipore water.

Then the objective revolver was carefully turned and a high aperture objective (63×/1.25 ANTIFLEX PLAN-NEOFLUAR PH3 OIL-IMMERSION, ZEISS, Germany) in RICM mode was installed.

The micropipette was slowly moved downwards until a dark spot on the substrate appeared indicating that the pipette had reached the surface. This position was set as the injection height and the pipette was moved slightly up. A different place on the substrate for the measurement was chosen. After pressing the *inject* button of the FemtoJet, the injection movement was started: the pipette moved automatically downwards, a small drop of fluid PDMS was deposited onto the substrate and the pipette was brought upwards again. The injection pressures used varied between $700\,\mathrm{hPa} < p_i < 5000\,\mathrm{hPa}$; the time of injection was $0.5\,\mathrm{s} < t_i < 2.5\,\mathrm{s}$. The compensating pressure p_c, which acts when the system is idle to prevent backflow, was set to $p_c = 0$ as the PDMS oils used were very viscous and the backflow was therefore irrelevant.

The details of the microscopic setup for observation of the drop are described in Section 5.6.

Chapter 5

Reflection Interference Contrast Microscopy - a Valuable Tool for Wetting Studies

5.1 Introduction

Wetting phenomena have attracted considerable scientific attention in recent years due to their technological importance as well as to novel theoretical and experimental developments. The usual methods for investigation of liquid drops or films on surfaces include axissymmetric drop-shape analysis ADSA [Río and Neumann, 1997; Song and Springer, 1996a,b], ellipsometry [Heslot et al., 1989], atomic force microscopy (AFM) [Haferl et al., 2001] but also more exotic techniques like surface acoustic waves [Newton et al., 1995], interferometry using differential-interference contrast (DIC) [Be'er and Lereah, 2002] and analysis of intensity distributions of refraction patterns [Thomas et al., 1995].

Drop shape measurements of drops in the picoliter regime on a solid substrate under water with good time resolution cannot be achieved by any of the above mentioned methods. This might be one of the reasons why there has not been much research on wetting phenomena in ambient water. In this work we apply the interferometric technique of Reflection Interference Contrast Microscopy (RICM) to the investigation of wetting phenomena in ambient water.

Micro-interferometry is a versatile technique to visualize vertical distances from a few nanometers to a few hundred nanometers between two surfaces. The method of RICM has been widely used in biophysics to observe the behaviour of objects like cells and vesicles close to a wall [Marchi-Artzner et al., 2001; Marx et al., 2002] but also to study wetting processes [Nissen et al., 1999]. It is a powerful tool for the study of living cells and other biological objects as the measurement can take place in ambient air as well as under water or in biological buffer. The combination of a lateral resolution of less than 1 µm and a vertical resolution in the nm range make it a powerful tool for wetting studies. From its first application to biological physics

in the 1950s [Abercrombie and Ambrose, 1958] the technique has been improved continuously.

In this chapter we will show in detail the working principle of RICM and apply it to the reconstruction of a drop shape. The resolution and error of measurement of such a drop shape measurement are also elaborated.

5.2 Reflection Interference

The basic principle of RICM is shown in Fig. 5.1. On a glass substrate is a film of cross-linked polymer with a drop of polymer oil on top. The glass substrate is illuminated from below (beam I_0). Light is both reflected at the interface between glass and polymer (beam I_1) and the upper surface of the polymer (beam I_2). As the difference in refractive index between cross-linked polymer and polymer oil is very small, the reflection at this interface can be neglected (see page 43) the same holds for the interface between immersion oil and bottom surface of the glass.

Light reflected from the glass/polymer interface (beam I_1) interferes with light reflected from the upper surface of the polymer (beam I_2). The resulting intensity fringe pattern I contains information on the height $h(x, y)$ of the polymer at the lateral position (x, y) and is described by:

$$I(\vartheta) = I_1 + I_2 + 2\sqrt{I_1 I_2}\cos[2kh(x,y)\cos\vartheta + \phi] \tag{5.1}$$

where ϑ is the angle of incidence and $k = \frac{2\pi n}{\lambda}$ is the wave vector for the wavelength in vacuum λ in a medium with refractive index n. The constant phase $\phi \leq \pi$ accounts for the phase shift due to the reflection at the interface and depends on the angle of incident light as well as on the polarization.

5.3 Antiflex Technique

The intensity of the reflected light is rather low for most relevant biological interfaces like polymers, membranes and aqueous solutions. The reflective coefficient r which describes the maximum reflected intensity at an incident angle of 0° is given by:

$$r = \frac{(n_1 - n_2)^2}{(n_1 + n_2)^2} \tag{5.2}$$

The reflective coefficient can be calculated for the relevant interfaces are (see Fig. 5.2):

- Immersion oil/glass interface interface: $r_{imm.oil/glass} \simeq 7 \times 10^{-6}$ with $n_{imm.oil} = 1.518$ and $n_{glass} = 1.526$.
- cross-linked PDMS/fluid PDMS interface: $r_{PDMS/PDMS} \simeq 3.6 \times 10^{-5}$ with $n_{PDMS/CL} = 1.420$ and $n_{PDMS/F} = 1.403$

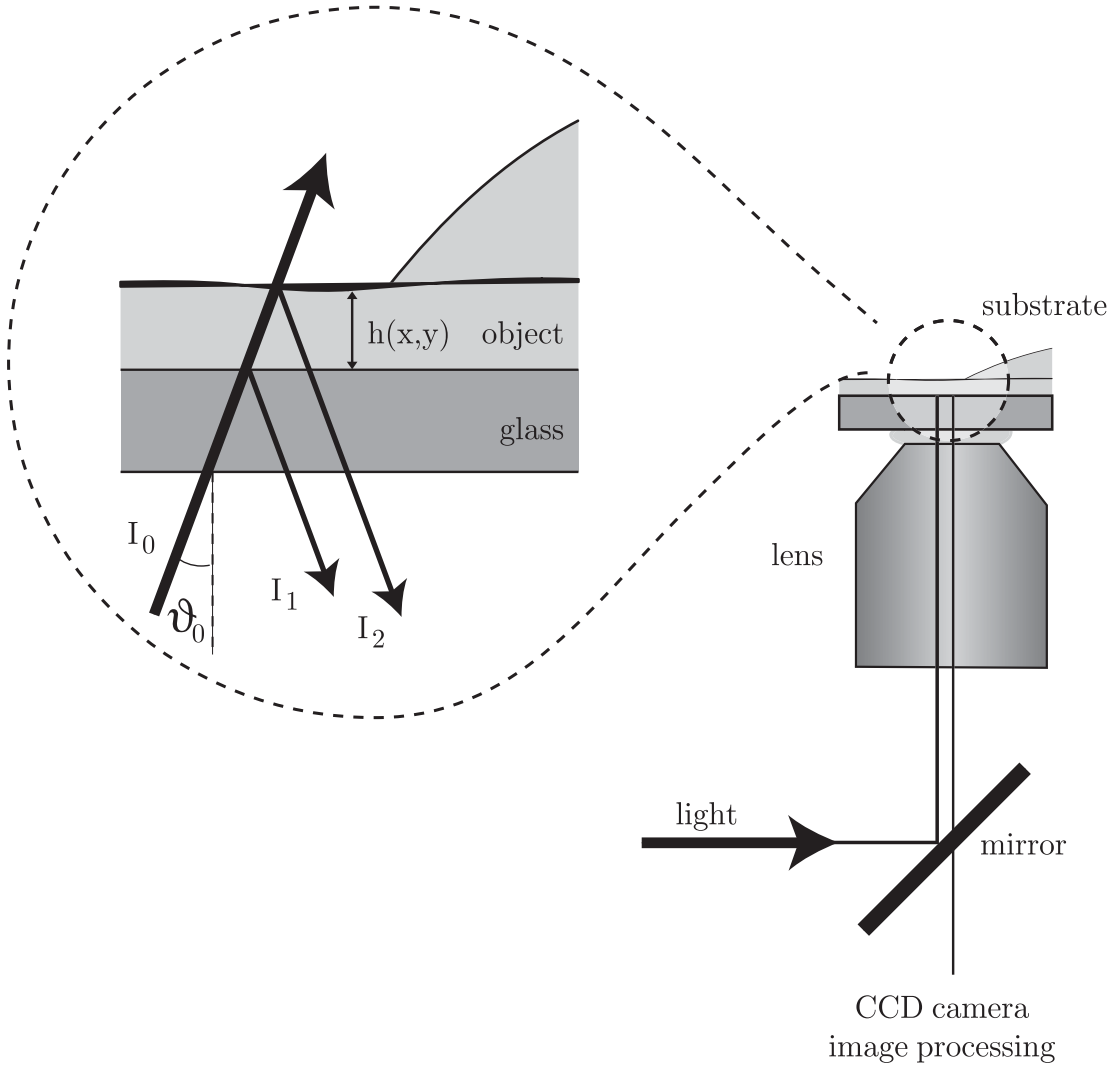

Figure 5.1: The working principle of RIC microscopy. Light is reflected at different interfaces and interferes with a phase shift acquired by propagating along different optical paths.

- Glass/cross-linked PDMS interface: $r_{glass/PDMS} \simeq 1.3 \times 10^{-3}$ with $n_{glass} = 1.526$ and $n_{PDMS} = 1.420$
- fluid PDMS/water interface: $r_{PDMS/water} \simeq 0.7 \times 10^{-3}$ with $n_{PDMS} = 1.403$ and $n_{water} = 1.33$
- cross-linked PDMS/water interface: $r_{PDMS/water} \simeq 1.07 \times 10^{-3}$ with $n_{PDMS} = 1.420$ and $n_{water} = 1.33$

As can be seen, the reflection at the interface between fluid PDMS and cross-linked PDMS can be neglected as the reflective coefficient for this interface is two orders of magnitude smaller than that of the other interfaces due to the minor difference in the refractive indices of cross-linked PDMS and fluid PDMS.

However light reflected by any component of the microscope is more intense than

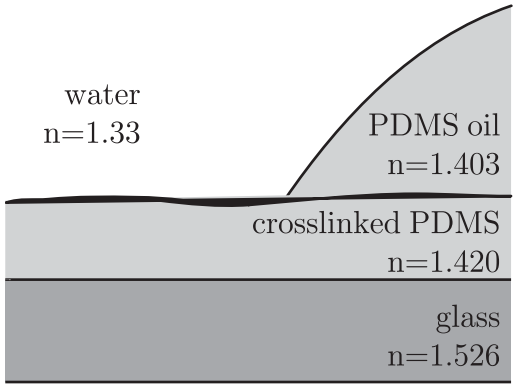

Figure 5.2: Refractive indices of the used system. Measurements of the refractive index of pure PDMS oil and the used PDMS mixtures showed no difference and confirmed the manufacturer's data. The refractive index of the cross-linked polymer was measured by ellipsometry to be 1.4196±0.0014 (at 632.8 nm). The value for glass cover slides was taken from the glass manufacturer (SCHOTT, Mainz, Germany), the respective value for water from literature [Gerthsen, 1997].

the interference pattern by orders of magnitude. To overcome this problem Ploem [1975] developed the antiflex technique which blocks all light scattered within the microscope. The path of light in the microscope is extended by two polarizers and a quarter-wave plate (see Fig. 5.3).

The light from the microscope's light source is turned into linearly polarized light by the polarizer P_1. A quarter-wave plate put into the optical pathway near the substrate transforms the polarization again so the light is circularly polarized afterwards.

Now a feature of circularly polarized light is used: at every following reflection at one of the various interfaces the direction of the polarization is switched. This is true for the reflection at a boundary to a material of higher as well as of lower refractive index. When light is reflected at a boundary to a material with higher refractive index at small incident angles the phase of the component perpendicular to the plane of incidence undergoes a phase shift of π, whereas the component $E_{\parallel}$ parallel to the plane of incidence is unaltered. At the boundary to a material with lower refractive index the phase of $E_{\perp}$ stays unaltered whereas the phase of $E_{\parallel}$ is shifted by π (Fresnel equations, see [Hecht, 2001]). Therefore reflection at a material with both higher or lower optical index results in a reversal of the direction of the circular polarization.

After this transformation the ray passes the quarter-wave plate a second time and is now transformed to linear polarization perpendicular to that of the incident wavefront. By the use of an analyzer P_2 perpendicular to the first polarizer P_1 only light which passed the quarter-wave plate twice is used for the image formation. Light which is scattered at lenses or other components inside the microscope does not reach the camera.

5.4 Image Formation

This section will focus on the process of image formation by RICM. The concept of coherence will be developed in detail as it is crucial for the formation of interference fringes and estimating the lateral resolution. The problem of height reconstruction from interference fringe images is tackled giving an overview of several methods

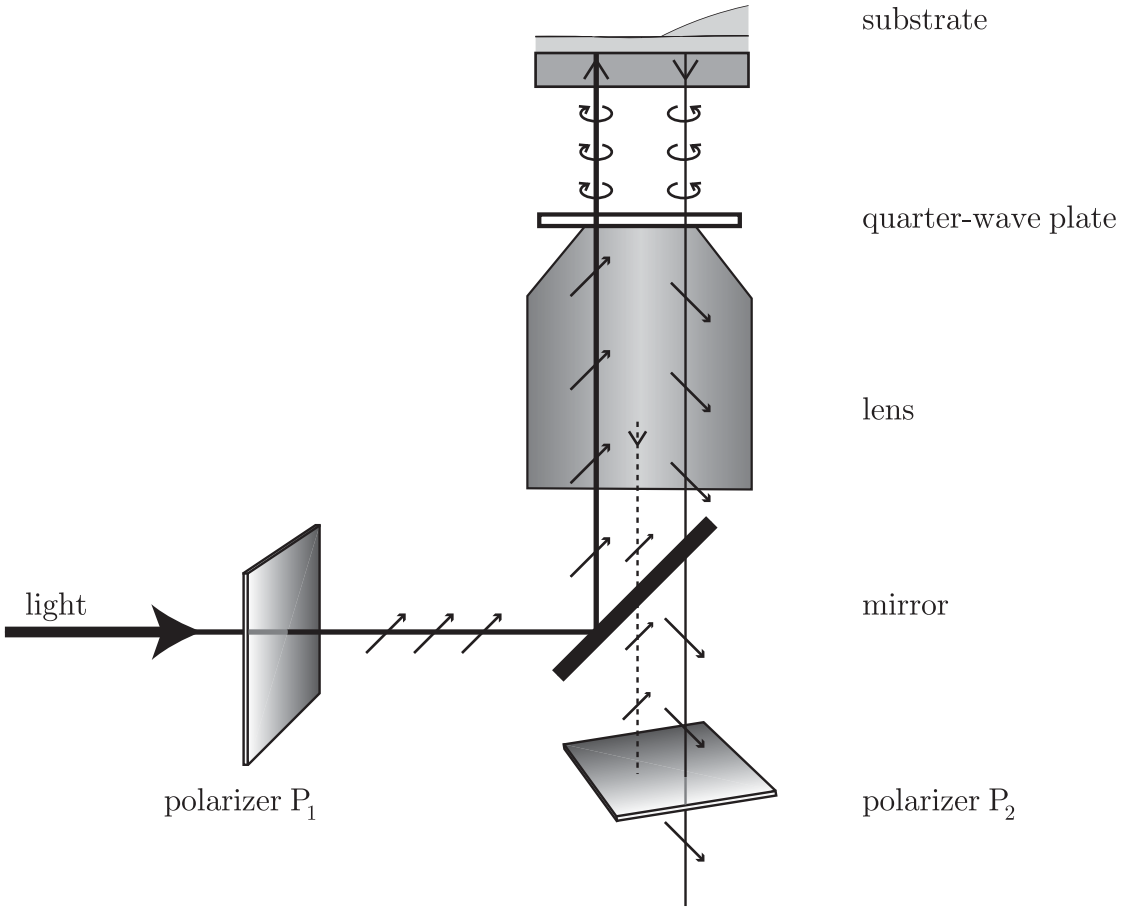

Figure 5.3: Principle of the antiflex technique. Light is first brought into a state of linear polarization by polarizer P_1. After passing the properly aligned quarter-wave plate the polarization is circular. Reflection at any interface within the substrate switches the direction of polarization. Passing the quarter-wave plane a second time the light is linearly polarized with an orientation perpendicular to the state prior to reflection. It can pass the second polarizer P_2 featuring an orientation perpendicular to P_1. Light that is reflected at interfaces within the microscope (center beam) will always maintain its orientation (phase shift 0 or π) and cannot pass polarizer P_2.

with increasing complexity. The process of reconstructing the height of a drop on a substrate is explained in depth.

5.4.1 Coherence and Resolution

Coherence of Light and the Visibility of Interference Fringes

In the following we will first describe the concept of coherence and how it is related to the visibility of interference fringes. For a more detailed treatment see [Pluta, 1988] and [Born and Wolf, 1980], which are also the main sources of this section.

Two rays can only form stable interference patterns if they are coherent, i.e., monochromatic with a constant phase relation [Hecht, 2001]. A real physical light source (apart from lasers), however, consists of a multitude of point sources emitting finite wave trains with no phase correlation. Nevertheless the resulting field obeys coherence conditions within a certain time and a certain lateral width: the coherence time t_c and the coherence length x_c. Combined they form the coherence volume V_c with a plane wave inside, but more or less random phase relations outside of this volume. This is also true for matter waves [Felber et al., 1998].

The measured intensity I of a field $\mathbf{E}$ is $I \propto \langle \mathbf{E} \cdot \mathbf{E}^\star \rangle = \langle \mathbf{E}^2 \rangle$ where $\langle\ \rangle$ denotes the time average[1]. For two interfering wave trains $\mathbf{E}_1$ and $\mathbf{E}_2$ the resulting field is

$$\mathbf{E} = \mathbf{E}_1 + \mathbf{E}_2 \tag{5.3}$$

and

$$\begin{aligned} \mathbf{E}^2 &= (\mathbf{E}_1 + \mathbf{E}_2)^2 \\ &= \mathbf{E}_1^2 + \mathbf{E}_2^2 + 2\mathbf{E}_1 \cdot \mathbf{E}_2 \quad . \end{aligned} \tag{5.4}$$

So for the overall intensity I (apart from a constant factor):

$$\begin{aligned} I &= \langle \mathbf{E}_1^2 \rangle + \langle \mathbf{E}_2^2 \rangle + 2\langle \mathbf{E}_1 \cdot \mathbf{E}_2^\star \rangle \\ &= I_1 + I_2 + I_{12} \end{aligned} \tag{5.5}$$

The last term I_{12} is dependent on the coherence characteristics of the waves and is called the *mutual coherence term*: this term disappears for incoherent waves as the time average over the unrelated phases gives no contribution. For coherent waves the time average does not vanish.

The dependence of the term I_{12} on the coherence of the light is now worked out. Consider light emitted from an extended source σ, travelling through two slits P_1 and P_2 at plane A and interfering at point Q in plane B (shown in Fig. 5.4). We consider the points P_1 and P_2 as the sources of secondary fields $\mathbf{V}_1$ and $\mathbf{V}_2$. The the intensity at point Q is given by:

$$I(Q) = I_1 + I_2 + 2\Gamma_{12}^r(^{(s_2-s_1)}/_c) \quad . \tag{5.6}$$

I_1 and I_2 are the respective intensities for a situation with only one source of secondary field $\mathbf{E}_1$ or $\mathbf{E}_2$ present, $(s_2 - s_1)/c$ is the difference in travel time between the two light paths. $\Gamma_{12}^r(\tau)$ is the real part of the *mutual coherence function*

$$\Gamma_{12}(\tau) = \langle \mathbf{E}_1(t+\tau) \cdot \mathbf{E}_2^\star(t) \rangle \quad . \tag{5.7}$$

$\Gamma_{12}(\tau)$ is the correlation function of a wave $\mathbf{E}_1$ at a time $t+\tau$ with a wave $\mathbf{E}_2$ at a time t.

For two coinciding points ($P_1 = P_2$) we obtain

$$\Gamma_{11}(\tau) = \langle \mathbf{E}_1(t+\tau) \cdot \mathbf{E}_1^\star(t) \rangle \tag{5.8}$$

[1] Only if $t_c < t_{measurement}$, which is true for the used setup.

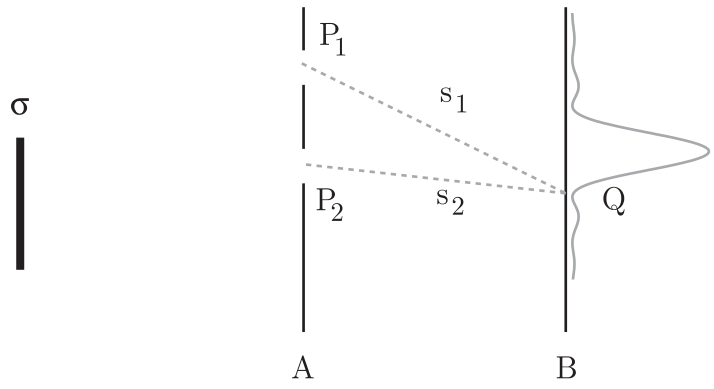

Figure 5.4: Interference of light from an extended source σ.

which is the *self-coherence* of the light vibrations at P_1. If the coherence time t_c (length of a wave train emitted by a source) is long compared to other relevant path times, we can concentrate on the spatial coherence J_{12}

$$J_{12} = \Gamma_{12}(0) \quad = \quad \langle \mathbf{E}_1(t)\mathbf{E}_2^{\star}(t)\rangle \quad . \tag{5.9}$$

The normalized form of Γ_{12} is called the *complex degree of coherence* γ_{12}:

$$\gamma_{12} \quad = \quad \frac{\Gamma_{12}}{\sqrt{I_1 I_2}} \quad . \tag{5.10}$$

The coherence properties of a light source are directly related to the visibility S of the interference pattern. The visibility S is determined by the minimum and maximum intensities of the fringes and relates to the *complex degree of coherence* γ_{12}:

$$S \quad = \quad \frac{I_{max} - I_{min}}{I_{max} + I_{min}} = 2\frac{\sqrt{I_1 I_2}}{I_1 + I_2}\,|\gamma_{12}| \tag{5.11}$$

For strictly monochromatic light $\gamma_{12} = 1$ the diffraction patten shows the maximal visibility S_{max}:

$$S_{max} \quad = \quad 2\frac{\sqrt{I_1 I_2}}{I_1 + I_2} \tag{5.12}$$

If the light is incoherent then $\gamma_{12} = 0$ and the beams do not give rise to an interference pattern: $S = 0$. For cases $0 < \gamma_{12} < 1$ the waves are partially coherent, interference fringes are visible with $S < S_{max}$.

The Van Cittert-Zernike Theorem in Space

So how can there be an interference pattern in plane B if the light from σ is emitted incoherently? This phenomenon was explained quantitatively by Van Cittert and Zernike (CZ-theorem) [Born and Wolf, 1980]. Here it will be illustrated for a simplified setup with a one dimensional light source depicted in Fig. 5.5. The finite length of the emitted wave trains will be neglected, but it can be shown that the following reasoning will hold for a finite correlation time t_c as well.

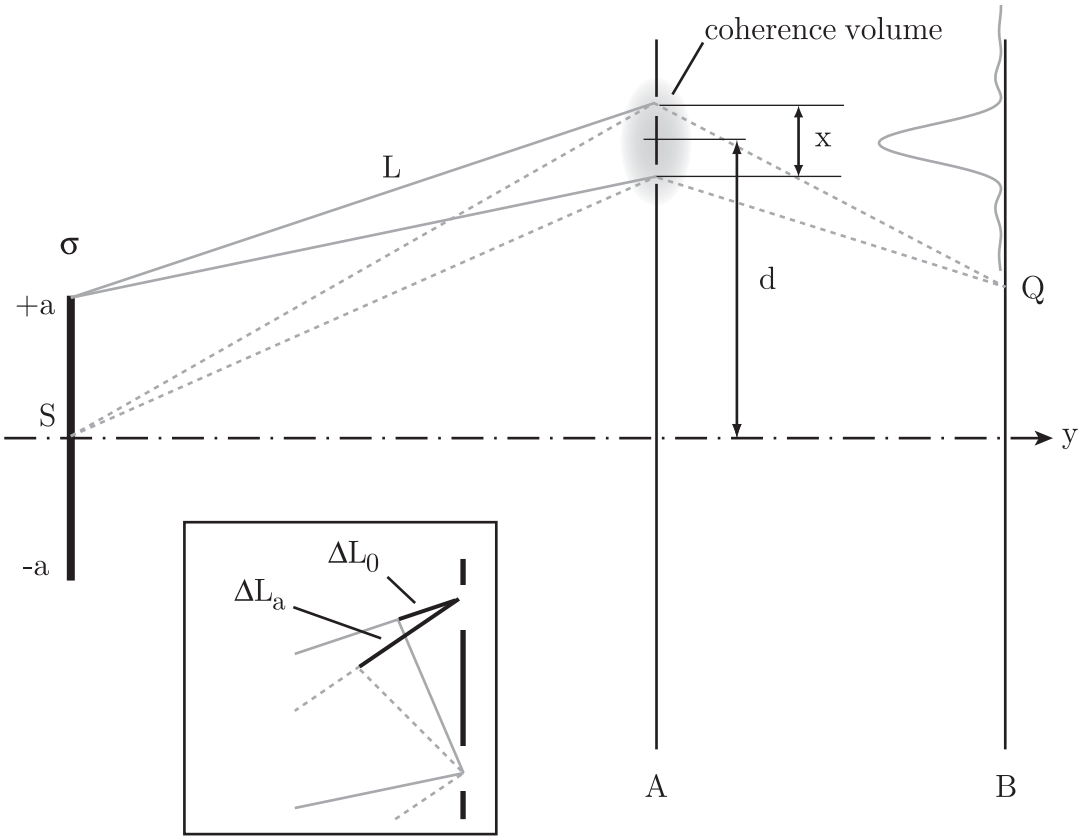

Figure 5.5: Correlation length x_c for an extended light source σ. Spherical waves emitted from a point source S within σ pass through two slits in plane A and give rise to an interference pattern in plane B. For different source points the difference in path length ΔL between σ and plane A should not vary by more than about $\lambda/2\pi$ to ensure good contrast of the diffraction pattern.

A light source σ with a width $2a$ consists of uncorrelated point sources S emitting spherical waves $\Psi(r)$.

$$\Psi(r) \quad = \quad \frac{e^{ikr+\varphi_0}}{r} \quad , \tag{5.13}$$

where k denotes the wave vector, r the distance from the source and φ_0 is a constant phase that varies randomly between the point sources. At a distance L from the source σ there is a plane A with two slits at a distance x. If light travelling through those two slits is coherent an interference pattern will form in plane B.

Light emitted by a point source S_0 in the middle of σ will have acquired a path difference of

$$\Delta L_0 = \frac{d}{L}x \tag{5.14}$$

before even reaching the two slits in plane A. This adds to the phase difference the light will acquire on the way towards screen B. The diffraction pattern will accordingly be displaced laterally.

Another point source at a point $S_{\pm a}$ on the rim of the light source σ will acquire a path difference of

$$\Delta L_{\pm a} = \frac{d \pm a}{L}x \tag{5.15}$$

on its way to plane A. The light of this point source will therefore form an interference pattern that is displaced differently.

The interference patterns of the single point sources are independent of the offset phase φ_0, only the phase variation from the different path lengths has an effect. The interference patterns of the single sources add up to a joint pattern that is independent of the respective φ_0 as well, as the interference images add up incoherently.

If the phase differences ΔL_x are small, the interference patterns from the different point sources will only be displaced by a small amount and will add to an overall interference fringe image with only a small loss of contrast. If the path difference increases the contrast decreases.

The maximal possible variation of path length $\Delta L = |\Delta L_{\pm a} - \Delta L_0|$ is independent of d (see Eqs. 5.15 and 5.14):

$$\Delta L = \frac{a}{L}x \quad . \tag{5.16}$$

A maximal mean phase variation $\Delta\varphi = k \cdot \Delta L$ of $\Delta\varphi = 1$ will still give rise to a good visibility. Taking this value and applying it to Eq. 5.16 we get:

$$x_c = \frac{L}{ka} \quad . \tag{5.17}$$

This is the lateral coherence length x_c of the source σ in plane A.

A more rigorous treatment uses the coherence function J_{12} to come to the same result [Born and Wolf, 1980]:

$$J_{12}(P_1, P_2) = \langle V_1(t)V_2^{\star}(t)\rangle = \int_{\sigma} I(S)\frac{e^{ik(R_1-R_2)}}{R_1R_2}dS \tag{5.18}$$

with the integral over the area of the light source. Expanding $(R_1 - R_2)$ and integrating over a slit gives rise to

$$\gamma = \frac{\sin u}{u} \quad , \qquad u = \frac{ka}{L}x \quad . \tag{5.19}$$

For u=1 the degree of coherence drops from 1 (for x=0) to 0.84 which gives the coherence length from Eq. 5.17.

Application to the Resolution of the RICM

The resolution of the RICM will now be estimated according to the principles discussed above.

For a two dimensional circular light source the degree of coherence γ_{12} for two points P_1 and P_2 is

$$\gamma_{12}(D) = \frac{2J_1(D)}{D} \quad , \qquad D = kx \sin\sigma \tag{5.20}$$

with σ being the steradian of the light source as seen from the middle point between P_1 and P_2 [Pluta, 1988]. $J_1(D)$ is the first order Bessel function of the first kind (see Fig. 5.6) [Abramowitz and Stegun, 1984].

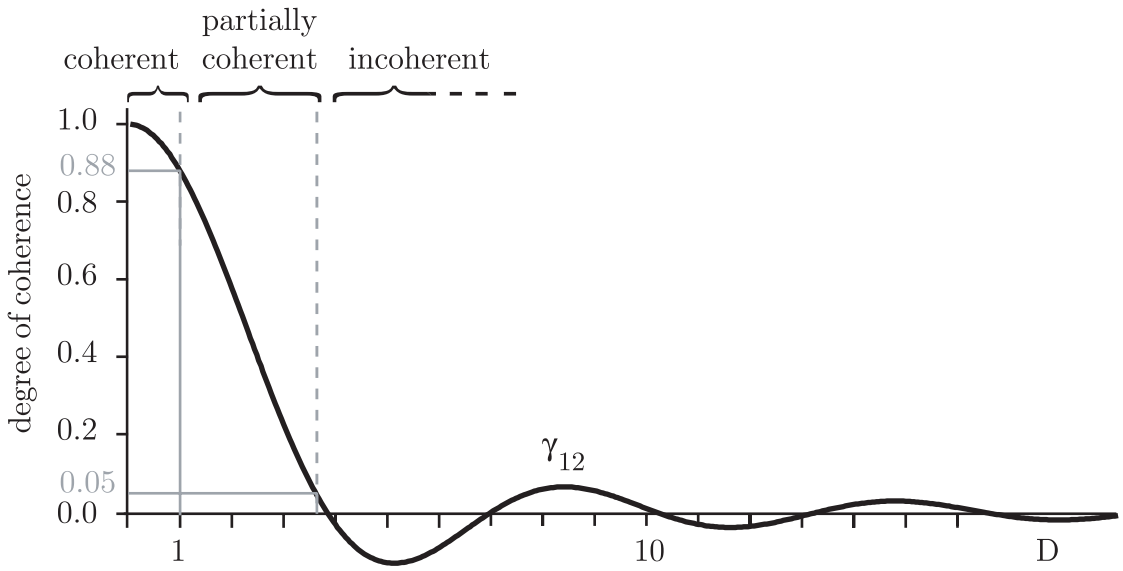

Figure 5.6: Degree of coherence between two points P_1 and P_2 illuminated by a circular light source: $\gamma_{12}(D) = \frac{2J_1(D)}{D}$.
$J_1(D)$: first order Bessel function of the first kind
$D = kx \sin\sigma$
x : distance between the two points
σ: steradian of the light source as seen from the middle point between P_1 and P_2

The two points will be illuminated coherently for $D < 1$ (see Pluta [1988] p.298). For two points in the focal plane of a microscope this results in:

$$x = x_c \leq \frac{\lambda}{2\pi \sin\sigma} = \frac{0.16 \cdot \lambda}{\sin\sigma} \quad . \tag{5.21}$$

Introducing the illuminating numerical aperture INA=$n \cdot \sin\sigma$ and allowing for a refractive index $n \neq 1$ gives:

$$x_c \leq \frac{0.16 \cdot \lambda}{\mathrm{INA}} \quad . \tag{5.22}$$

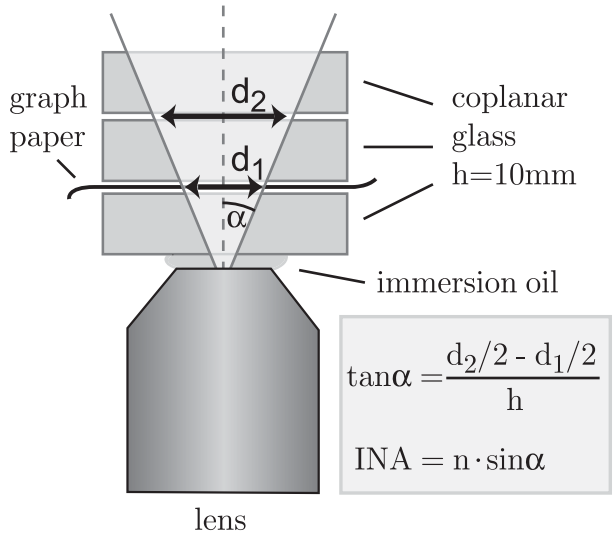

Figure 5.7: Sketch of the method for determining the illumination numerical aperture. Three pieces of coplanar glass of height $h = 10\,\text{mm}$ were put on top of the lens. The diameter of the light cone d was determined at the two faces of the middle glass pane. This was done by alternately placing a piece of graph paper in between the respective panes and then measuring the diameter of the clearly visible light cone. The numerical aperture was then calculated according to the shown equations.

As can be seen in Fig. 5.6 the illumination is still partially coherent for values of $D \geq 1$. According to Pluta [1988] partial coherence is therefore defined for the interval:

$$\frac{0.16 \cdot \lambda}{\text{INA}} \leq x_{pc} \leq \frac{0.5 \cdot \lambda}{\text{INA}} \tag{5.23}$$

For the used setup with a wavelength of $\lambda = 546\,\text{nm}$, the INA was between 0.32 and 0.97 with a frequently used INA of around 0.67. The INA does not enter the height profile calculations but was nevertheless determined according to Fig. 5.7. The values for the corresponding lateral coherence length x_c are between:

$$\text{INA} = 0.32: \quad x_c = 0.27\,\mu\text{m} \leq x_{pc} \leq 0.83\,\mu\text{m} \tag{5.24}$$

$$\text{INA} = 0.67: \quad x_c = 0.13\,\mu\text{m} \leq x_{pc} \leq 0.40\,\mu\text{m} \tag{5.25}$$

$$\text{INA} = 0.97: \quad x_c = 0.09\,\mu\text{m} \leq x_{pc} \leq 0.28\,\mu\text{m} \tag{5.26}$$

Now the very principle of RICM demands that rays reflected at different interfaces interfere, so those rays have to be coherent. For light that is incident with a non-zero angle and is reflected at a wedge-shaped plane as depicted in 5.8(a), this means that the coherence length x_c has to be bigger than the distance x between a ray (ray 1) reflected directly at the bottom interface and another ray reflected at the top interface (ray 2) (see Fig. 5.8(b)).

An easy calculation for the situation in Fig. 5.8(b) where the incident angle was taken as $\alpha_{max} = \arcsin(\text{INA}/n)$ shows that this condition holds only for a small INA, small wedge angles β of the drop and for small heights d. The results for the lowest, the highest and a reasonable INA are shown in Fig. 5.9. It can be seen that the coherence drops rather fast. The calculation only takes into account those two interfering rays with the largest possible lateral incidence distance x in the specific setup. In reality light from the whole light cone will interfere. Therefore this calculation is only an estimate of a lower limit of visibility to illustrate the fact that loss of visibility due to a limited lateral coherence length x_c will occur.

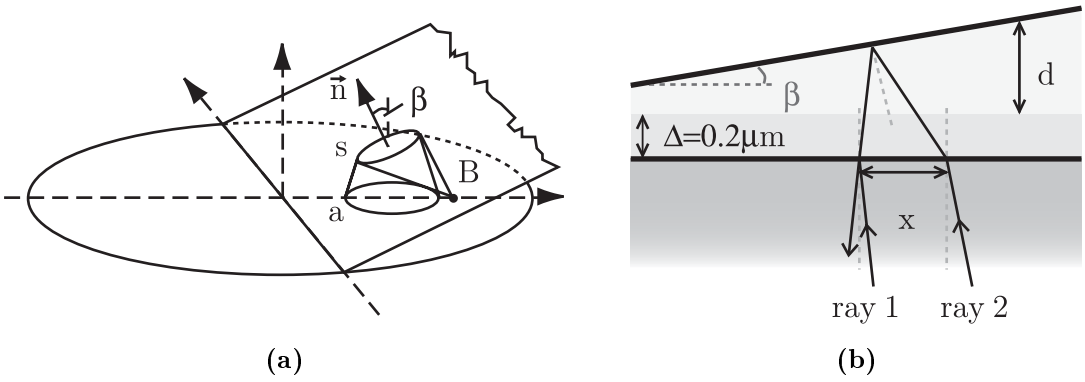

Figure 5.8: Reflection of light with a non-zero INA at a wedge.
(a) Light from patch a is reflected at the slope in patch s and interferes in point B with light reflected directly at point B. Illustration taken from [Wiegand et al., 1998].
(b) Sketch of the situation of a drop of PDMS oil on a substrate. The drop is simplified to be wedge shaped. Interference is only possible if light from *ray* 1 and *ray* 2 is coherent.

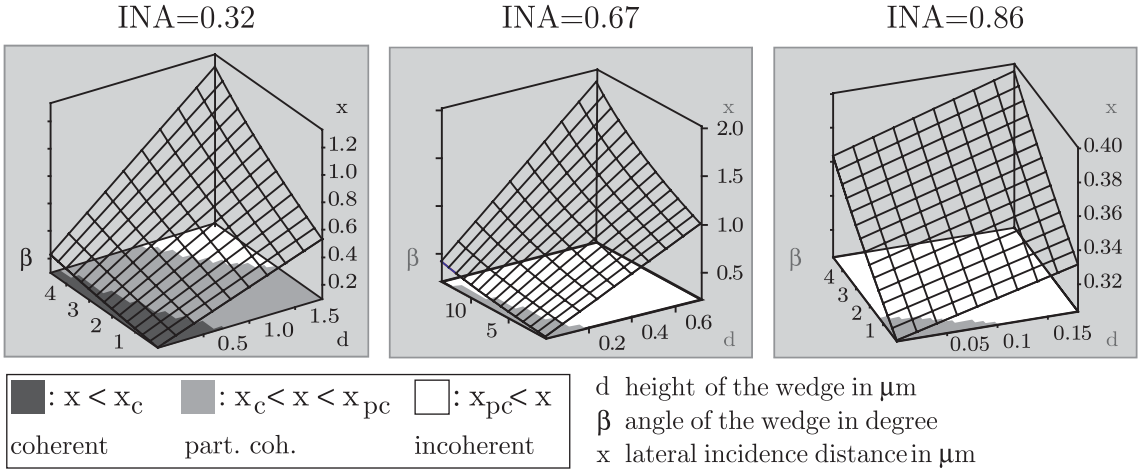

Figure 5.9: Calculation of the maximal possible lateral incidence distance x between two interfering rays for different angles $\alpha_{max} = \arcsin(^{\mathrm{INA}}/_{n})$ of incident light (see Fig. 5.8(b)). If x is smaller than the lateral coherence length x_c, the visibility S (see Eq. 5.11) of the interference fringes will be maximal. If x is larger than the lateral coherence length x_c the visibility S will decrease.

What does this imply for the resolution of a microscope? One point in the focal plane P will produce an Airy pattern in the image plane with the intensity:

$$I = \left[\frac{2J_1(Y)}{Y}\right]^2 \tag{5.27}$$

$$Y = \frac{2\pi}{\lambda} n \sin\sigma \cdot \frac{y'}{M_{ob}} \tag{5.28}$$

where J_1 denotes the first-order Bessel function of the first kind. Y is known as the Airy optical unit with n the refractive index of the space between the object point P and the objective, σ the object-side aperture angle, M_{ob} the magnification of the

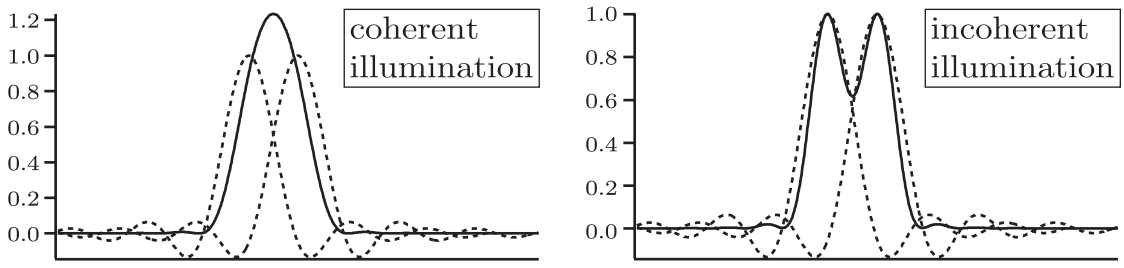

Figure 5.10: Whether two points in the focal plane can still be distinguished in the image plane depends also on the coherence between those two light sources. The interference pattern of two Airy discs is different for coherent and incoherent illumination. As can be seen the resolving power is better for incoherent illumination.

objective and y' the distance from the center of the Airy pattern.

The resolution of a microscope is defined as the smallest distance ϱ between two points in the focal plane such that these two points can still be distinguished as separate entities in the image plane. As the Airy patterns of those points might also interfere, the combined intensity is

$$I' = \left[\frac{2J_1(Y_1)}{Y_1}\right]^2 + \left[\frac{2J_1(Y_2)}{Y_2}\right]^2 + 2\gamma_{12}\frac{2J_1(Y_1)}{Y_1}\frac{2J_1(Y_2)}{Y_2} \tag{5.29}$$

where γ_{12} is the degree of coherence. As can be seen in Fig. 5.10 this implies that the resolution is better for incoherent illumination than for the coherent case.

Taking the intensity loss between the two inner maxima of the respective two Airy discs as a criterion whether two points can still be distinguished, the minimal distance ϱ in the focal plane can be calculated according to the Rayleigh criterion[2] to be:

$$\varrho_{ic} = \frac{1.22 \cdot \lambda}{2n \sin \sigma_{NA}} = \frac{0.61 \cdot \lambda}{\mathrm{NA}} \quad \text{for incoherent illumination} \tag{5.30}$$

$$\varrho_{co} = \frac{1.63 \cdot \lambda}{2n \sin \sigma_{NA}} = \frac{0.82 \cdot \lambda}{\mathrm{NA}} \quad \text{for coherent illumination} \tag{5.31}$$

$$\tag{5.32}$$

where NA is the numerical aperture of the objective. With a numerical aperture of NA= 1.25 of the used setup, this gives a resolution of

$$\varrho_{ic} = 0.264\,\mu\mathrm{m} \quad \text{for incoherent illumination,} \tag{5.33}$$

$$\varrho_{co} = 0.355\,\mu\mathrm{m} \quad \text{for coherent illumination.} \tag{5.34}$$

[2]According to the Rayleigh criterion two points are considered to be resolved if the center of one Airy pattern coincides with the first dark ring of the other. This holds only for incoherent light but can be extended to cover coherent illumination as well.

This value only takes two point sources in the focal plane into account. In RICM, however, each of those point sources will be the result of a multitude of interfering rays that got reflected at a whole patch of the observed interface (patch s in Fig. 5.8). For small angles the dimensions of this patch can be approximated by the maximal lateral incidence distance x as before.

If the size of the patch x is smaller than the lateral coherence length x_{pc}, the two point sources resulting from the interference of light will be partially coherent if they are less than x_{pc} apart. In this case the resolution will be $\varrho = \max(\varrho_{co}, x)$.

If the size of the patch x is bigger than x_{pc} only light reflected at parts of the patch that are within the lateral partial coherence length x_{pc} interferes. The size of this "active" patch x_a is $x_a = \max(x_{pc}, x) = x_{pc}$. The resolution cannot be better than the size of this patch. Therefore the resolution cannot be better than x_{pc} which implies incoherent resolution. The resulting resolution is $\varrho = \max(\varrho_{ic}, x_{pc})$.

A model calculation of the resolution ϱ according to these principles for different INAs is shown in Fig. 5.11. The resolution increases with the INA as the coherence length decreases. The resolution for an $INA = 0.67$ is about $\varrho = x_{pc} = 0.4\,\mu\text{m}$.

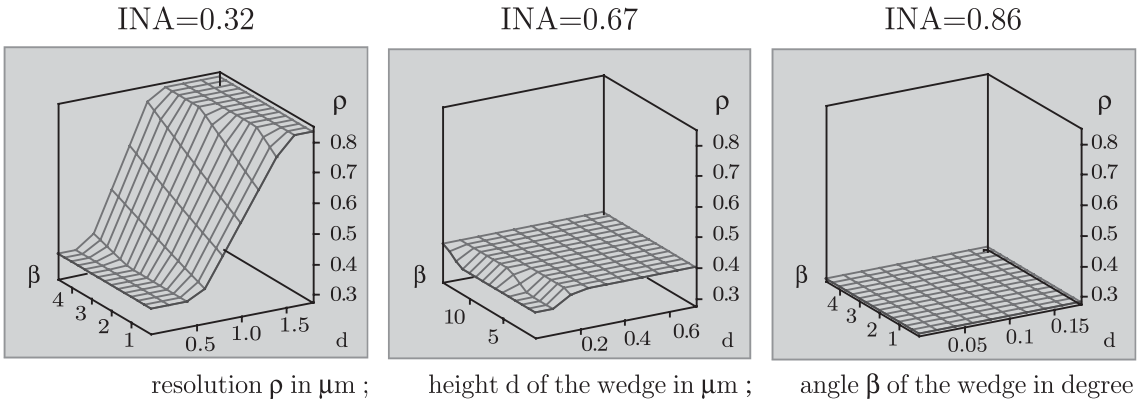

Figure 5.11: Calculation of the resolution of the RICM for different INAs. The resolution increases with increasing INA.

In a situation with a big slope (high gradient) of the substrate the interference fringes will be accordingly very narrow. If the distance of the fringes approaches the resolution of the microscope this will result in a damping of the visibility. A good derivation of this damping of contrast for high gradients can be found in [Rädler and Sackmann, 1993].

5.4.2 Methods of Height Profile Reconstruction

The interference pattern of light reflected at different interfaces depends both on the reflectivity of the interfaces and on the geometry of the setup. Reflection of a light cone with a finite INA at a curved interface will lead to a change in the angular distribution of the light cone. This renders the reconstruction of the height profile from the measured intensities exceedingly difficult. Therefore it is recommended

to simplify the system and use more or less advanced models as a basis for the calculation.

There are three different approaches of increasing complexity for the calculation of the height profile reconstruction from the measured intensity (see Fig. 5.12).

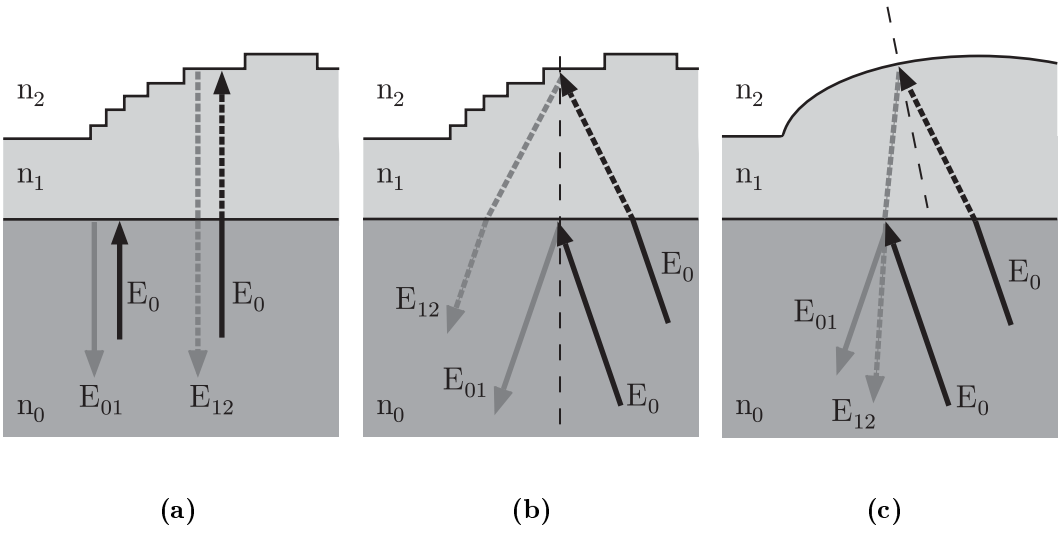

Figure 5.12: Sketches of the different approaches for the height reconstruction of RICM images:
(a) Simple theory considers only light which enters the sample in direction normal to the plane of the substrate. All interfaces are assumed to be parallel to each other.
(b) Finite-aperture theory accounts for all angles appearing in the illumination cone of a non-zero INA. The interfaces of the substrate are assumed to be parallel to each other.
(c) Non-local theory allows for an illumination cone of non-zero INA and reflection at non-parallel interfaces.

Simple Theory

The Simple Theory considers only light which enters the sample in a direction normal to the plane of the substrate. All interfaces are assumed to be parallel to each other. No divergence of the incident and reflected beam is taken into account (see Fig. 5.12(a)). The resulting intensities are of the form:

$$I(h) \;=\; I_1 + I_2 - 2\sqrt{I_1 I_2}\cos\left(2\frac{2\pi}{\lambda}n_1 h\,(x)\right) \tag{5.35}$$

where n_1 is the refractive index of the PDMS film. Even though this approach is based on a very simple model it is sufficient for calculations of small relative height differences of systems with low inclination [Wiegand et al., 1998].

Finite-Aperture Theory

The finite-aperture theory [Gingell and Todd, 1979; Rädler and Sackmann, 1993] accounts for a light cone incident under a maximal angle $\alpha = \arcsin(^{\mathrm{INA}}/_{n})$ and reflected at interfaces parallel to each other (see Fig. 5.12(b)). Different rays from within the illumination cone acquire a relative phase shift which leads to a reduction in contrast. The finite-aperture theory takes care of this effect by incoherent summation of the incident intensity $I(\delta)$ over all angles of illumination using equation 5.1. Following Rädler and Sackmann [1993] this leads to a resulting intensity of

$$I = 4\pi \sin^2\left(\frac{\alpha}{2}\right)\left[I_1 + I_2 + 2\sqrt{I_1 I_2}\,\frac{\sin(2kh)\sin^2(\alpha/2)}{2kh\sin^2(\alpha/2)}\,\cos\left[2kh\left(1-\sin^2\left(\frac{\alpha}{2}\right)\right)\right]+\sigma\right] . \tag{5.36}$$

As the intensity in equation 5.36 is dependent on the initial aperture, the visibility S (compare equation 5.11) decreases with increasing aperture and increasing height of the substrate.

This theory cannot give an analytical expression for the height of the substrate in terms of the intensity.

Non-Local Theory

The non-local theory, developed by Kühner [1996], is the most exact theoretical description of the formation of an RICM image which takes into account finite illumination aperture angles as well as the reflection of light from curved surfaces (see picture 5.12(c)). Its main advantage is the exact determination of absolute object-substrate distances for objects with known shape. The theory cannot be applied to the reconstruction of unknown shapes.

The numerical procedures are demanding, but a comparison between the finite-aperture theory and the non-local theory by Wiegand et al. [1998] led to the introduction of a simple correction factor k. The correction factor k links the angle α_{simple} of the object obtained by using the simple theory to the angle $\alpha_{non-local}$ obtained by using the non-local theory:

$$k = \frac{\alpha_{non-local}}{\alpha_{simple}} \tag{5.37}$$

Non-local theory correction factors were used for the reconstruction of drop profiles from RICM images in all cases. The details of the calculations for the specific setup are given in Section 5.5.3.

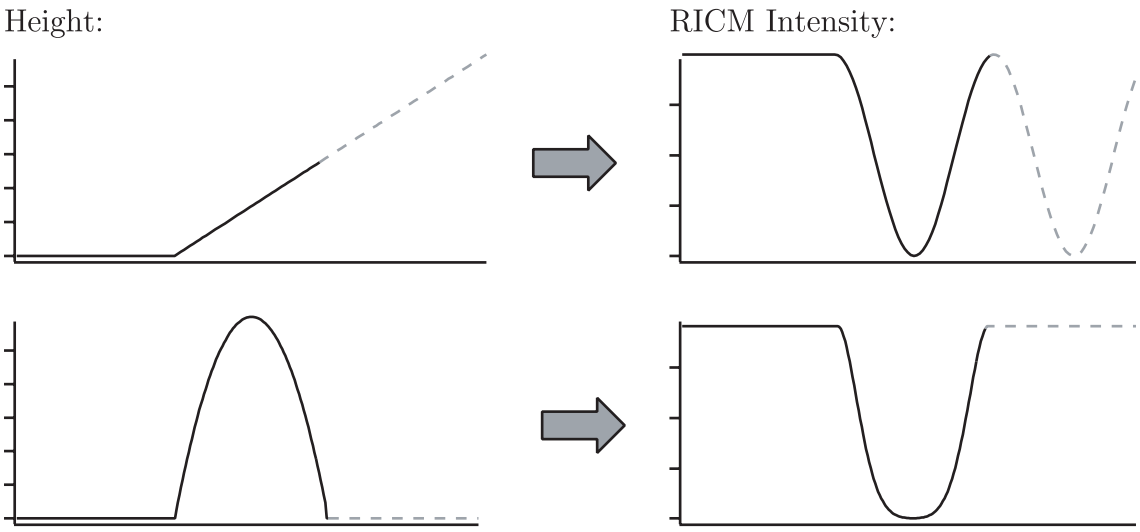

Figure 5.13: The RICM intensity profile can only be interpreted correctly if the overall shape of the observed object is known. Depicted is an example where both a simple wedge and a height peak will result in an intensity peak of the interference fringe image.

5.5 Drop Shape Reconstruction

5.5.1 Drop Shape Reconstruction Using Simple Theory

Height reconstruction of RICM images is only possible if the overall shape of the observed object is known. This is due to the fact that a rise in intensity of the RICM image might represent either a rise or a decline in height depending on the phase of the interference fringes. Also an intensity peak in the RICM image might either represent a height peak or the interference fringe image of a flat rise (see Fig. 5.13). Here the overall shape of the drop profile is clearly given as a flat substrate with the drop sitting on top. As all drops obey spherical symmetry (see Section 5.5.4) it is sufficient to calculate the height profile of a line that runs through the center of the drop.

In all experiments the reconstruction is done using the non-local theory. For this purpose the height profile is first calculated with the simple theory and then adjusted stepwise with a specially calculated correction factor according to the non-local theory (see Section 5.5.3).

For the reconstruction according to the simple theory a line profile passing through the center of the drop is taken from the RICM micrograph (see Fig. 5.14(a)). The intensity profile is a curve alternating between maxima and minima, as shown in Fig. 5.14(b). The optical path difference between an adjacent interference minimum and maximum is $\delta = \lambda/2n$. Therefore the height difference Δh is determined by:

$$\Delta h = \frac{\delta}{2} = \frac{\lambda}{4n_{\mathrm{PDMS}}} \tag{5.38}$$

Calculating Δh for the used setup with $\lambda = 546\,\mathrm{nm}$ and $n_{\mathrm{PDMS}} = 1.403$ for fluid PDMS gives $\Delta h = 97.3\,\mathrm{nm}$. Successively applying Eq. 5.38 to an intensity profile

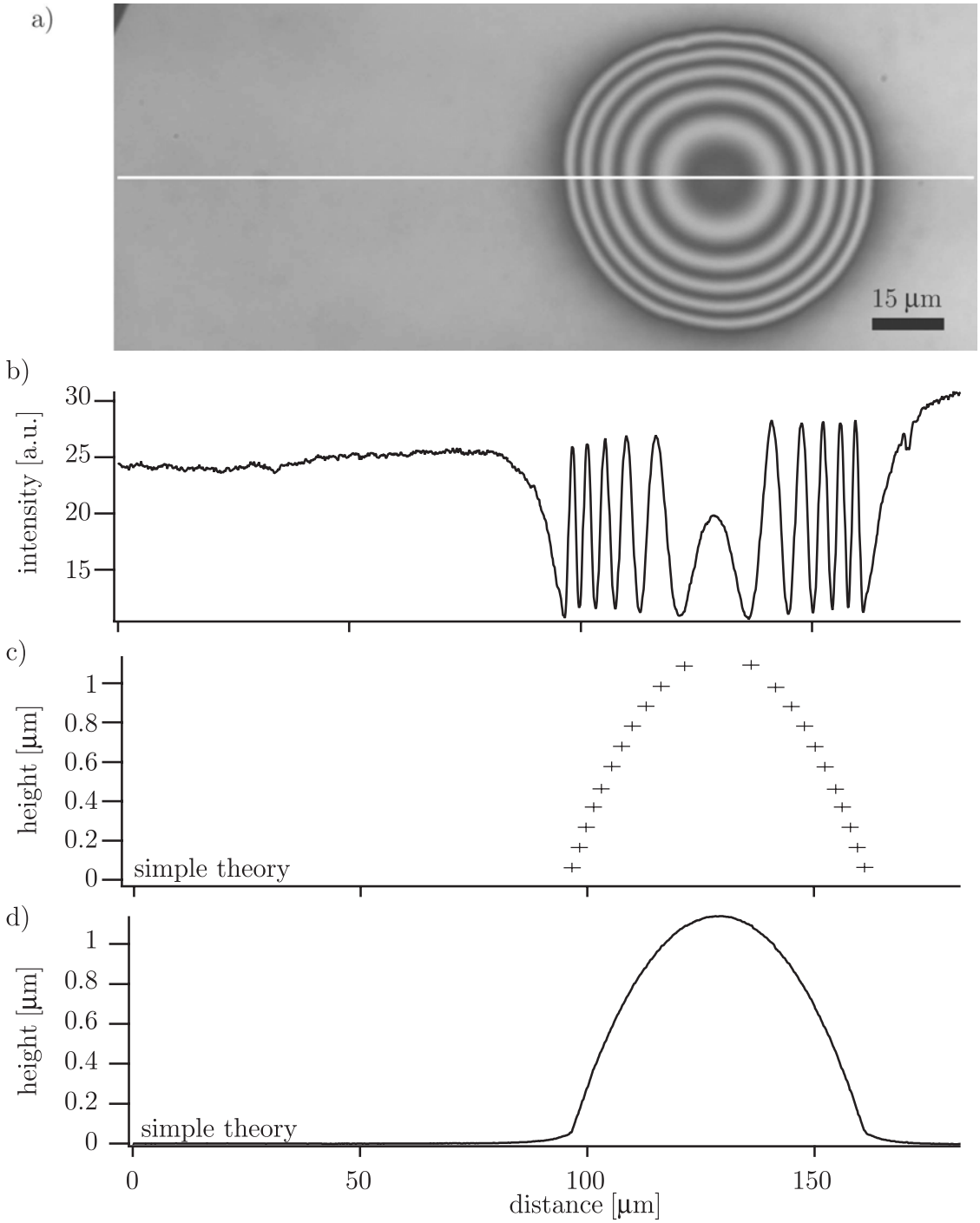

Figure 5.14: a) Raw image of a RICM micrograph of a drop of fluid PDMS on a thin film of cross-linked PDMS under water.
b) Intensity profile $I(x)$ along the white line in the RICM micrograph.
c) Single heights h can be reconstructed from the extreme values according to the simple theory, Eq. 5.38. Note that the height has an unknown offset of $N \cdot \Delta h$.
d) Using the simple theory, the height profile within the intervals can be analyzed by an inverse cosine function (compare Eq. 5.39).

yields single values of the height at the extrema (see Fig. 5.14(c)). The intensity within the intervals is given by a cosine transformation of the height according to Eq. 5.35. Solving this equation for the height and using the easily accessible maximal and minimal intensities I_{max} and I_{min} for normalisation rather than the previously used reflected intensities I_1 and I_2 gives:

$$h(x) = \frac{\lambda}{4\pi n_{\mathrm{PDMS}}} \arccos \frac{2I(x) - (I_{max} + I_{min})}{I_{max} - I_{min}} \tag{5.39}$$

This equation is used for all height profile calculations. A resulting height profile is shown in Fig. 5.14(d).

5.5.2 The Problem of the Missing Extrema

The Virtual Rim Maximum

The reconstruction following the simple theory is straightforward, still we do encounter a problem: we can only calculate the height profile between two adjacent extrema. Looking at Fig. 5.14(b) it can be easily seen that there is no maximum on the left hand side of the first minimum. The intensity drops from a more or less homogeneous plateau to the first minimum. The intensity of the plateau represents the absolute height of the water/cross linked PDMS interface at an average of 207 nm (as determined by ellipsometry) which is less than the absolute maximum needed for the reconstruction (see Fig. 5.15). Therefore this first *virtual maximum* has to be estimated. This is done in two steps: first a sensible starting value for the virtual maximum is derived and then it is readjusted as the drop geometry changes over time.

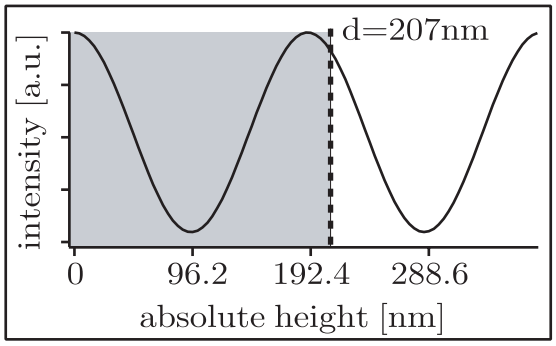

Figure 5.15: RICM intensity versus height of reflecting interface according to the simple theory. The average thickness of the cross-linked film of PDMS is 207 ± 1.6 nm. The height can only increase from there. The maximal observed intensity is equivalent to it's value at 207 nm, which is less than the absolute maximum needed for the reconstruction.

A non-local theory simulation of the RICM picture of a wedge of fluid PDMS on a film of cross-linked PDMS on glass in ambient water was done in collaboration with Felix Linke (see Section 5.5.3 for details). This simulation shows that the first maximum decreases with the contact angle (see Fig. 5.16 (a)). As the *virtual maximum* is used for calculating the horizontal plane next to the drop where the angle is near zero, the intensity of the virtual maximum should be larger than that of all other maxima.

Moreover, the non-local theory simulation also shows that two adjacent maxima differ in intensity by only less than 5%. Comparison of the height of all maxima

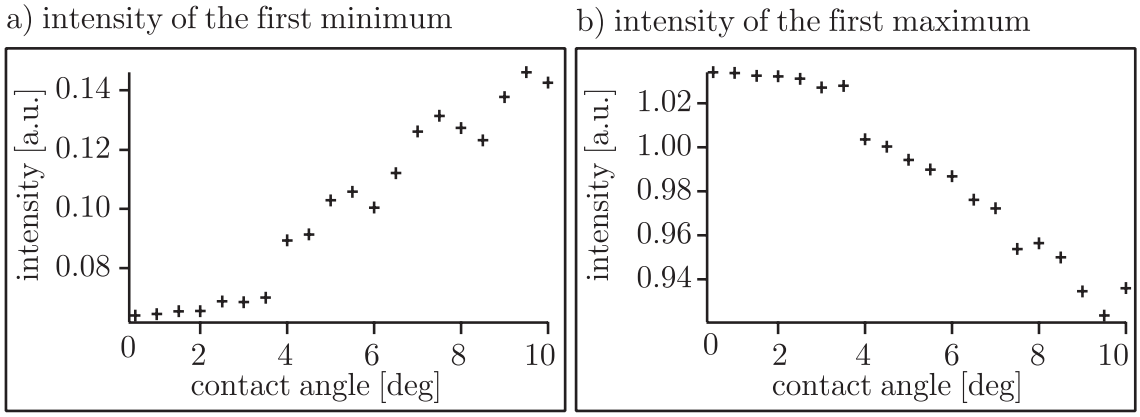

Figure 5.16: Simulation of the intensity of the first minimum respective maximum of a RICM image of a wedge. The intensity of the first minimum increases with the contact angle whereas the intensity of the first maximum decreases. This calculation was performed for a wedge of PDMS on a cross-linked film of PDMS on glass in ambient water for a INA of 0.48.

in a time series of intensity plots of real measurements shows that the difference in intensity of all those adjacent maxima is less than 10%. This implies that the error made by taking the first maximum instead of the *virtual* one is small.

Therefore it is a justifiable first approximation to estimate the missing *virtual* maximum left of the first minimum at the absolute maximal value $I_{max,\,abs}$ of the intensity profiles as the difference to the real unknown value is small[3].

In a time series of an evolving drop the value of the first minimum also changes as the contact angle changes (see Fig. 5.16 (b)). For a fixed value $I_{max,\,abs}$ of the first virtual maximum this means that the scaling factor in Eq. 5.39 changes with time. The height of the drop at the first minimum is fixed, though, so the height of the plateau outside of the drop would seem to change over time. The magnitude of this error is in the 10% range as can be calculated from the values shown in Fig. 5.16.

A better approximation of the virtual maximum therefore is to take the absolute maximum $I_{max,\,abs}$ as described above and rescale it for every intensity plot of a time series in such a way that the height of the plateau (corresponding to a fixed intensity value) stays constant.

In all height profile reconstructions done in this thesis the first intensity plot of a time series is calculated with $I_{max,\,abs}$ and a starting value of $h_{plateau} = h(0) = 0\,\mathrm{nm}$ for the intensity $I(0) = I_{plateau}$. For all following height reconstructions the height at the first minimum will stay the same and the height for $I_{plateau}$ will always stay $h_{plateau} = 0\,\mathrm{nm}$.

[3]In most cases this value was that of the first maximum, however in some cases the absolute maximum was found to be another maximum or occurred in the plateau region.

The Middle Extremum

The intensity of a RICM micrograph at the drop's apex always shows an extremum I_{middle}. This is due to the fact that the intensity is a cosine transformation of the height. If the drop's apex has a height of $h \neq N \cdot \Delta h$ there will always be a region around the apex where the cosine will be strictly monotonic. So the cosine transformation of the spherical cap in this region will show an extremum I_{middle}. This extremum I_{middle} doesn't reach the full maximal or minimal value of intensity I_{max} or I_{min} corresponding to $h = N \cdot \Delta h$. This can also be seen in Fig. 5.14(b).

Only if the height h of the drop is $h = N \cdot \Delta h$ will the intensity at the apex of the drop reach a true extremal value I_{max} or I_{min} which is needed for the height calculation. In all other cases the value I_{max} or I_{min} needed for the height reconstruction of the apex region has to be estimated.

As the height of the drop's apex I_{middle} decreases with time the intensity at the apex will oscillate between minimal and maximal values I_{min} or I_{max}. An example is shown in Fig. 5.17.

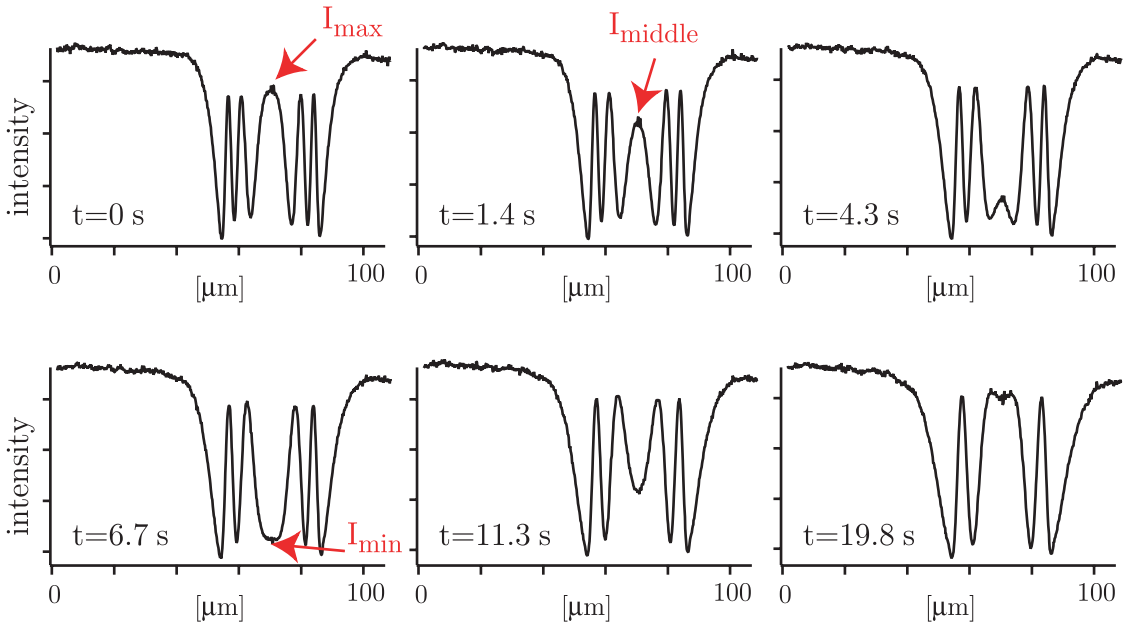

Figure 5.17: Time series of RICM intensity profiles of an evolving drop. The intensity I_{middle} of the middle extremum oscillates between I_{min} or I_{max}.

Therefore the extremal value I_{max} needed for the calculation of the drop profile at time $t = 1.4\,\mathrm{s}$ or $t = 4.3\,\mathrm{s}$ is not the value I_{middle} at those times but the value $I_{max}(t = 0)$. Along these lines the extremal value I_{min} needed for the calculation of the drop profile at time $t = 11.3\,\mathrm{s}$ or $t = 19.8\,\mathrm{s}$ is best estimated at the value $I_{min}(t = 6.7\,\mathrm{s})$. Accordingly, the height profiles of a series of intensity plots were calculated from the intensity profiles using the latest value of I_{max} or I_{min} of the preceding plots.

The intensity of all extrema, however, depends on the drop shape. As time evolves

the drop becomes smaller and the visibility in the drop center will increase. Therefore the consecutive inner maxima I_{max} will increase, whereas the inner minima I_{min} will decrease with time. Experimentally the difference between two consecutive minima or maxima is always less than 10%. The error due to this shift should be less than 5% as the first minimum or maximum is only used for the calculations in the first half of the cycle. This is equivalent to a possible error of less than $\Delta h \cdot 0.05 = 97.3\,\mathrm{nm} \cdot 0.05 = 5\,\mathrm{nm}$.

5.5.3 Calculation of Non-Local Correction Factors for the Used Setup

As described in Chapter 5.4.2 the non-local theory can be easily implemented by calculating an angle-dependant correction factor k. The local angle $\alpha_{non-local}$ of the reflecting interface at a point according to the non-local theory can be calculated as $\alpha_{non-local} = {}^1\!/_k \cdot \alpha_{simple}$, where α_{simple} is the angle determined by simple theory.

The correction factor for the reconstruction of drop profiles was calculated according to the non-local theory for several INAs in a collaboration by Felix Linke [Linke, 2004].

The interference pattern of a cone of light incident with a maximal angle equivalent to the INA reflected at an interface geometry was simulated by ray-tracing in analogy to [Wiegand et al., 1998], but with a number of improvements: here the concept of polarization raytracing was used [Conrady, 1957; Waluschka, 1989] while taking into account both incident and numerical aperture. The incident beam was taken as circularly polarized and the integration was done over the incident beam. The reflecting interface was assumed to be a wedge of PDMS with zero curvature on a thin film of cross-linked PDMS on glass in ambient water. The result of the simulation can be seen in Fig. 5.18.

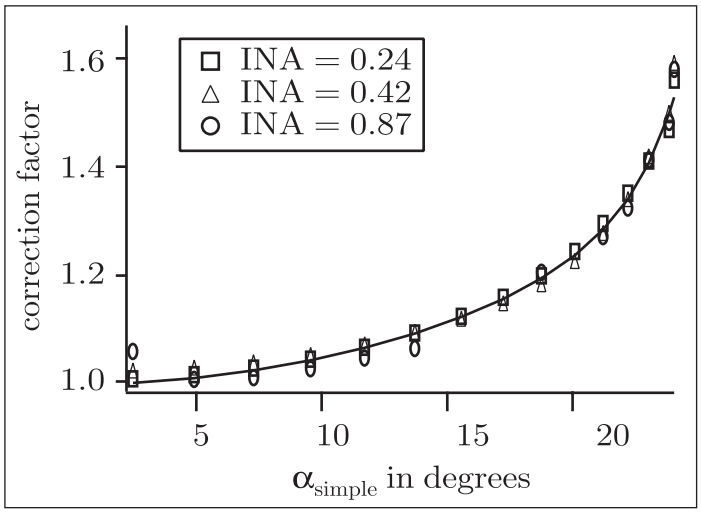

Figure 5.18: Non-local theory correction factors for the height profile reconstruction. The drop shape is modelled as a simple wedge with zero curvature. The correction factor is strongly dependent on the wedge angle but only weakly dependent on the illumination aperture. The continuous line represents a function which was used to determine the correction factor in calculations.

The correction factor depends strongly on the angle but only weakly on the INA. The relative difference between the values of the correction factor for the different

INAs is surprisingly low at less than 2%. Therefore all height profiles were calculated with correction factors only dependent on the angle and independent of the INA.

The following function was fitted to the simulated correction factor:

$$k(\alpha_{simple}) = \left(1 + A \cdot (B - \alpha_{simple})^C\right)\left(1 + D \cdot 10^{-4} \cdot \alpha_{simple}^2\right)$$

with the angle in degrees. The best fit to the simulated data is

$$k(\alpha_{simple}) = \left(1 + 16.13\,(29.58 - \alpha_{simple})^{2.48}\right)\left(1 + 4.24 \cdot 10^{-4} \cdot \alpha_{simple}^2\right) \qquad (5.40)$$

which is shown as a continuous line in Fig. 5.18. This function (Eq. 5.40) was afterwards used to determine the correction factor in the height profile calculations. As the function fits the data extremely well the error is clearly dominated by the 2% spread mentioned above.

For the calculation of the corrected height profile, the angle $\alpha_{simple}(x)$ was determined at every pixel x by a straight line fit within a surrounding interval of 1 µm of the height obtained by simple theory. Afterwards the angle $\alpha_{non-local}(x)$ was calculated according to equations 5.37 and 5.40 and the difference of the slope $\Delta s(x) = \tan\alpha_{non-local} - \tan\alpha_{simple}$ was determined. Starting from low values of x the new height was calculated stepwise by incrementally adding $\Delta h = \Delta s \cdot \Delta x$ to the height as determined by the simple theory. Here $\Delta x = 0.159$ µm is the distance between two neighbouring pixels.

All data show angles of less than 14°. This means that the correction factor is less than 1.1 in all cases. The difference in the calculated height of the drop's apex between simple theory and non-local reconstruction is less than 7% (example given in Fig. 5.19). This small value indicates that the used approximation is sufficient as further corrections would be of lower order.

In this approach, the geometry of the reflecting interface is modelled as a wedge with zero curvature. This is a simplification, as a drop is a spherical cap with a constant non-zero curvature. If the curvature is small enough though, the slope of the drop will barely change within the surface patch from which light is reflected to interfere afterwards at one point (illumination patch, see Section 5.4.1, Fig. 5.8).

To answer the question whether we can disregard the drops' curvature, we have to have a closer look at the drops in question. Here the observed drops are spherical caps with a radius of curvature in the order of 10^2 µm. Their height to width ratio is in the order of percent. Analysis of drop profiles from RICM reconstruction show that apart from the rim region the curvature changes by less than 0.5% per µm (example depicted in Fig. 5.20). This is the order of magnitude of the change in slope which will occur within the illumination patch. This curvature is sufficiently small to justify the calculation of the correction factor under the assumption of zero curvature.

The only part of the drop where the curvature will be considerable is the rim region. This does not have much influence on the height correction, however, as the angles concerned are still small and accordingly the correction factor is almost $k = 1$.

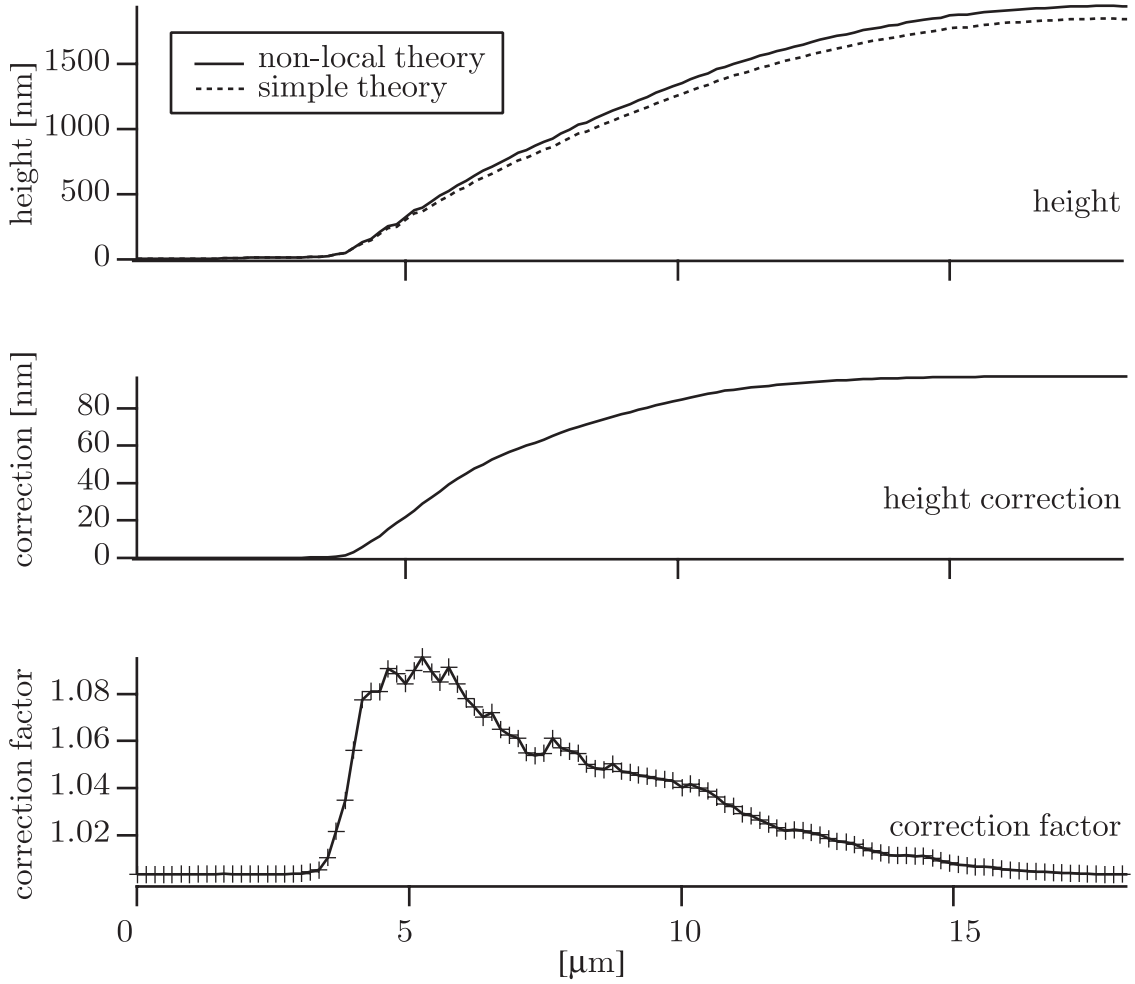

Figure 5.19: Non-local theory height correction of a drop profile. A drop with a contact angle of 14° is shown as an example with a large correction factor. This is one of the largest angles measured.

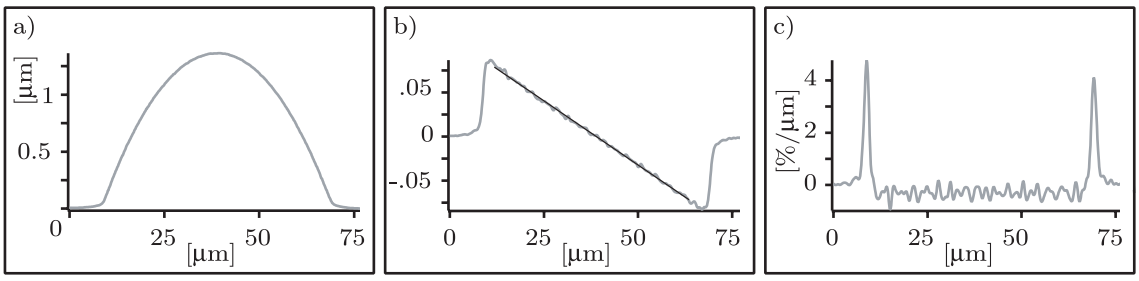

Figure 5.20: a) Height profile of an example drop.
b) The gradient of the height profile shows a slight linear decrease in the region where the drop can be represented by a spherical cap. The fitted line has a slope of -0.003 per µm, which is the average curvature and corresponds to a radius of curvature of 300 µm
c) The second derivative yields a curvature which is very small apart from the rim region.

Especially because the rim region is only a few µm wide the added height will be negligible.

Usually the drop will curve down continually towards the flat substrate[4] with a change in curvature in the order of % per µm at the rim region, which is still a rather small value. There are also cases, however, where the drop reaches the substrate forming a sharp edge. In these cases the reconstruction of the rim region will fail. This problem is also treated in Chapter 5.5.5.

5.5.4 Error Analysis

What can we tell about the quality of the reconstruction? What possible sources or errors are there and how big is their influence on the height determination?

Non-axisymmetry of the Drop

Only if the drop is axisymmetric, a height profile through the center of the drop will represent its whole three-dimensional shape. If the drop base is not spherical but suffers from distortions, any single height profile cannot represent the whole shape of the drop. Therefore the drop base radius calculated from a single height profile will merely represent the specific radius for this specific profile. Any calculation regarding the drop volume will suffer from these errors. Also the contact angle might exhibit different values if the drop is not axisymmetric [McHale et al., 2001].

It is assumed in all calculations, however, that the drop is completely spherical. As this is only an approximation, it is essential to quantify the error made by neglecting aspherical distortions of the drop. Therefore it is necessary to first quantify the non-axisymmetric deviation of the measured drops from a spherical cap. To do this, it is assumed that the shape of the drop is ellipsoid rather than spherical as a first order approximation.

The semi-major axis a and the semi-minor axis b are measured by fitting an outer and an inner circle to the outmost fringe line of the drop as seen in the RICM image (see Fig. 5.21).

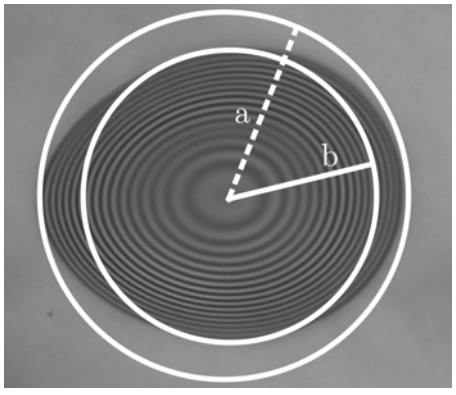

Figure 5.21: The semi-major axis a and the semi-minor axis b of an ellipsoidal drop are determined by fitting an outer and an inner circle to the rim line.

[4] the *foot* of the drop

Then the ratio a/b is determined for $t = 0\,\mathrm{s}$ and $t = 60\,\mathrm{s}$ (see Fig. 5.22 and Appendix E Tables E.3 and E.4). This ratio can be used as an estimate of the error of the drop base radius. As this ratio is also the coefficient by which the area of a circle differs from that of an ellipse, it can be used as a first estimate of the error of the drop volume if one neglects second order effects in the deviation of the height from a spherical cap. A simple calculation comparing the volume of a spherical cap to that of an ellipsoidal cap supports this.

As can be seen in Fig. 5.22 all drops can be regarded as mainly spherical. Moreover, any distortion from the spherical shape will decrease significantly within short times (see plotted values for $t = 0\,\mathrm{s}$ and $t = 60\,\mathrm{s}$), the average error after 60 s being in the range of 2%.

Therefore it is a valid approximation to treat all drops as axisymmetric.

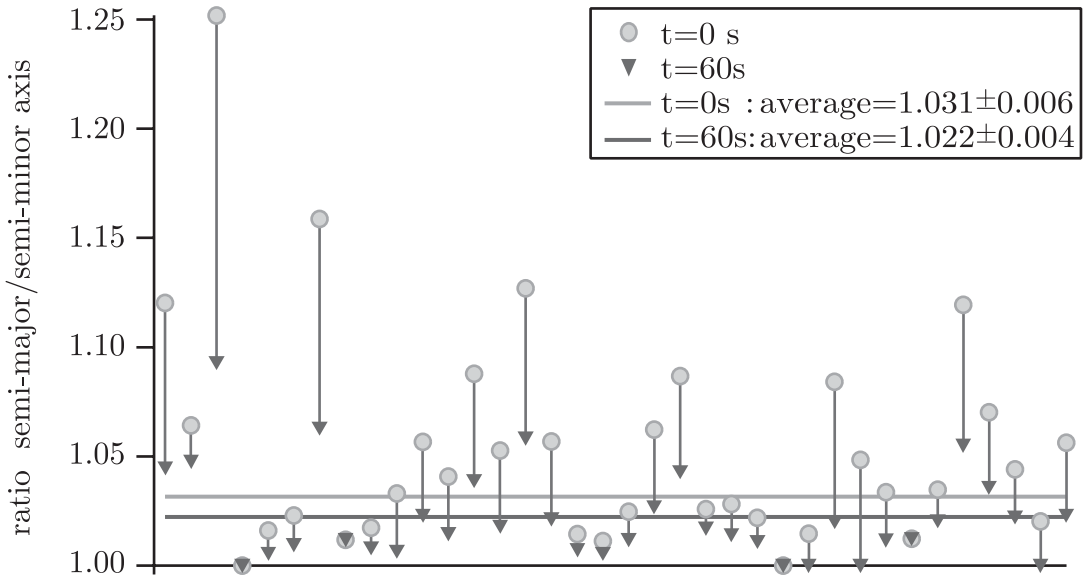

Figure 5.22: The ratio a/b of semi-major axis a to semi-minor axis b is plotted at two different times for all experiments. As can be seen, this ratio deviates only slightly from one, therefore all drops can be regarded as mainly spherical. Moreover, any distortion from the spherical shape will decrease significantly within short times (see plotted values for $t = 0\,\mathrm{s}$ and $t = 60\,\mathrm{s}$).

Inhomogeneous Illumination

A homogeneous illumination is crucial for reliable RIC microscopy as reconstruction of lateral intensity fluctuations will result in fluctuations in height regardless of whether they derive from the surface geometry or just from inhomogeneous illumination.

Creating a mostly homogeneous illumination is easy to facilitate, especially if the region of measurement is small compared to the maximal illuminated area of the microscope. The illumination, however, will always have an inhomogeneous part

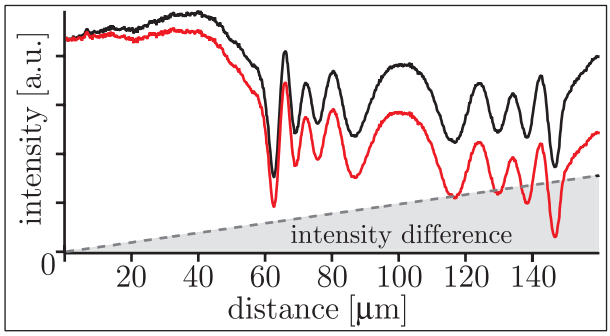

Figure 5.23: The intensity plot of a usual RICM image of a drop of PDMS on a flat substrate (black curve) was shifted by a linear intensity rise (dotted line) to give a heavily tilted plot (grey line) thus mimicking a highly inhomogeneous illumination. The illumination used in the experiments was less inhomogeneous in all cases.

especially when dealing with objects that extend over ranges of hundreds of µm as in the case of a drop with a suspected precursor.

The influence of the illumination on the reconstruction of a drop profile itself is small. The inhomogeneous part of the illumination can always be approximated by a linear rise between two adjacent extrema as the intensity of even a badly adjusted illumination varies only slowly between two extrema. This means that the intensity in between those two extrema differs from the homogeneous case only by a constant factor and offset. For situations with a small inhomogeneous contribution like in the presented experiments, this does not generate an observable lateral displacement of the extrema. As the reconstruction by an inverse cosine transformation demands the normalisation of the intensity in between two adjacent extrema anyway, the height reconstruction will barely differ from that of a homogeneous illumination.

This is demonstrated in Fig. 5.23 where a usual intensity plot of a drop of fluid PDMS on a flat substrate of cross-linked PDMS was shifted by an arbitrary linear intensity rise thus mimicking a highly inhomogeneous illumination.

As can be seen in Fig. 5.24(a) the difference in reconstructed height of the two plots is tiny. Inside the drop the difference is less than 4 nm or 0.5% (see Fig. 5.24(b)). As the used setup provides an illumination that is less inhomogeneous than the previously assumed one, the error of drop shape reconstruction due to inhomogeneous illumination can be neglected.

Inhomogeneous illumination has a more pronounced influence on the reconstruction of the flat substrate and the precursor region around the drop. This can be seen in Fig. 5.24(c) where the precursor region of the reconstruction of the two intensity profiles from Fig. 5.23 is shown. The difference between the two height profiles is in the range of 0–10 nm.

To monitor *changes* in the precursor region, the height profile of the substrate prior to drop deposition is subtracted. This allows easy recognition of height changes. Additionally, these height changes do not depend on the homogeneity of the illumination as strongly as the height itself. Fig. 5.24(d) shows the same region as Fig. 5.24(c) with subtracted background. The relative height difference is not affected by the inhomogeneous illumination as much as the original plots. The height difference is less than 5 nm. As any real illumination will be much less inhomogeneous than the assumed one, the impact of inhomogeneous illumination on the observation of height changes in the precursor region is very low and will be far less than 5 nm.

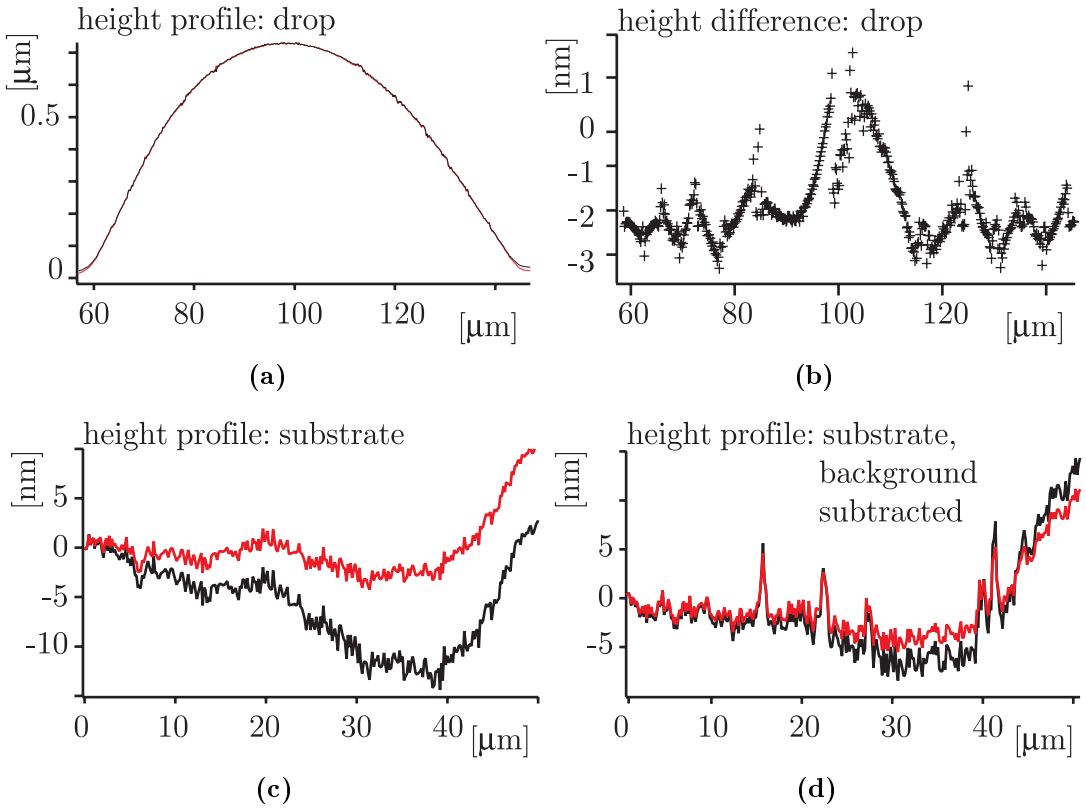

Figure 5.24:
a) Reconstruction of intensity profiles from Fig. 5.23 with and without additional lateral intensity rise (black line and grey line, respectively) using the same algorithm. The difference is hardly visible.
b) The difference between the two height profiles is less than 4 nm which is less than 0.5%.
c) Reconstruction of the substrate outside the drop shows a bigger influence of the illumination.
d) A respective background height profile of the substrate prior to drop deposition is subtracted from the height profiles from (c). The influence of the illumination decreases.

Time-Dependent Fluctuations

The RICM intensity of a fixed point will always exhibit time-dependent fluctuations. This noise can have several reasons such as instability of the lamp's light arc, fluctuation of fluids, movement of the whole setup against the microscope and thermal noise of the camera. How much influence will these fluctuations have on the reconstructed height?

In a simple experiment a drop of PDMS was put onto a substrate and then left for some time until the speed of drop motion had substantially decreased. A series of 10 pictures was then taken in succession within the next 7 minutes so that the drop motion between the first and the last picture was marginal. Height profile reconstruction was carried out and the standard deviation was calculated for each point of the curve.

The average standard deviation of the height was 1.8 nm.

A closer look at the standard deviation within the drop region reveals a defined structure: the standard deviation has peaks at the extrema of the intensity as shown in Fig. 5.25.

This is due to error propagation. Considering Eq. 5.39

$$\begin{aligned} h(x) &= \frac{\lambda}{4\pi n_{\mathrm{PDMS}}} \arccos \frac{2I(x) - (I_{max} + I_{min})}{I_{max} - I_{min}} \\ &= A \cdot \arccos \frac{2I(x) - (I_{max} + I_{min})}{I_{max} - I_{min}} \end{aligned}$$

the error of the height relates to the error of the intensity measurement as follows:

$$\Delta h(x)^2 = \left(\frac{\partial h}{\partial I(x)} \cdot \Delta I(x)\right)^2 + \left(\frac{\partial h}{\partial I_{max}} \cdot \Delta I_{max}\right)^2 + \left(\frac{\partial h}{\partial I_{min}} \cdot \Delta I_{min}\right)^2 \tag{5.41}$$

$$\begin{aligned} = {} & (\Delta I(x))^2 \; A^2 \frac{4}{\left(1 - \frac{(2\,I(x) - I_{max} - I_{min})^2}{(I_{max} - I_{min})^2}\right)(I_{max} - I_{min})^2} \; + \\ & (\Delta I_{min})^2 \; A^2 \frac{\left(-\frac{2\,I(x) - I_{max} - I_{min}}{(I_{max} - I_{min})^2} + \frac{1}{I_{max} - I_{min}}\right)^2}{1 - \frac{(2\,I(x) - I_{max} - I_{min})^2}{(I_{max} - I_{min})^2}} \; + \\ & (\Delta I_{max})^2 \; A^2 \frac{\left(\frac{2\,I(x) - I_{max} - I_{min}}{(I_{max} - I_{min})^2} + \frac{1}{I_{max} - I_{min}}\right)^2}{1 - \frac{(2\,I(x) - I_{max} - I_{min})^2}{(I_{max} - I_{min})^2}} \end{aligned} \tag{5.42}$$

Here $\Delta h(x)$ is equivalent to the standard deviation σ_h. $\Delta I(x)$ is the error of determining the intensity I at point x, ΔI_{min} and ΔI_{max} are the errors of determining the intensity at the respective extrema. Apart from time -dependent fluctuations the error when determining the extrema is also be due to the finite pixel width, as the extremum is smeared out between two pixels which will reduce the measured I_{min} or I_{max}.

The peaks of the standard deviation σ_h at the position of the extrema in intensity are due to the poles of the derivative of the arccos at the extrema.

The standard deviation of the height was calculated with Eq. 5.42 using a data-supported estimate of an average intensity error $\Delta I(x)$ of 0.5% of the background intensity and equivalent ΔI_{max} and ΔI_{min}. The resulting standard deviation is shown in Fig. 5.25. It is in good agreement with the standard deviation determined by comparing the height profiles of 10 independent measurements of the same drop. Therefore it is legitimate to use Eq. 5.42 with a simple estimate of the initial intensity fluctuations as a means for further error calculations.

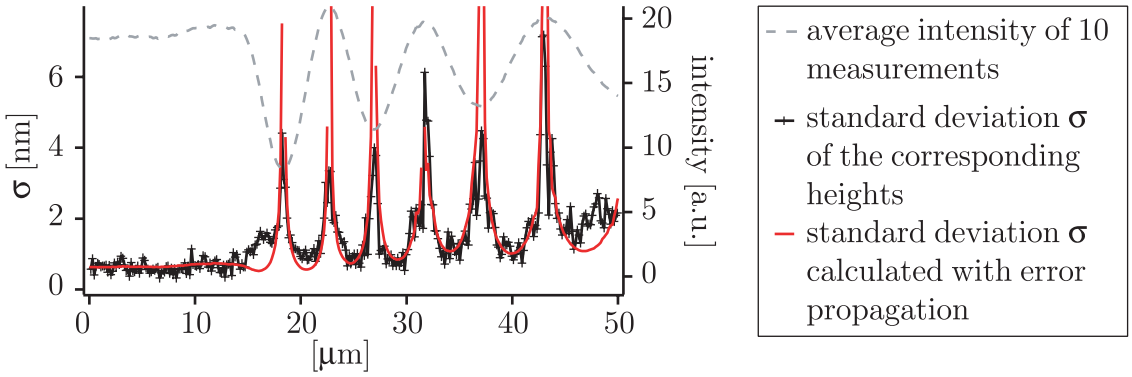

Figure 5.25: The standard deviation of the height was first determined from 10 height profiles of consecutive measurements of the same drop (black curve). The data is well described by a standard deviation calculated by means of error propagation and a simple estimate of the error in determining the intensity (grey line). The standard deviation shows peaks at the positions of the extrema of the intensity in both cases.

5.5.5 The Rim Caustic

The reconstruction of the rim region is problematic. If performed in the same straightforward manner as the plain substrate or the drop itself, the resulting height profile can be misleading if not utterly wrong. For geometries with a sharp bend between the spherical cap and the flat substrate the reflected intensity will change at the edge in a stepwise fashion. Integration over all incident angles and diffraction can lead to caustic phenomena[5] [Berry, 1976]. For drops with a slow bend towards the substrate, the so-called *foot*, this phenomenon does not occur as shown in Chapter 5.5.3.

[5]For a given curve and a given point source of light, the caustic of the curve is the envelope of rays of light reflected (or refracted) by the curve.

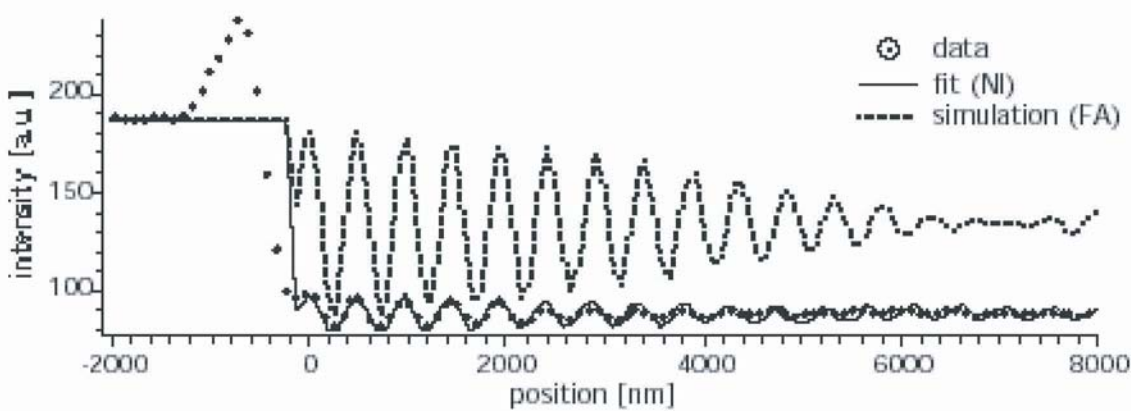

Figure 5.26: Intensity plot from a RICM interferogram of a water droplet on a glass substrate exposed to air. The measured data were fitted by the theory of non-planar interfaces (NI / drawn line) and the finite aperture theory (FA / dashed line), respectively. The rim caustic can be clearly seen as an intensity overshoot between the plateau of the background region and the sinusoidal intensity profile of the drop region. (from [Wiegand et al., 1998]).

In experiments the intensity profiles of drops with a sharp bend show an overshoot of intensity between the plateau of the background region and the sinusoidal intensity profile of the drop region (see Fig. 5.26). This occurs with and without additional contrast layer between drop and substrate.

This phenomenon has been seen before. Wiegand et al. [1997, 1998] noticed the overshoot, but their attention was on the reconstruction of the sinusoidal part of the profile so no further analysis of the rim region was carried out. Zhang and Chao [2003] describe a shadowgraphic experiment where the existence of a caustic is used to discriminate drops with a sharp bend towards the substrate from drops which exhibit a slow rise.

When applying the regular reconstruction algorithm to a RICM image with an overshoot due to the rim caustic, this will lead to a height profile with a plateau followed by a small trench in front of the sharp rise. It is important to know that this trench in the height profile is an artefact and does not convey information about the real height.

5.6 RICM Setup

The setup consists of an inverted AXIOVERT 200 (CARL ZEISS, Göttingen, Germany) microscope which is illuminated by a mercury arc lamp (HBO 103W/2, OSRAM, Munich, Germany). This lamp emits incoherent light in a line spectrum. For RIC microscopy the green line at 546 nm is selected by a filter (D 546/12 with S/R[6] coating, AHF ANALYSENTECHNIK AG, Tübingen, Germany). Following a path with Köhler optics the light is deflected at a semi-transparent (50%) mirror and reaches the substrate through an high aperture objective (63×/1.25 ANTIFLEX-NEOFLUAR OIL-IMMERSION, ZEISS, Germany) with built-in $\lambda/4$ plate. Light reflected at the different interfaces of the substrate interferes, passes the objective and a polarizer (DIC-Senarmont, ZEISS, Germany) and is recorded by a cooled, digital CCD camera (Orca ER, HAMAMATSU PHOTONICS, Germany), digitized by a frame-grabber card (STEMMER IMAGING, Germany), and processed with the imaging software OPEN BOX [Keller et al., 2001].Sketches of the working principle of a RICM microscope are also shown in Fig. 5.3 and Fig. 5.1.

The line profiles were taken from the raw data in OPEN BOX. Afterwards the data was stored in a compressed form. The height reconstruction was done with various specially written macros in the data processing programm IGOR PRO (WAVE METRICS, INC., Lake Oswego, USA).

[6]scratch-resistant

Chapter 6

Wetting and Diffusion

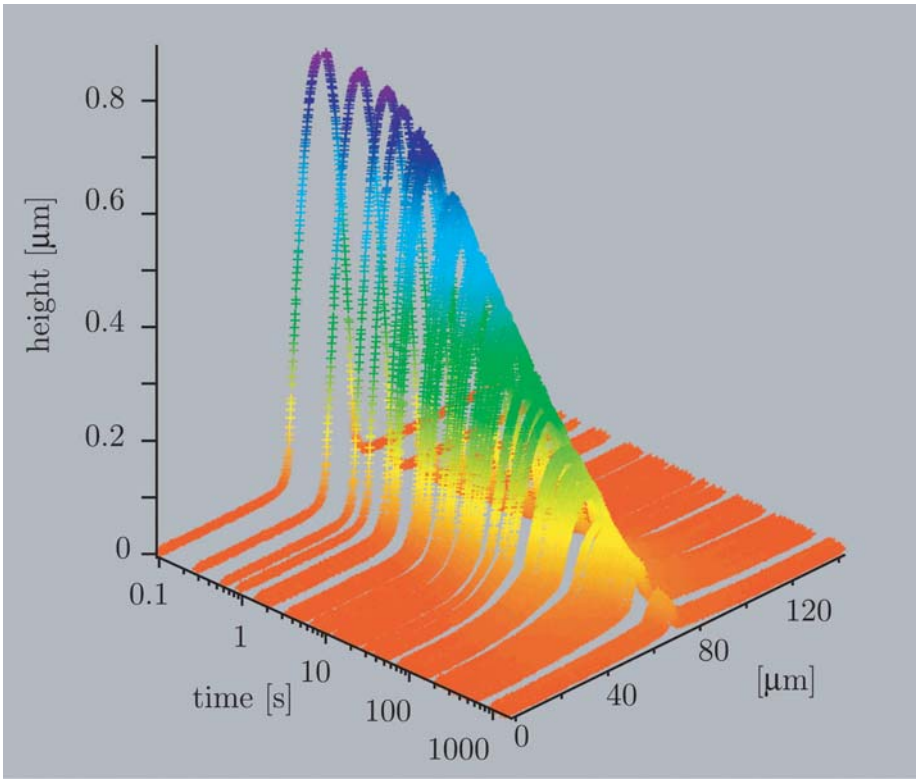

Figure 6.1: Development of the reconstructed height profile of a drop of fluid PDMS (DMS-T21) on a substrate of cross-linked PDMS. Notice the logarithmic scale of the time axis.

In this chapter the observations of the performed experiments will be presented and discussed. In all, over 40 drops of different PDMS oils on two different substrates were observed.

In Chapter 6.1 it will be shown that the general shape of drops of PDMS deposited on a film of cross-linked polymer is that of a spherical cap.

In Chapter 6.2 the behaviour of the drop base radius will be presented.

In Chapter 6.3 it will be shown that the drop loses volume continuously and that this loss is due to diffusion into the substrate. This diffusion process can be understood as a radially symmetric, two dimensional diffusion process in an infinitely thin disk. Evaluation of the governing equations with the semi-analytical method of Jeager agrees well with the data for short times where the variation of drop base radius can be neglected. It can be shown that it is possible to solve the diffusion equation numerically. The general form of the calculated volume loss is in good agreement with the measured data.

In Chapter 6.4 the behaviour of the contact angle will be presented. As the drop is deposited onto the substrate and evolves to reach its equilibrium shape, the contact angle decreases. This decrease follows a power-law behaviour. For long times the contact angle might increase again, a behaviour that has never been observed before. A simple model suggests this might be due to chain kinetics at the rim of the drop.

6.1 Drop Shape

The equilibrium shape of a static drop on a clean substrate is a spherical cap as this minimizes the free energy of the surface. In the case of a non-static wetting drop, this holds true except for the rim region where the drop will slope down continuously and forms the so-called *foot of the drop*.

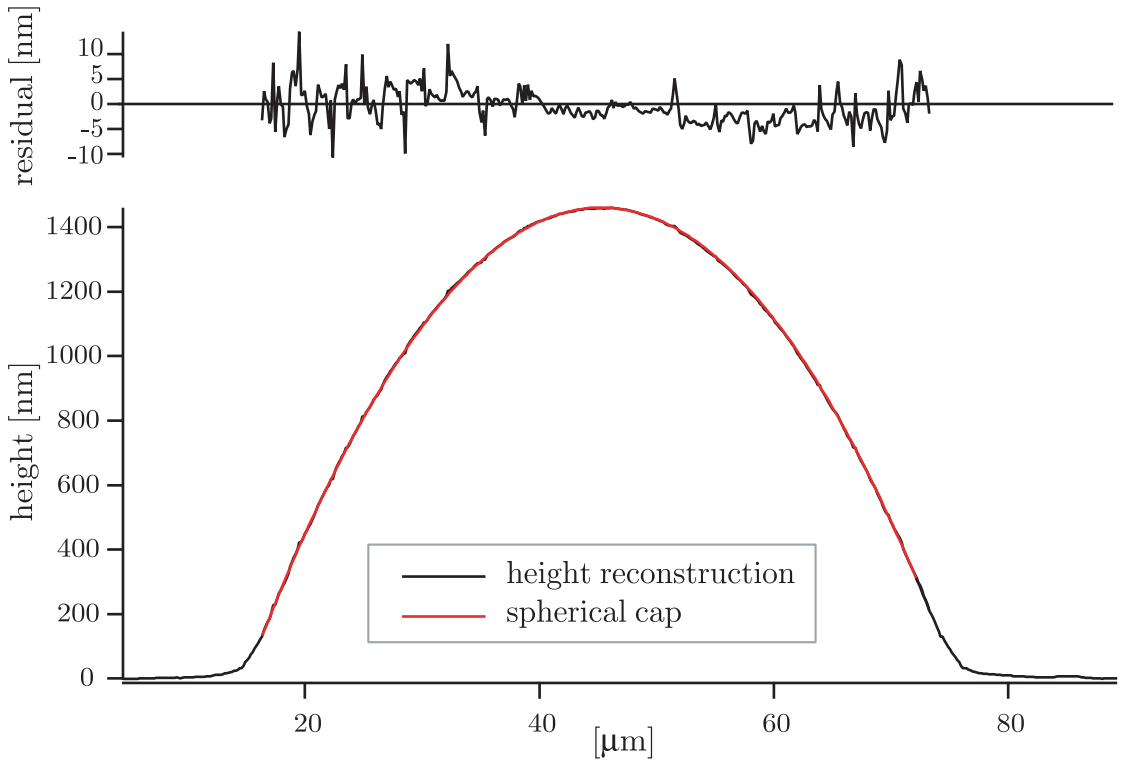

Figure 6.2: The shape of the inner part of the reconstructed drop is in very good agreement with a spherical cap. Shown here is a drop of fluid PDMS with a polar fraction only a few seconds after deposition. No distortion of the drop shape due to the removal of the micropipette can be seen.

Albrecht et al. [1992] report that this holds true even for small drops of polymer ($V \sim 6\,\mathrm{pl}$) with a central thickness equal to one monolayer. In this case the continuum picture is expected to break down and the polymer molecules should then behave like a two-dimensional freely diffusing surface gas and form a Gaussian distribution. However, it was found that the deposited drops still form spherical caps, which in the authors opinion is due to entanglement and hindered diffusion.

In this study experiments were performed with drops of even smaller volume but with considerable bigger initial heights. The initial volumes were in the range of $V = 75 - 8000\,\mathrm{fl}$ with initial drop base radii of 10-150 µm (see also Appendix E Tables E.3 and E.4). The height of the measured drops was in the range from 1-2 µm down to the order of 10 nm for very long times. The drop base radius for the latter drops was merely a few micrometer and the accuracy of those measurements was therefore limited by the lateral resolution.

The drop shape was determined by calculating the height profile of an intensity profile running through the center of the drop as described in Chapter 5.5. Then a spherical cap was fitted to the data in the following way: the two end points were selected manually. Afterwards the starting values of the fitting parameters were calculated using the height of the end points and the height of a middle point in between the two end points. The spherical cap was then fitted according to the equation:

$$y = f(x) = \sqrt{R^2 - (X_r - x)^2} + Y_r \tag{6.1}$$

where the fitting parameters are the radius square R^2, and the coordinates of the center of the drop X_r and Y_r.

Within one experiment the shape of the drop was tested accordingly up to 100 times by taking intensity profiles at different times and afterwards calculating the corresponding height profiles.

It was found that a drop of fluid PDMS assumes its spherical shape very shortly after it is deposited onto the substrate with the micropipette. The drop shape equilibrates within less than half a second as no distortion can be seen in profiles taken after that period. The drop stays spherical throughout the whole experiment. The deviation of the measured profile from a spherical cap fit is very small (see Fig. 6.2).

As the residuals within a single experiment resemble each other and the number of measurements in a single experiment varies highly, a meaningful mean residual was calculated in the following manner. First the root mean square of the residuals of all height profiles taken within one experiment was calculated. Then the mean of these values was calculated to 6.2±3.8 nm (a histogram of those values is shown in Fig. 6.3). This is roughly in the same order of magnitude as the measurement error of 1.8 nm due to time dependent fluctuations (see Section 5.5.4).

No possible shape distortion due to the volume loss by diffusion through the drop base can be distinguished. This is clearly due to the fact that the drop shape equilibrates very fast as the viscosity of the used fluid PDMS is low whereas the diffusion process is very slow (see Section 6.3).

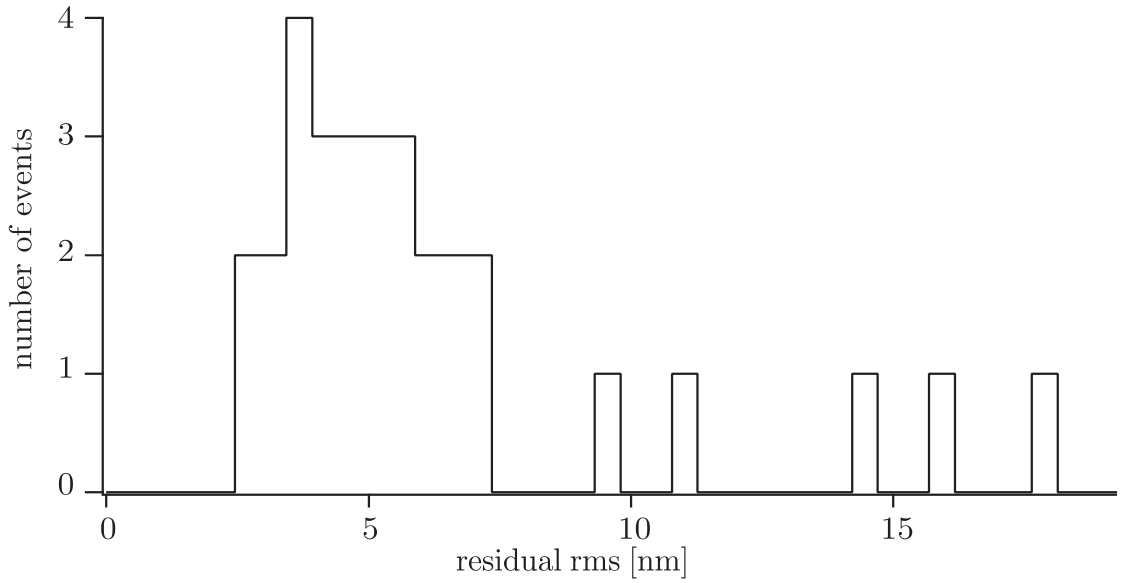

Figure 6.3: The root mean square residual of all taken height profiles from one single experiment was calculated. Then the mean of these values was determined to be $6.2 \pm 3.8\,\mathrm{nm}$. A histogram of the residuals is shown above ($n = 31$, bin width: $0.5\,\mathrm{nm}$).

6.2 Drop Base Radius

The drop base radius was determined as the position of intersection of the spherical cap fit with the x-axis as shown in Fig. 6.4. This is a reproducible method that will result in a point close to the position that one would intuitively assume to be the rim.

In all experiments the initial drop base radius was in the range of 5-50 μm. After deposition the drops first spread on the substrate to reach its equilibrium contact angle, but because the drop loses volume at the same time, the drop base radius shrinks again after a certain time t_r. A few typical examples are depicted in Fig. 6.5.

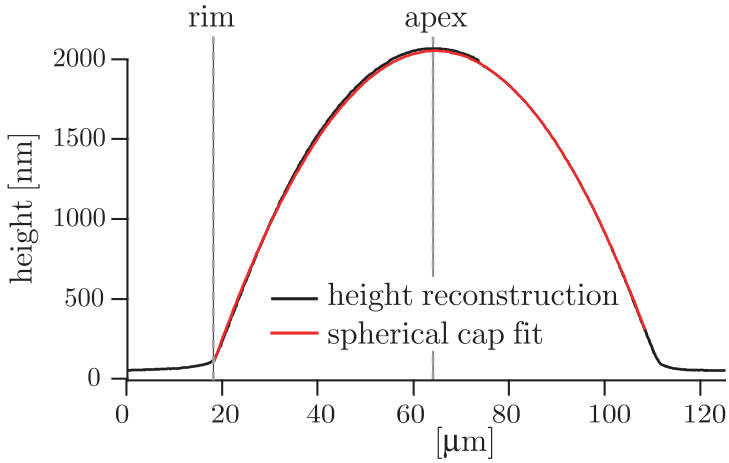

Figure 6.4: The position of the rim is determined as the point where a spherical cap fit crosses the x-axis. The inner and outer boundary for the integration procedure are also determined using the spherical cap fit.

The reversal of the velocity of the contact line can only be explained if the volume loss is taken into account. After deposition the drop will exhibit a non-equilibrium contact angle and thus will be forced to spread. However as its shape remains that of a spherical cap and the volume loss becomes more and more pronounced over time, the drop will start to shrink again at a certain time t_r. This also occurs in experiments where a fluid drop is deposited onto a porous substrate like a permeable membrane [Clarke et al., 2002; Denesuk et al., 1993; Starov et al., 2003; Zhdanov et al., 2003].

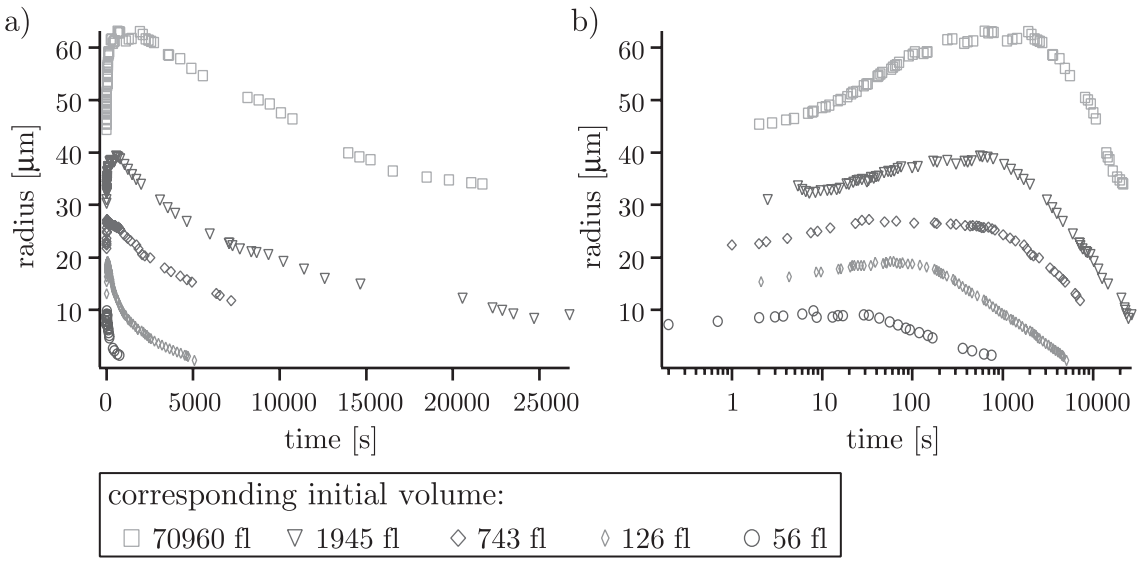

Figure 6.5: Examples of the evolution of the drop base radius of a drop of fluid PDMS on a substrate of cross-linked PDMS. Both graphs show the same set of measurements with the time axis being linear in the left graph and logarithmic in the right one. The reversal of the movement of the contact line is clearly visible. The fluid PDMS used in these experiments was DMS-T22 with a polar fraction. The viscosity was 200 cSt=200 mm^2/s.

6.3 Loss of Volume Due to Diffusion

As soon as a drop of fluid PDMS is deposited onto the substrate its volume starts decreasing. This is illustrated in Fig. 6.6 where the volume evolution of a set of several drops of PDMS is shown. The distinct feature of the volume loss is its fast onset and the subsequent slowing down as the volume decreases to zero. The slowing down of this process can be seen especially clearly using a logarithmic time axis (Fig. 6.6, right side).

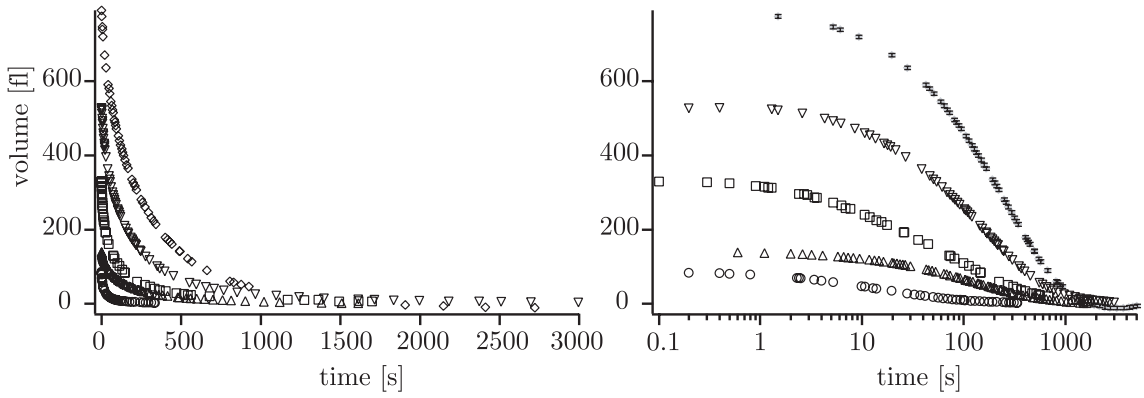

Figure 6.6: Examples of the evolution of the volume loss of a drop of fluid PDMS on a substrate of cross-linked PDMS for several measurements. Both graphs show the same set of measurements with the time axis being linear in the left graph and logarithmic in the right one. Exemplary error bars are shown for the largest drop in the right graph. The fluid PDMS used in these experiments was DMS-T21 with a viscosity of 100 cSt=100 mm^2/s.

6.3.1 Determination of the Drop Volume

The drop volume was determined from the reconstructed height by a trapezoidal integration using spherical symmetry:

$$V(t) \;=\; \sum_{i=0}^{n} \frac{1}{2}\left(h(x_{i+1}) + h(x_i)\right) \cdot \pi \left(x_{i+1}^2 - x_i^2\right) \tag{6.2}$$

where x_0 is the position of the apex, x_n is the position of the rim and $h(x)$ is the height at position x as reconstructed from the measured data.

The positions of the apex of the drop and the rim position are determined using a spherical cap fit. The apex is simply taken from the fit itself. However the boundary of the drop cannot be determined as precisely as the apex, as the height profile approaches the substrate at the rim of the drop in a smooth decline, which permits a precise determination of its position. To acquire reproducible data the outer limit of summation was taken as the point where the spherical cap fit meets the x-axis as shown in Fig. 6.4.

This procedure for determining the drop volume has two sources of error: the error of the height reconstruction and the error imposed by a drop that has a slightly

non-spherical boundary. The error of the height reconstruction is independent of the absolute height and in the order of a few nm. This implies that the error of the drop volume increases for decreasing drop size. Taking an average error of the height reconstruction of 5 nm, which is a reasonable upper boundary (see Section 5.5), the error of the volume of an example drop was calculated to be less than 5 fl (see error bars in Fig. 6.6).

6.3.2 Verification of Volume Loss by Diffusion: Continuous Bleaching Experiments

A drop of fluid PDMS on a substrate of cross-linked PDMS with water as the ambient medium can lose volume in several different ways. First the PDMS oil could simply dissolve into the water. As a second possibility the drop could spread on the substrate with a thin precursor film that would be too thin to be visible in this kind of experiment and could effectively induce the volume loss. The third possibility is a volume loss through diffusion of the fluid PDMS into the substrate. In this section it is shown that the third possibility is the main contributor.

The evaporation of the hydrophobic PDMS oil into the surrounding medium is highly unlikely because it is insoluble in water as mentioned in the manufacturer's manual. Nevertheless it was checked whether the volume loss could be due to evaporation into the surrounding water. This was done by performing an experiment in water already saturated with PDMS as this would slow down the volume loss if it was due to evaporation. The water was saturated with PDMS (DMS-T22) by mixing 1 ml of purified water with app. 0.1 ml of PDMS (DMS-T22) and gently stirring for two days. The experiment was then performed as usual. Within 200 s a drop of fluid PDMS lost about 60% of its initial volume of 7 pl. This value is not noticeably smaller than comparable values from other experiments (see Fig. 6.7). Therefore evaporation of PDMS into the surrounding water is not a major contribution to the total volume loss and can be neglected.

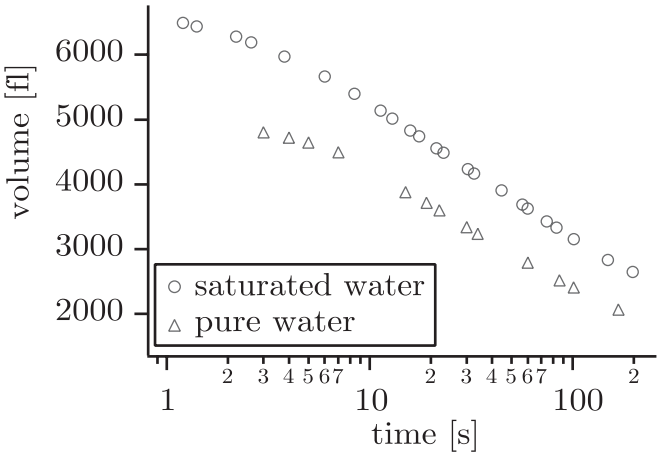

Figure 6.7: An experiment was performed in water saturated with PDMS. The volume loss does not differ from that of a comparable drop in pure water.

To distinguish between the flow of PDMS as a precursor film and the diffusion of PDMS in the substrate the diffusion coefficient was determined in a continuous bleaching experiment as described in Appendix D.

The expected diffusion coefficient for self-diffusion of fluorescently labelled PDMS within a matrix of free PDMS is in the order of $D_S = 30\,\mu m^2/s$ [Cosgrove et al., 1996], which is one order of magnitude higher than the diffusion coefficient expected for the diffusion of free PDMS chains in a cross-linked network of PDMS ($D_{NW} = 3.3\,\mu m^2/s$) [Garrido et al., 1988]. Therefore it is possible to distinguish between a situation with a precursor film on top of the substrate with a diffusion coefficient similar to that of self diffusion D_S and a situation where the PDMS diffuses solely within the substrate, which will result in a diffusion coefficient similar to that of $D_{NW} = 3.3\,\mu m^2/s$.

The self diffusion constant of the fluid PDMS was determined at $D_S = 39 \pm 9\,\mu m^2/s$, which is in good agreement with the expected value of app. $30\,\mu m^2/s$ as measured by Cosgrove et al. [1996]. This indicates that the performed measurements of the diffusion constant by continuous bleaching are reliable.

The diffusion constant of the labelled PDMS as measured at a distance of 50–$200\,\mu m$ to the respective drop was determined to be $D = 3.5 \pm 0.8\,\mu m^2/s$. This value matches the expected value D_{NW} for the diffusion of free PDMS chains in a cross-linked network. If a substantial contribution from a precursor film had been present, this would have led to a concentration profile with two discernible decay lengths. As this was not the case the main contribution to the loss of volume can be attributed to diffusion within the network of cross-linked PDMS.

As the diffusion coefficient was only measured for the PDMS with lower viscosity (DMS-T21) the diffusion coefficient for the used PDMS oil with higher viscosity has to be estimated. The reptation theory gives a dependency of the diffusion coefficient on the molecular weight M of the polymer of $D \propto M^{-2}$ [Masaro and Zhu, 1999]. However Garrido et al. [1988] performed measurements of fluid PDMS in cross-linked networks of PDMS and arrived at a proportionality of $D \propto M^{-1.3}$. Taking those values as the limiting boundary, the value for the diffusion constant for DMS-T22 can be estimated to be between $D = 1.3\,\mu m^2/s$ for $D \propto M^{-2}$ and $D = 1.8\,\mu m^2/s$ for $D \propto M^{-1.3}$. The value used for all further calculations was $D = 1.8\,\mu m^2/s$.

6.3.3 Comparison of the Data to the Semi-Analytical Solution of the Diffusion Equation

When the drop is put onto the substrate of cross-linked PDMS, the liquid PDMS starts to diffuse into the substrate. The drop is spherical, therefore this process can be treated as an axial-symmetric diffusion, which is most efficiently described in cylindrical coordinates.

As described in detail in Section 3.2.3 the average time a PDMS molecule needs to cover the distance $\Delta = 200\,nm$ between upper and lower surface of the cross-linked film is in the range of milliseconds. This is very short compared to the time the same molecule needs to travel distances in the μm range away from the drop. Therefore it is reasonable to assume that the thin film of cross-linked polymer is always saturated with liquid PDMS in the region directly underneath the drop as the outward motion

is the bottleneck of the diffusion process.

Assuming a constant concentration c_0 underneath a drop of a liquid with diffusion coefficient D and constant radius R the diffusion equation can then be treated as described in Section 3.2.3. The resulting concentration flux out of the drop is:

$$\Phi(t) = \frac{8D\,c_0}{\pi} I(0,1,\alpha) \qquad \text{(Eq. 3.41)}$$

where $\alpha = Dt/R^2$ and $I(0,1,\alpha)$ is a function that has been evaluated by Jaeger and Clarke [1942]. The flux of volume is therefore

$$\Phi_{vol}(t) = \frac{8D\,\nu_{max}\,\Delta}{\pi} I(0,1,\alpha) \tag{6.3}$$

where ν_{max} is the maximal volume ratio of liquid PDMS in the network and Δ is the thickness of the cross-linked film. For a comparable setup of fluid PDMS in a cross-linked network of PDMS this quantity has been measured to be around $\nu_{max} = 0.4$ [Pouchelon et al., 2001].

The volume can then be calculated as

$$V(t) = V_0 - \int_0^t \Phi_{vol}(\tau)d\tau \tag{6.4}$$

$$= V_0 - \int_0^t \frac{8D\,\nu_{max}\,\Delta}{\pi} I(0,1,\alpha(\tau)d\tau \tag{6.5}$$

where V_0 is the maximal volume of the drop after its deposition.

The behaviour of the measured data was compared to this theory using a specially written IGOR macro. In this procedure the values for $I(0,1,\alpha)$ are either linearly interpolated from the table in Jaeger and Clarke [1942] or calculated using the approximations Eq. 3.43 for $\alpha \leq 0.01$ and Eq. 3.44 for $\alpha \geq 1000$.

The volume is calculated using Eq. 6.5. The integral is evaluated using a trapezoidal integration procedure with 10000 time steps at coordinates evenly spaced on a logarithmic scale. The logarithmic spacing of the time steps is sensible as the dynamics are very fast at the beginning of the experiment and then slow down considerably. The maximal volume V_0 is taken as the average of the first three measured values to account for the slight scatter in the data[1].

Two examples of the volume data of a drop of fluid PDMS on a substrate of cross-linked PDMS are depicted in Fig. 6.8 with the volume calculated as described above.

This semi-analytical solution of the diffusion equation fits all data well within the first two decades of time. This is especially remarkable as the theory does not include any adjustable parameters except the initial volume. The agreement of this theory to the data is another clear sign that the drop loses volume by diffusion.

The theory can be made to match the data even more closely if one allows for an adjustment of the volume factor v_{max} of between $v_{max} = 0.35 - 0.55$.

[1] Average standard deviation of the mean of the first three data points is less than 3%.

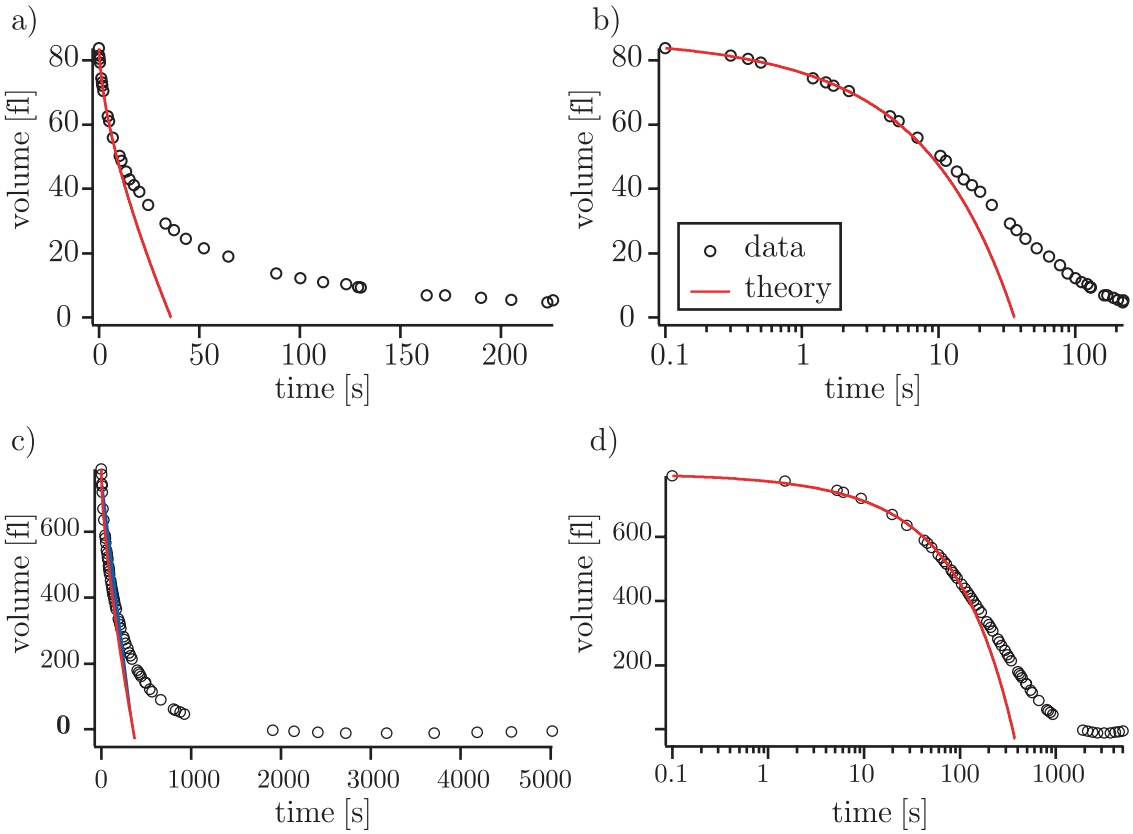

Figure 6.8: Volume evolution of two drops ((a)–(b), (c)–(d)) of fluid PDMS (DMS-T21) on a thin film of cross-linked PDMS. The theory reproduces the volume loss very well for short times. This can be seen especially clearly in the logarithmic plots on the right side. The value used for the diffusion coefficient was $D = 3.5\,\mu m^2/s$ and the maximal volume fraction of fluid PDMS in the matrix was taken as $\nu_{max} = 0.4$ (a) and $\nu_{max} = 0.55$ (b).

However there seems to be a volume dependency of the process for PDMS with a polar fraction. Bigger drops lose volume faster than expected by the theory whereas small drops lose volume slower than expected. This can be seen clearly in the series of measurements that were done with PDMS DMS-T22 with a polar fraction (see Fig. 6.9). For this series the spread in volume V_{max} is very high with the start volume ranging between $V_{max} = 40 - 12000\,fl$.

6.3.4 Comparison of the Data to a Numerical Solution of the Diffusion Equation

Finite Difference Scheme for the Diffusion Equation

The simple model of Jaeger led to a good agreement between data and theory for short times but for longer times this approach fails inevitably as the receding contact line cannot be taken into account. Therefore a simulation of the diffusion process

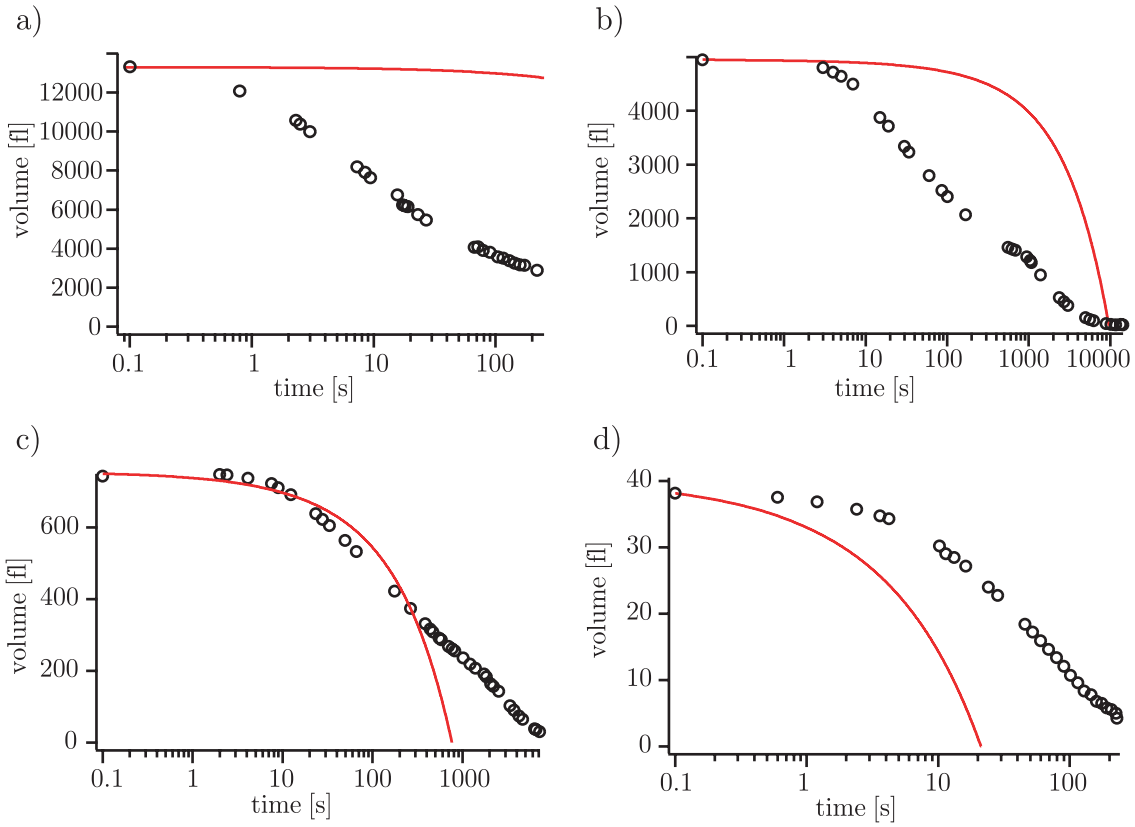

Figure 6.9: Four examples of the volume loss of a drop of fluid PDMS with a polar fraction on a thin film of cross-linked PDMS. The values used for the calculation were taken as $D = 3.5\,\mu m^2/s$ for the diffusion coefficient and $\nu_{max} = 0.4$ for the maximal volume fraction of fluid PDMS in the matrix. The velocity of the volume loss seems to decrease with decreasing start volume.

was done using the finite-difference form of the basic diffusion equation

$$\frac{\partial c(\mathbf{r},t)}{\partial t} = D\,\Delta c(\mathbf{r},t) \qquad \text{Fick's } 2^{nd} \text{ law.}$$

in cylindrical coordinates

$$\frac{\partial c(r,t)}{\partial t} = D\left(\frac{\partial^2 c}{\partial r^2} + \frac{1}{r}\frac{\partial c}{\partial r}\right)$$

and using the measured drop base radius as a boundary condition.

In general differential equations can be solved either by *explicit* or by *implicit* methods. *Explicit* methods are rather straightforward: each value $c(r_i, t_{n+1}) = c_i^{n+1}$ at a time t_{n+1} is evaluated from the nearby values at the time t_n. The explicit algorithm for the axis-symmetric diffusion equation in cylindrical coordinates is:

$$\frac{c_i^{n+1}}{\Delta t} = \frac{c_i^n}{\Delta t} + D\left(\frac{c_{i+1}^n - 2\,c_i^n + c_{i-1}^n}{(\Delta r)^2} + \frac{c_i^n - c_{i-1}^n}{\Delta r\; r_i}\right) \tag{6.6}$$

In accordance to the boundary conditions the first derivative in space is taken from the left to the right (*upwind differencing*), thereby describing a flow from left to right.

The diffusion equation is an example of a *stiff* differential equation where the solution involves several different time-scales which vary by orders of magnitude. This implies that the time steps have to be very small, too small for the explicit solution to be efficient. If the time step chosen is too large however, the solution will suffer from exponentially growing high-frequency oscillations [LeVeque et al., 1998]. Therefore the diffusion equation has to be solved using an *implicit* method as this method does not suffer from these problems.

Implicit methods are also called *backward time* as the derivatives on the right hand side are evaluated at time steps t_{n+1}. These methods are not prone to instabilities due to high frequency oscillations. Their drawback is that they are only first-order accurate in time. The *fully implicit* finite difference equation for the axis-symmetric diffusion equation is:

$$\frac{c_i^{n+1}}{\Delta t} = \frac{c_i^n}{\Delta t} + D \left(\frac{c_{i+1}^{n+1} - 2\,c_i^{n+1} + c_{i-1}^{n+1}}{(\Delta r)^2} + \frac{c_i^{n+1} - c_{i-1}^{n+1}}{\Delta r\; r_i} \right) \tag{6.7}$$

To generate a higher order accuracy the explicit-implicit *Crank-Nicolson* scheme was used, which is second-order accurate [Press et al., 1992]. In this method the average of the right-hand side of equations Eq. 6.6(*fully implicit*) and Eq. 6.7 (*explicit*) is evaluated:

$$\begin{aligned} \frac{c_i^{n+1}}{\Delta t} = \frac{c_i^n}{\Delta t} + \frac{D}{2} \Bigg(& \frac{c_{i+1}^{n+1} - 2\,c_i^{n+1} + c_{i-1}^{n+1}}{(\Delta r)^2} + \frac{c_{i+1}^{n+1} - c_{i-1}^{n+1}}{\Delta r\; r_i} \\ & + \frac{c_{i+1}^{n} - 2\,c_i^{n} + c_{i-1}^{n}}{(\Delta r)^2} + \frac{c_{i+1}^{n} - c_{i-1}^{n}}{\Delta r\; r_i} \Bigg) \end{aligned} \tag{6.8}$$

Here the centered first derivative is used. This is necessary because the concentration profile along the radius is not calculated from one point r_i to the next r_{i+1} as is the case for the explicit method, but instead the concentration at a point $c(r_i, t_{n+1}) = c_i^{n+1}$ depends on the whole concentration profile at the time t_n. The whole concentration profile is calculated at the same time by solving the set of linear equations generated by Eq. 6.9.

As the evolution of the diffusion process begins very fast and then slows down considerably, the time steps were not equally spaced, but were taken with a logarithmical spacing. The same holds for the concentration variation in space which changes considerably near the rim of the drop, but is quite flat in the distance. Therefore the used radius steps had a logarithmical spacing as well. This is not unusual in diffusion simulations, for example, most heat transfer problems in astrophysics are treated with grid steps of varying size (see [Olshanskii and Reusken, 2004] for further references).

As the grid width varies, the time steps $\Delta t^n = t^n - t^{n-1}$ and radius steps $\Delta r_i = r_i - r_{i-1}$ have to be considered at their appropriate positions. The whole set of linear equations in matrix representation will therefore look like:

$$\begin{pmatrix} \cdot & & & & & & \\ & \cdot & & & & & \\ & & \cdot & & & & \\ & & A_i & B_i & C_i & & \\ & & & & \cdot & & \\ & & & & & \cdot & \\ & & & & & & \cdot \end{pmatrix} \begin{pmatrix} \cdot \\ \cdot \\ c_{i-1}^{n+1} \\ c_i^{n+1} \\ c_{i+1}^{n+1} \\ \cdot \\ \cdot \end{pmatrix} = \begin{pmatrix} \cdot & & & & & & \\ & \cdot & & & & & \\ & & \cdot & & & & \\ & & a_i & b_i & c_i & & \\ & & & & \cdot & & \\ & & & & & \cdot & \\ & & & & & & \cdot \end{pmatrix} \begin{pmatrix} \cdot \\ \cdot \\ c_{i-1}^{n} \\ c_i^{n} \\ c_{i+1}^{n} \\ \cdot \\ \cdot \end{pmatrix} \quad (6.9)$$

$$A_i = \frac{1}{2\, r_i\, \Delta^{\pm} r_i} - \frac{1}{2\, \Delta r_{i+1}\, \Delta r_i}$$

$$B_i = \frac{1}{D\, \Delta t^{n+1}} + \frac{1}{2\Delta r_{i+1}\, \Delta r_i} + \frac{1}{2(\Delta r_{i+1})^2}$$

$$C_i = -\frac{1}{2\, r_i\, \Delta^{\pm} r_i} - \frac{1}{2(\Delta r_{i+1})^2}$$

$$a_i = -A_i$$

$$b_i = \frac{1}{D\, \Delta t^{n+1}} - \frac{1}{2\Delta r_{i+1}\, \Delta r_i} - \frac{1}{2(\Delta r_{i+1})^2}$$

$$c_i = -C_i$$

$$\Delta t^n = t^n - t^{n-1}$$

$$\Delta r_i = r_i - r_{i-1}$$

$$\Delta^{\pm} r_i = r_{i+1} - r_{i-1}$$

Boundary Conditions

The diffusion into the substrate was treated in a similar way to that described in Section 6.3.3. The concentration below the drop was set back to $c^{n+1} = c^n \cdot \Delta t \cdot 6 \times 10^{-3}/\mathrm{s}$ after each time step, which is a value only slightly lower than the maximal concentration c_{max} . This had to be done as a setback to the maximum concentration produced an oscillation within the drop region. The difference between a setback to c_{max} and the thus calculated lower value was however negligible within the drop with the concentration rising to $c > 0.95 \cdot c_{max}$ within two to three grid steps (a few μm) starting from the rim.

The position of the rim of the drop was evaluated using a linear interpolation between the data points.

The boundary condition for c_0 at $r = 0$ was described using a Taylor expansion:

$$c(r) = c_0 + r \left.\frac{\partial c(r)}{\partial r}\right|_{r_0} + \frac{r^2}{2} \left.\frac{\partial^2 c(r)}{\partial r^2}\right|_{r_0} + \cdots \tag{6.10}$$

$$\tag{6.11}$$

Using Fick's 2^{nd} law and symmetry arguments this leads to the following finite differences equation for r_0:

$$c_0^{n+1} = c_0^n \left(1 - (2D \frac{\Delta t^1}{\Delta r_1})\right) + c_1^n \, 2D \frac{\Delta t^1}{\Delta r_1} \tag{6.12}$$

which implies for the matrices:

$$A_0 = 0 \qquad a_0 = 0 \tag{6.13}$$

$$B_0 = 1 \qquad b_0 = 1 - \left(2D \frac{\Delta t^1}{\Delta r_1}\right) \tag{6.14}$$

$$C_0 = 0 \qquad c_0 = 2D \frac{\Delta t^1}{\Delta r_1} \tag{6.15}$$

$$\tag{6.16}$$

As the problem is treated in an implicit scheme the value at point $r_0 = 0$ is itself dependent on the values of all other points. Therefore the axis was extended to the left and so-called ghost points were created. The amount of ghost points for explicit schemes is regularly determined by the highest order of differentiation in the Taylor expansion. However in implicit schemes this is not feasible as the solution of each time step depends on the value of all points and an abrupt cut off would therefore set another arbitrary boundary. Therefore the whole axis was mirrored to form a whole ghost axis that was then symmetrically filled with the concentration profile of the regular r-axis after each time step. This approach for simulating the boundary condition is also used in astrophysics (see the review of Shu [1997] and references therein).

The volume loss was then calculated by integrating the concentration profile of the fluid PDMS within the thin film outwards. The integration was done with a trapezoidal routine.

Convergence

The amount of time it takes to do the matrix inversion is the limiting factor concerning the number of grid points. The matrix of the set of linear equations that has to be solved for each time step in the simulation is tri-diagonal. An efficient algorithm will invert a tri-diagonal matrix in n steps, where n is in the order of the number of grid points. This is the case for the IGOR routine used to solve tri-diagonal matrices. Still the inversion of a large matrix at every time step will need too much time. Therefore is is necessary to determine the convergence of the simulation in relation to the number of needed grid points so as to be able to use a

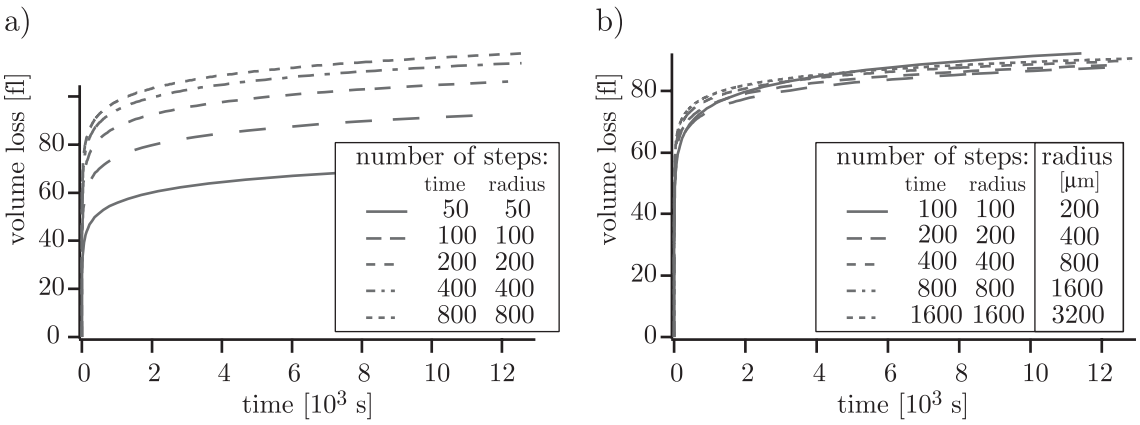

Figure 6.10: a) Numerical simulation for a drop calculated for a substrate with a maximum radius of 200 µm with different numbers of grid points. The simulation converges. b) Numerical simulation for a drop calculated for a substrate with different radii but with the same density of lateral grid points per µm. It can be seen that the calculated volume loss does not depend much on the chosen maximum radius if it is above 200 µm.

number of grid points high enough to lead to a convergent solution, but low enough not to lead to an enormous number of operations.

As can be seen in Fig. 6.10 the algorithm converges. The outer radius of the calculated area does not influence the outcome considerably for radii larger than 200 µm. Therefore the used number of grid points and the outer radius were chosen accordingly for all simulations with an outer radius of 600 µm and a grid size of 800–1600 time and radius steps.

Comparison of the Simulation to the Data

The simulation procedure does not differ from what is described in literature as a way to calculate diffusion processes; still this simulation can only be used to show a qualitative consistency between data and simulation. This is because the results of the simulation depend strongly on the input parameters in a way that leaves the general shape of the curve unaltered, but changes the magnitude of the calculated volume loss by a factor that might be as large as several orders of magnitude. If one allows for a rescaling with this factor, the calculated curves match the data nicely.

In Fig. 6.11 graphs of data and simulation for three different experiments are shown. As can be seen most clearly in the logarithmic plot, the simulation can account for the the volume evolution of the drops over the whole time-scale. The slowing down of the volume loss in the later decades of the diffusion process that could not be seen in the semi-analytical calculations according to Jaeger is now an especially distinctive feature. This implies that the slowing down of the volume loss is indeed due to the decreasing drop base radius as this is the most fundamental difference in the underlying assumptions of the two approaches.

The magnitude of the volume loss depends strongly on the start values. This is a well known problem in diffusion simulations [Spiegelman, 2000], which could not be solved in the scope of this thesis.

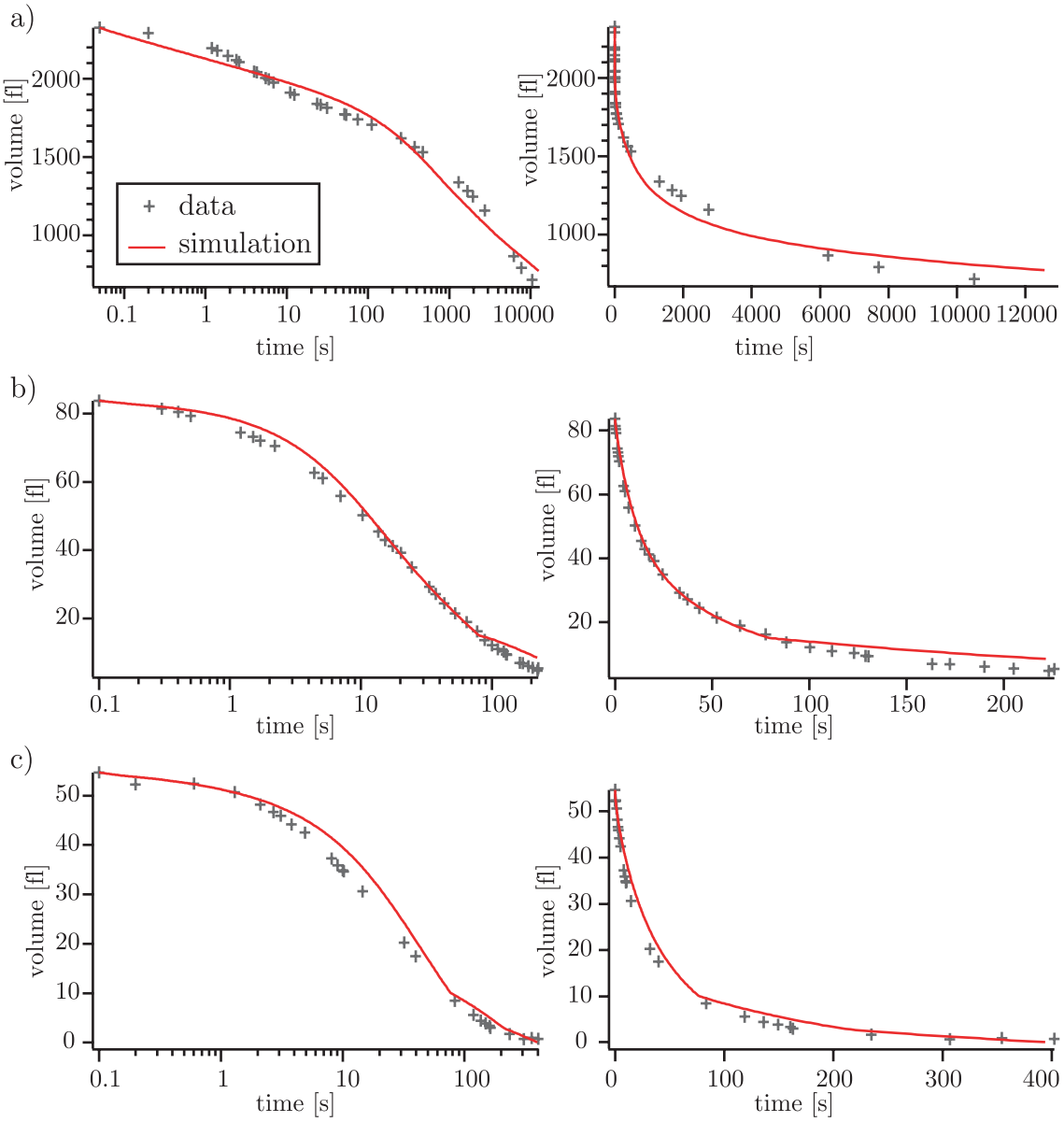

Figure 6.11: Three examples of volume loss data of drops of fluid PDMS on a thin film of cross-linked PDMS compared to the results of the numerical simulation of the diffusion process with logarithmic (left) and linear (right) coordinates. The numerical simulation follows the data closely for all times. The grid size used was within the range of convergence as determined in Section 6.3.4.

6.4 Contact Angle

6.4.1 Determination of the Contact Angle

The contact angle was determined as the maximum angle of a spherical cap fit to the reconstructed height profile (for an example of the spherical cap fit see Fig. 6.2).

The contact angle can also be determined by more straightforward methods such as differentiating the data or fitting a straight line to the rim. These methods give contact angle data with the same magnitude as compared to the spherical cap fit, but with considerably more scatter. This scatter is mainly due to the influence of the position of the fitting region, which can be minimised using the spherical cap fit.

The contact angle measured using the spherical cap fit depends only in a minor fashion on the choice of the fitting region. This is also illustrated in Fig. 6.12 where the contact angle for the height profile of Fig. 6.2 was determined 10 times. The fitting region was varied by moving both end points. The resulting variation of the contact angle is less than 0.3° with a standard variance of 0.09°.

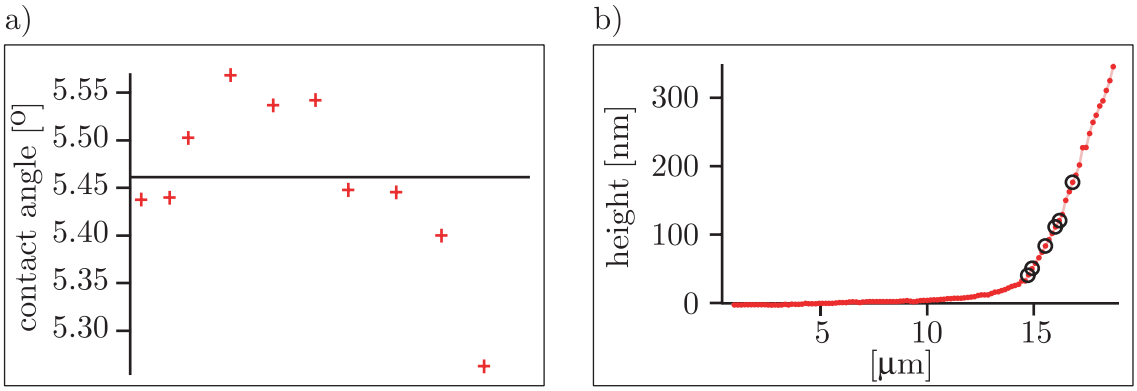

Figure 6.12: Contact angle of the height profile of Fig. 6.2 measured several times using a spherical cap fit with different fitting regions (shown in a)). For the first five measurements the left edge of the fitting region was varied, starting from the points depicted in b) (from left to right). For the last four fits the left edge was taken as the second point in b) whereas the right edge was varied starting from the right rim of the drop up to the center of the drop. The resulting contact angle is $\theta = 5.46° \pm 0.09$ (grey line). The maximum variation of the measured angle is less than 0.3°.

6.4.2 Power-law Behaviour of the Contact Angle

A drop that is deposited onto a non-penetrable substrate will either spread or dewet to reach its equilibrium shape as described in Chapter 3.1.2. A drop deposited onto a porous material will also try to reach its equilibrium contact angle by wetting or dewetting. Since the drop loses volume to the substrate, however, the kinetics will differ from those of a drop on a non-penetrable substrate.

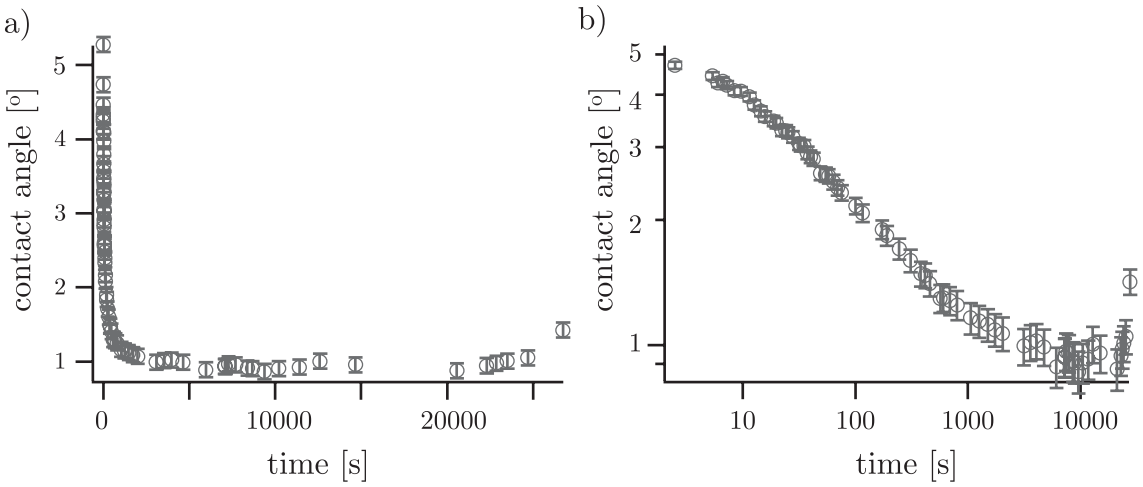

Figure 6.13: Characteristic example of the contact angle behaviour.
a) linear scale
b) double logarithmic scale

A characteristic example of the time dependence of the contact angle of a drop of fluid PDMS on a substrate of cross-linked PDMS is shown in Fig. 6.13. The contact angle starts with an initial value at $t = 0$, which depends on the exact conditions of the drop deposition and cannot be predicted even though there is a general tendency for bigger drops to have larger initial contact angles.

The contact angle kinetics starts with a fast decrease from the initial value which then slows down considerably as can be seen in Fig. 6.13 a). In a double logarithmic plot the typical features of this process can be distinguished (see Fig. 6.13 (b)). Here the dynamics starts with a slight shoulder and then cross over into a rather straight line that indicates a power-law behaviour. In the majority of experiments a slight increase of the contact angle can be seen at long times.

Theories of the contact angle kinetics for a drop on a non-penetrable surface predict a power-law dependence of the contact angle as described in Chapter 3.1.2. However the kinetics of a drop that is deposited onto a porous or otherwise penetrable surface can in general not be predicted with these theories [Clarke et al., 2002; Starov et al., 2002a,b].

Nevertheless, in a double logarithmic plot all our experiments show a straight part in their contact angle behaviour, which indicates a power-law. In most experiments the straight parts can be distinguished clearly over more than one decade of time (see Fig. 6.14 and Fig. 6.15). In the following the power-law behaviour of the contact angle will be shown in detail.

Measurements on a Film of Cross-linked PDMS with Long Cross-linker (DMS-V31)

Representative data of two sets of experiments on a film of cross-linked PDMS with long cross-linker (DMS-V31) are shown in Fig. 6.14. The resulting fit of the function $\Theta = A \cdot t^B$ with the free parameters A and B gives an exponent B of approxi-

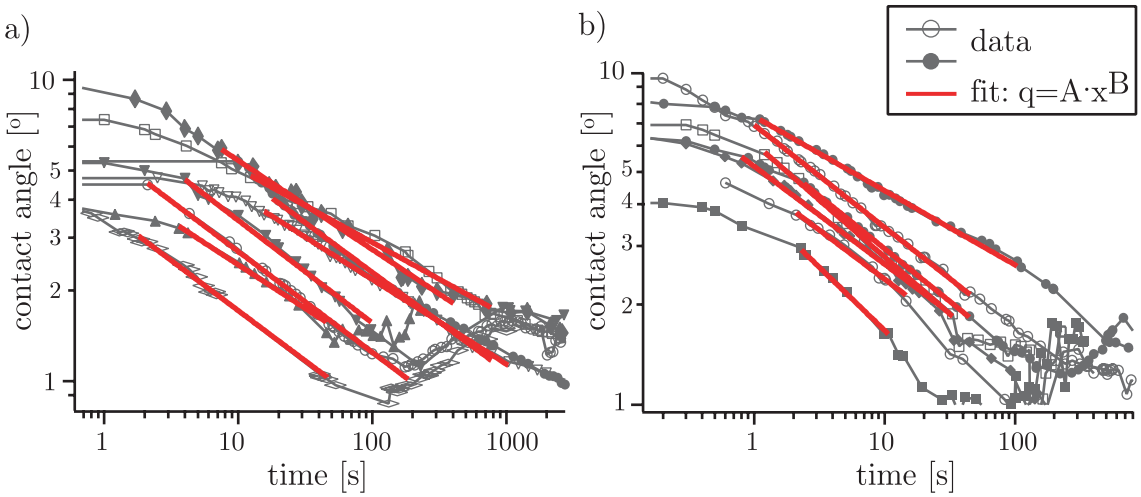

Figure 6.14: Measurements of the contact angle of drops of fluid PDMS on a thin film of cross-linked PDMS with long cross-linker (DMS-V31). The power-law behaviour is clearly visible as a straight decline, the exponent of the fit is around -0.3 for all measurements.

a) Long PDMS (DMS-T22) with polar fraction. Exponents of the fits, top to bottom:

-0.244 ± 0.007 -0.295 ± 0.009 -0.329 ± 0.007 -0.280 ± 0.003 -0.340 ± 0.010
-0.334 ± 0.004 -0.289 ± 0.010 -0.333 ± 0.008

b) Short PDMS (DMS-T21). Exponents of the fits, top to bottom:

-0.232 ± 0.003 -0.308 ± 0.003 -0.316 ± 0.002 -0.342 ± 0.004 -0.294 ± 0.007
-0.294 ± 0.011 -0.379 ± 0.012

mately -0.3, which is in agreement with the hydrodynamic theory (see Chapter 3.1.2, Eq. 3.28). [2] The values of the exponent for all experiments can be seen in Appendix E Tables E.3 and E.4; the mean values for the different sets of data can be seen in Table 6.4.2. The exponent does not depend on the involved surface tensions or viscosities as the exponent of the fits of all three different fluid samples is similar.

Type of fluid PDMS	Viscosity in cSt	Surface Tension in mJ/m^2	Number of Experiments	Exponent
DMS-T22	200	36.8	6	-0.29 ± 0.06
DMS-T22 with 0.1% polar YBD-125	200	27.7	13	-0.31 ± 0.05
DMS-T21	100	36.8	7	-0.31 ± 0.05

Table 6.1: Exponents of the power-law behaviour of the contact angles on thin films of cross-linked PDMS with long cross-linker (DMS-V31).

[2] Note however that the exact size and position of the fit region is determined manually and can alter the exponent of the fit up to 15-20%.

Measurements on a Film of Cross-linked PDMS with Short Cross-linker (DMS-V21)

The same measurements were done for a system in which a shorter cross-linker (DMS-V21) was used for the preparation of the thin film of cross-linked PDMS. This was done to check for the influence of the velocity of the diffusion as a shorter cross-linker should diminish the speed of diffusion into the substrate. This is due to the fact that a shorter cross-linker will form a more densely cross-linked network. Following Garrido et al. [1988], diffusion in a network has a behaviour intermediate between free and entangled diffusion, a denser network would therefore lead to a smaller diffusion coefficient.

As can be seen in Fig. 6.15 the data still support a power-law behaviour, only in this case the exponent is as small as -0.05. The exact values for the different sets of experiments on cross-linked PDMS with short cross-linker are shown in Table 6.4.2.

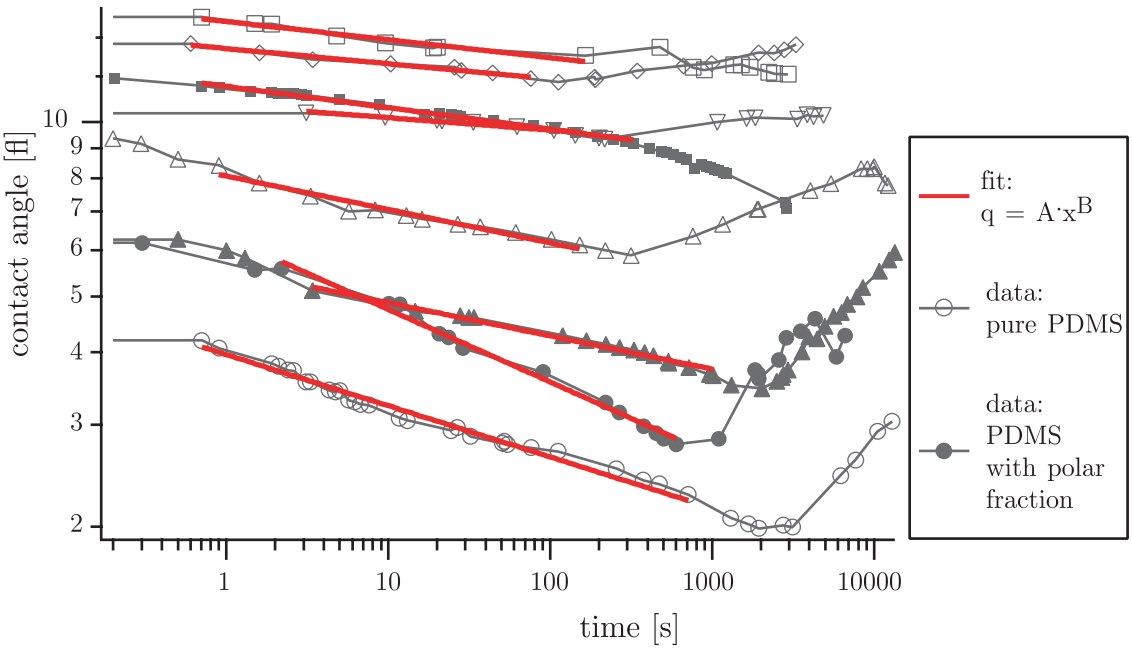

Figure 6.15: Measurements of the contact angle of drops of fluid PDMS on a thin film of cross-linked PDMS with short cross-linker (DMS-V21). The power-law behaviour is visible as a straight decline, however the exponent of the fit is as small as -0.05 for all measurements. The fluid PDMS was long PDMS (DMS-T22) with and without polar fraction.

The exponent of -0.05 is in strong contrast to the measurements on films with long cross-linkers which exhibit a power-law behaviour with an exponent of app. -0.3.

If we reconsider the short-time behaviour of the contact angle of drops on substrates with long cross-linkers (Fig. 6.14), however, the plots might be interpreted in a way that a short period with a power-law behaviour with a low exponent might precede the long decline with an exponent of -0.3. While in some measurements this flat region is very speculative, there are enough experiments where it can be seen clearly.

Type of fluid PDMS	Viscosity in cSt	Surface Tension in mJ/m^2	Number of Experiments	Exponent
DMS-T22	200	36.8	5	-0.05 ± 0.03
DMS-T22 with 0.1% polar YBD-125	200	27.7	3	-0.07 ± 0.05

Table 6.2: Exponents of the power-law behaviour of the contact angles on thin films of cross-linked PDMS with short cross-linker (DMS-V21).

A good example is depicted in Fig. 6.16 where two flat slopes representing power-law behaviour with exponents of -0.1 and -0.3 can be distinguished.

The reduced rate of diffusion within the substrate with shorter cross-linker might slow down the process of contact angle equilibration in a more pronounced way than the volume loss leading to a situation where the whole drop disappears into the substrate before the second regime of the contact angle's power-law behaviour will be reached.

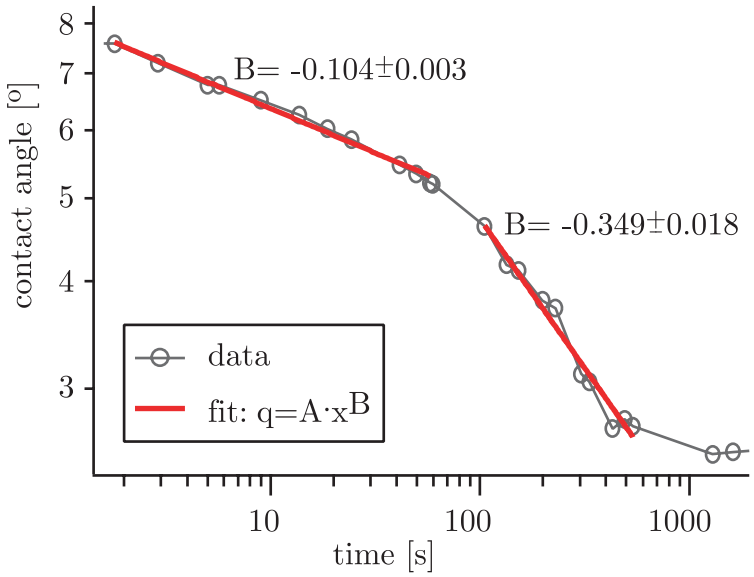

Figure 6.16: Measurement of the contact angle of a drop of fluid PDMS (DMS-T22) on a thin film of cross-linked PDMS with long cross-linker (DMS-V31). Two domains of power-law behaviour can be distinguished with exponents of approximately -0.3 and -0.1.

6.4.3 Long-time Behaviour: Increasing Contact Angle

The contact angle reaches a minimum θ_r at a time t_r and increases afterwards. A few examples of this behaviour are shown in Fig. 6.17. The minimum of the contact angle occurs at the same time t_r at which the direction of movement of the contact line reverses as can be seen in Fig. 6.18. There the drop base radius and the contact angle of a few experiments are simultaneously plotted.

Applying the concept of advancing and receding contact angles, we observe a behaviour in which the advancing contact angle is smaller than the receding one. This is in stark contrast to the regular theory of advancing and receding contact angles and has not been described in the literature before.

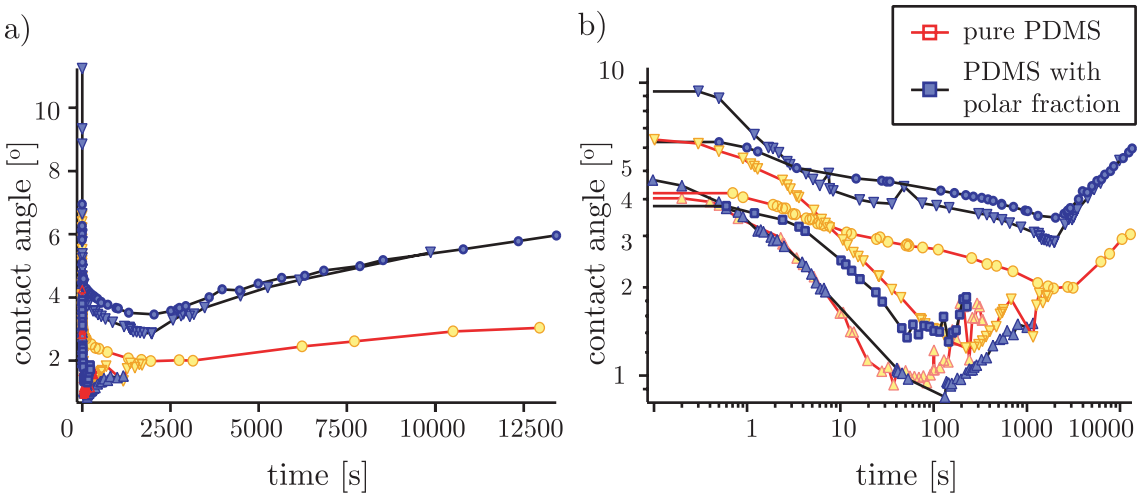

Figure 6.17: Examples of increasing contact angles at long times.
a) Linear plot.
b) Double logarithmic plot.

The increase of the contact angle for long times can be seen in approximately 80% of experiments, but not in all experiments. There are several reasons why this might occur. Firstly not all drops were observed until their volume reached zero. This was due to the fact that in the case of large drops the time required to do so was too long to be within the reach of the performed experiments[3]. In this case a possible increase of the contact angle for long times could have taken place after the end of observation. As a second possibility the increase of contact angle for very small drops might be smaller than the error of measurement and therefore invisible, especially as the error of measurement increases for small angles.

The increase of the contact angle for long times must be attributed to forces acting at the rim of the drop. A force acting at the rim of the drop can drag the contact line outwards even beyond the static equilibrium contact angle. A minimum contact angle will occur if this outward force then decreases over time and falls beneath the magnitude of an antagonist force. This force will then manage to pull the rim inwards again. This would lead to an increasing contact angle. Forces that could possibly lead to such a behaviour are described in the following. Note, however, that this phenomenon can only occur in non-equilibrium.

[3]Longest observation time was 7.5 h.

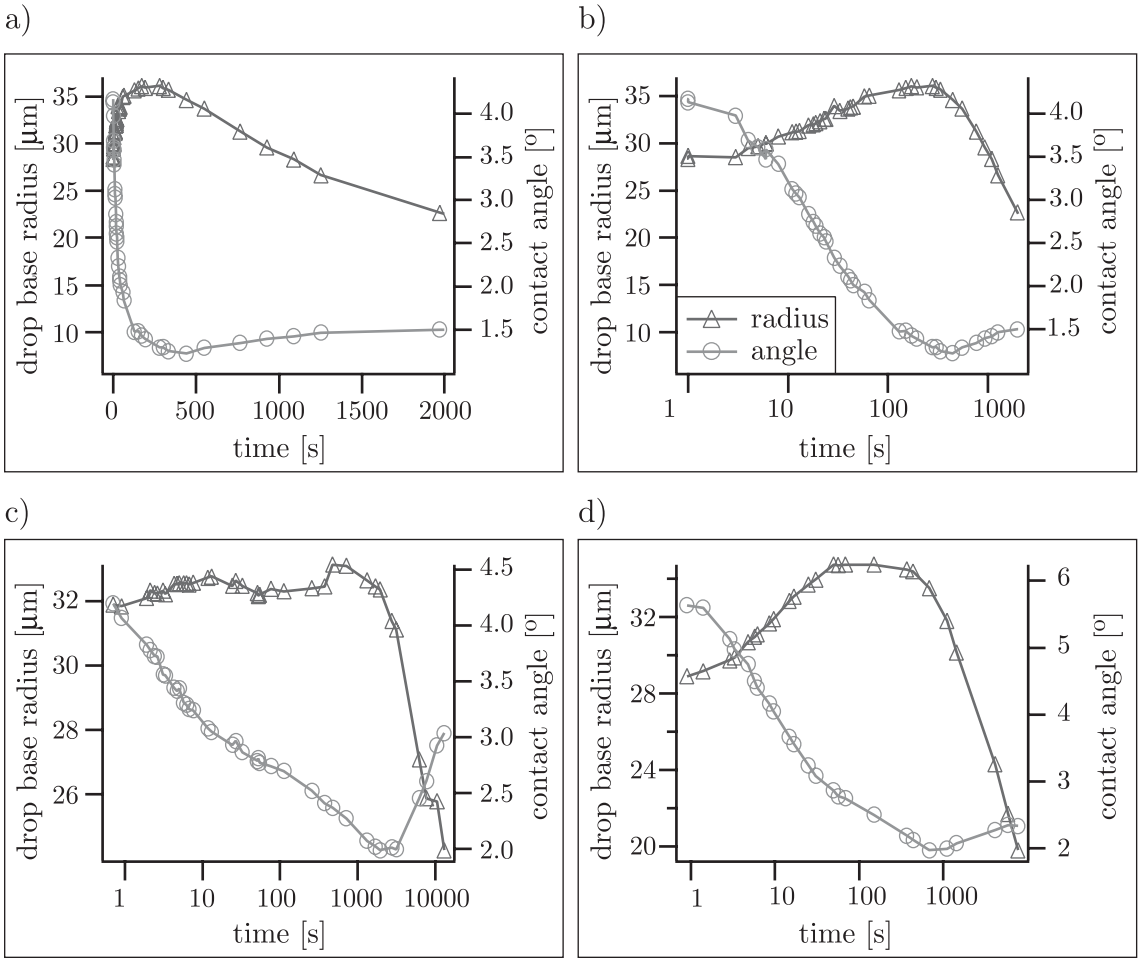

Figure 6.18: Comparison of the turning points of the contact angle and the radius.
a)-b) Drop of DMS-T22 with polar fraction on a substrate with long cross-linker, linear and logarithmic.
c) Drop of DMS-T22 on a substrate with short cross-linker.
d) Drop of DMS-T22 on a substrate with long cross-linker.

Line Tension Generated by the Liquid-fluid Interface at the Time of Reversal

In the case of a drop on a non-penetrable surface the forces acting on the rim of a drop can be attributed to the various terms of the surface tension that lead to Young's Law (see Chapter 3.1.1, Eq. 3.5 and Fig. 3.1). In a non-equilibrium situation these forces will be counteracted by viscous drag.

In all cases the force on the rim generated by the liquid-fluid interface is acting in the inward direction and equals $F_{LF} = \gamma_{LF} \cdot \cos\theta$. This force decreases from its initial value as the contact angle decreases. At the point of return θ_r this force will exhibit a minimum $F_{r,LV}$. Even though the values of θ_r are distributed between 0.03–2.0°with a mean of 1.0666 ± 0.124, the cosine of the contact angle is nearly constant and independent of the drop base radius R_r at the time of reversal t_r (see Fig. 6.19) as the cosine function is nearly horizontal for small angles. Nevertheless this implies that the generated force is independent of the drop base radius R_r.

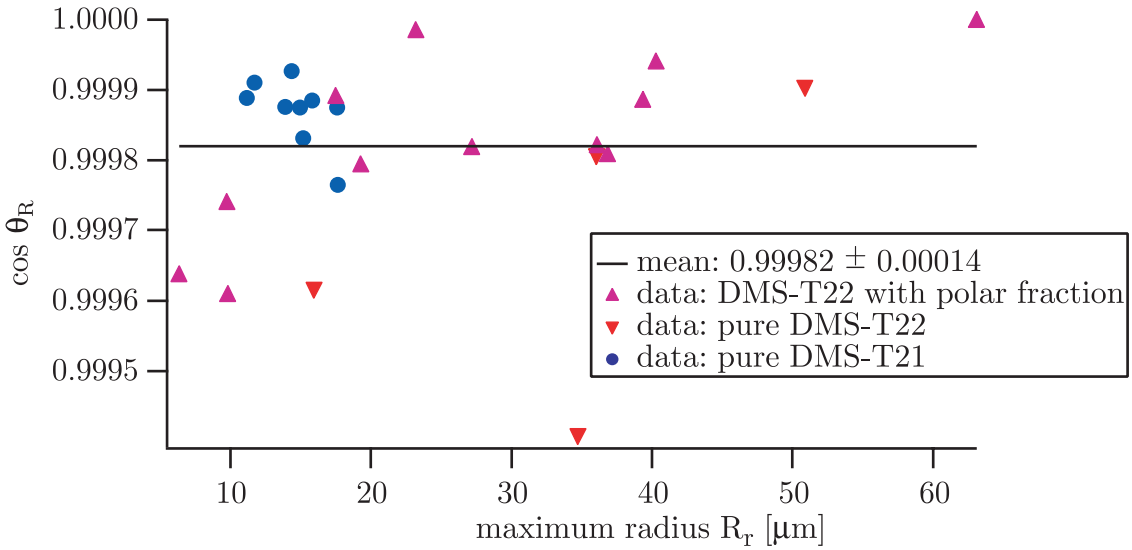

Figure 6.19: The cosine of the minimal contact angle θ_r at the time of reversal t_r of the contact line is approximately constant.

Force on the Rim Generated by the Diffusion Process

In the case of a drop of fluid polymers on a permeable substrate, however, the concept of surface tension cannot be applied to the interface between drop and solid substance. Polymers in the drop will diffuse into the substrate, thus interacting with the diffusion process and making it impossible to define a static surface free energy of this interface; instead the forces generated by the concentration gradient within the substrate have to be considered.

A sketch of how these forces generated by the diffusion process might interact with and influence the drop is shown in Fig. 6.20.

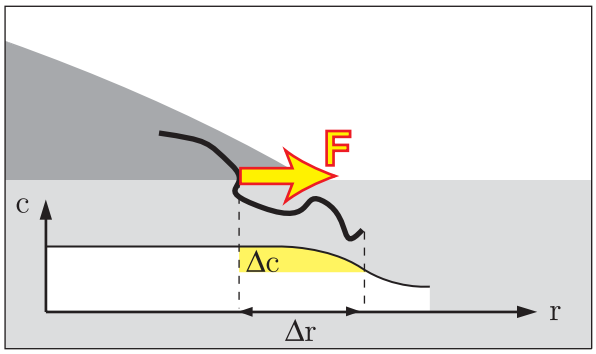

Figure 6.20: A concentration gradient along the length of a polymer in the substrate will generate a net force. Polymers that cross the drop-substrate interface will then pass on this force to the drop.

A concentration gradient along the length of a polymer in the substrate generates a net force on the polymer that is proportional to the concentration gradient. Polymers that cross the drop-substrate interface will then pass on this force to the drop.

The force that a single polymer can pass on to the drop will be tangential to its orientation. As the polymers are randomly distributed within the drop, the net force is zero apart from the rim region where the wedge leads to symmetry breaking.

The force on the polymers can be related to the gradient of the chemical potential, which depends on the concentration as:

$$\mu = \mu_0 + k_B T \ln c \tag{6.17}$$

where c is the mole fraction. The force generated by a concentration gradient is then:

$$\frac{\partial \mu}{\partial r} = F = \frac{k_B T}{c} \frac{\partial c}{\partial r} \tag{6.18}$$

As the radius R_r at the turning point is still of the magnitude of the initial radius, the semi-analytical solution of Jaeger [1942] as described in Chapter 3.2.3 still delivers a good approximation of the diffusion process and can be used to determine the concentration gradient. Using Eq. 3.41, the concentration gradient can then be expressed in terms of $I(0,1,\alpha)$:

$$\Phi(R_r,t) = 2\pi\, D \left(r \frac{\partial c}{\partial r} \right)_{r=R_r} = \frac{8D\, c_0}{\pi}\, I(0,1,\alpha_r)$$

which leads to

$$F = \frac{k_B T}{c} \left(\frac{\partial c}{\partial r} \right)_{r=R_r} = \frac{4\, k_B T}{R_r\, \pi^2} I(0,1,\alpha_r) \tag{6.19}$$

where $\alpha_r = D t_r / R_r^2$.

Calculating I(0,1,α) for the values of $\alpha_r = D t_r / R_r^2$ from the data, it seems that I(0,1,α_r) does not depend on the maximum radius R_r, but can be considered as nearly constant with a mean of 2.6 ± 0.8. This is depicted in Fig. 6.21.

As I(0,1,α_r) is a monotonous function and is constant for all experiments, $\alpha_r = DT/R_r^2$ is also constant with a mean value of $\alpha = 0.8$. This implies a power-law

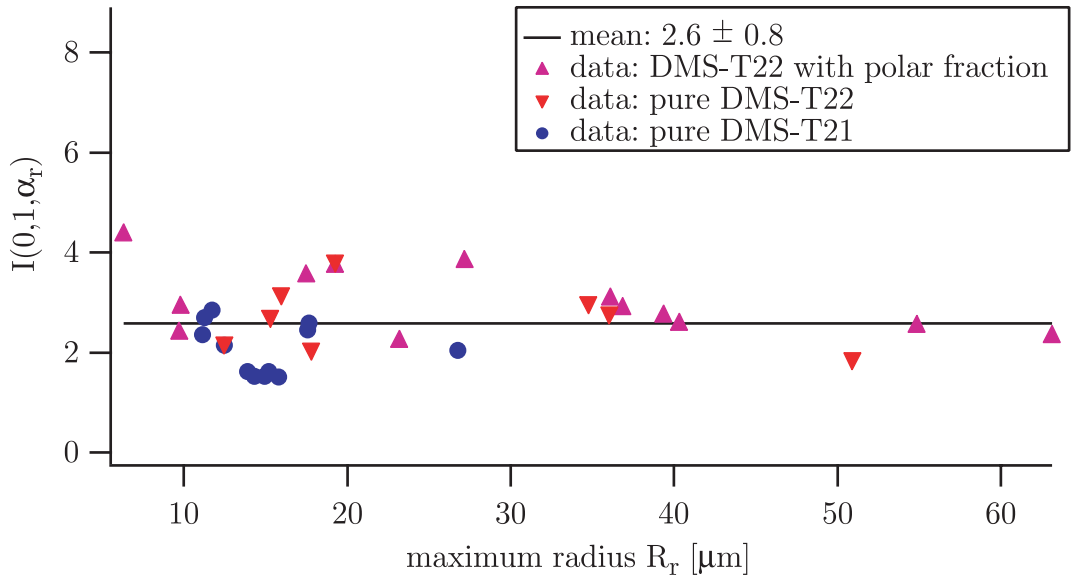

Figure 6.21: The integral I(0,1,α_r) is constant at the turning point of the contact line with a mean of $I(0, 1, D\,t_r/R_r^2) = 2.6 \pm 0.8$.

behaviour of $R_r = \sqrt{D\,t_r/\alpha_r} = A\sqrt{D\,t_r}$. As can be seen in Fig. 6.22 this power-law behaviour is prominent over three decades of time. Note that the error of t_r is relatively large due to the fact that it is taken at a point where the curve of the drop base radius is a smooth curve that is nearly horizontal.

The increase of the contact angle after its minimum might then be explained by the fact that once the drop base radius starts to shrink, the drop recedes over a part of the substrate that is already saturated with liquid polymer. This implies that the concentration gradient can be considered to be nearly zero. Therefore the force derived from the concentration gradient should diminish and the drop will equilibrate towards its Young angle.

This theory relies on the fact that a polymer penetrates a substrate and implies that the increase of the contact angle should not occur when a simple non-polymeric liquid or a non-permeable substrate is used. As a matter of fact this behaviour cannot be seen in experiments on non-penetrable surfaces and experiments with non-polymeric liquids on porous substrates [Bacri and Brochard-Wyart, 2000; Clarke et al., 2002; Denesuk et al., 1993; Starov et al., 2003]. This indicates that the behaviour does indeed depend on the polymeric nature of the penetrating liquid.

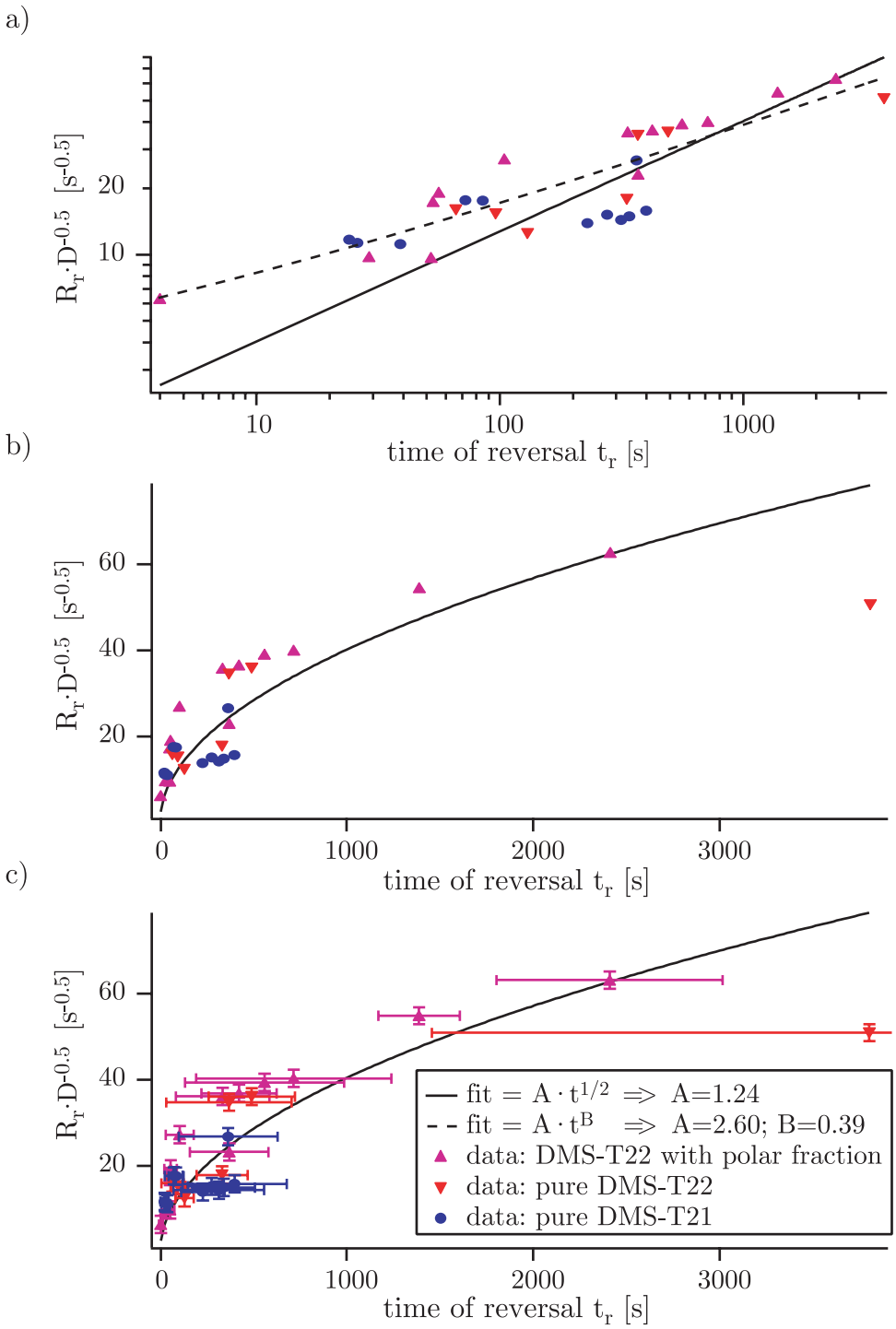

Figure 6.22: The relationship between drop base radius R_r at the time of reversal t_r and the time of reversal t_r can be described using a power-law in the form $R_r = A\,(D \cdot t_r)^{1/2}$. The coefficient in the fit is $A = 1.24 \pm 0.08$, which is close to the inverse mean of $\sqrt{\alpha_r}$: $1/\sqrt{\alpha_r} = 1/\sqrt{0.8} = 1.12$. Fitting the exponent gives a power-law $R_r = 2.6\,(D \cdot t)^{0.39}$. This is close to the expected behaviour. Shown are experiments done on a film of cross-linked PDMS with long cross-linkers (DMS-V31) that exhibit a rising contact angle for long times.

Chapter 7

Outlook

7.1 Including the Wetting Process into a Simulation

As the theory of diffusion leads to complicated mathematics when regarding the diffusion of the liquid into the penetrable network, it was not possible to mathematically couple the diffusion process to the wetting and obtain a unified description of the whole process. This is possible, however, in the case of a setup with a porous membrane as penetrable film.

The simulation of the diffusion process as described in Chapter 6.3.4 has shown that it is possible to take account of the data in a numerical way, even if the outcome lacks accuracy.

Therefore it seems possible to extend this approach to including the drop and it's wetting behaviour into another simulation. This could then help determining the driving force for the otherwise misterious contact angle increase for long times.

7.2 Applications in Biophysics

The study of the behaviour of living cells is one of the most interesting topics in biophysics. All solid surfaces, however, suffer from frozen surface defects. As cells react very strongly to those defects even in tiny concentrations, it is unclear whether any observed behaviour is indeed due to the tested experimental conditions or rather due to those unknown surface defects. This impedes clear interpretation of taken data.

Fluid surfaces do not suffer from frozen surface defects, as these defects heal instantaneously. Using fluid surfaces as substrates for experiments with living cells would therefore alleviate the interpretation of any measurement as the substrate will be better defined.

Experiments using such substrates have not been done up to now. This is due to the restrictions posed onto such substrates. Biophysical experiments with living

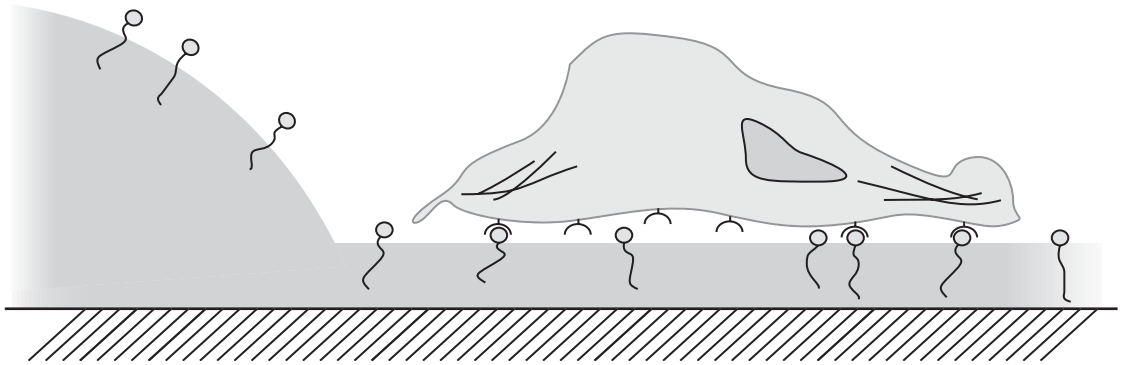

Figure 7.1: Experiments with living cells on fluid surfaces will not suffer from limitations due to frozen surface defects as such surface defects heal instantanously on fluid surfaces. Mobile receptors can be incorporated into the fluid surface by the use of polymer anchors.

cells have to be done using light microscopy due to their inhomogeneity and small size. The used fluid has to be transparent, bio-compatible, and form a thin film in an aqueous medium thus providing a controllable surface.

The setting up of such a system is therefore a demanding task and requires a thorough understanding of the involved processes. Especially an improved understanding of the wetting behaviour of polymer films under water will be essential to any further projects. Therefore the study of the wetting behaviour near the wetting transition as perforemed in this thesis was a first and important step towards the establishment of such systems.

Appendix A

Bio-compatibility Tests with Endothelium Cells

To test the bio-compatibility of siloxanes compared to that of different alkanes, the growth behaviour of human umbilical vein endothelial cells (HUVEC) on collagen coated cover slips immersed in a cell culture medium saturated with the respective polymer was observed. As HUVECs are primary mammalian cells they are very sensitive and can be used for stringent testing of bio-compatibility. The tested polymers were tetradecane, pentadecane, hexadecane and mixtures of polydimethylsiloxane with polydimethylsiloxanes with different side-groups as described below.

The used HUVECs were provided by Martin Aepfelbacher of the Institut für Kreislaufprophylaxe und Epidemiologie der Ludwig-Maximilian-Universität München. The cells were kept on Collagen G coated plastic culture flasks with Collagen G consisting of 90 % collagen I and 10 % collagen III (Biochrom, Berlin, Germany). The used cell culture medium was an EGM (Promo Cell, Heidelberg, Germany) containing ECGS/H2 (Endothelial cell growth supplement/Heparin) and 10% FCS at 5% CO_2 and 37°C in a humidified atmosphere (see also [Lindl and Bauer, 1994].

Before the test the used glass cover slips ($18 \times 18\,\mathrm{mm}^2$, Menzel Gläser, Germany) were washed with Hellmanex solution (Hellma GmbH, München, Germany) in a sonicator, rinsed several times with Millipore water, sterilized by washing in ethanol solution and dried. Before use cover slips were coated for 2 hours or overnight with $100\,\mu\mathrm{g/ml}$ collagen G (Biochrom, Berlin, Germany) to encourage adhesion and washed twice with PBS.

To produce cell medium saturated with the various polymers, a small quantity of the polymer oil (app. 1 ml) was put into cell culture medium (app. 5 ml). The mixture was shaken well and then left to settle for a day until the oil was clearly separated from the aqueous cell culture medium and then decanted. The so-obtained saturated medium was clear and free of oil drops as observed with phase contrast microscopy. All polydimethylsiloxanes were purchased from ABCR, Karlsruhe, all alkanes were purchased from Sigma-Aldrich Chemie GmbH, Steinheim in *purum* quality.

	Outcome
Decane	No cells on cover slip
Undecane	No cells on cover slip
Dodecane	A few patches of cells on cover slip
Tridecane	No cells on cover slip
Tetradecane	A few patches of cells on cover slip
Pentadecane	No cells on cover slip
Hexadecane	A few patches of cells on cover slip

	Outcome
Dimethylsiloxane DMS-T22	Dense cell layer on cover slip
DMS-T22 with 10^{-4} YBD-125	Dense cell layer on cover slip
DMS-T22 with 10^{-5} DBE-224	Dense cell layer on cover slip
DMS-T22 with 10^{-6} ALT-143	Dense cell layer on cover slip
Cell medium without polymers	Dense cell layer on cover slip

ABCR N°	
DMS-T22	Dimethylsiloxane
YBD-125	(Carboxylate-pyrolidonepropyl)methylsiloxane-dimethylsiloxane copolymer
DBE-224	Dimethylsiloxane-ethylene oxide block copolymer
ALT-143	polyoctylmethylsiloxane Homopolymer

Table A.1: Outcome of bio-compatibility tests with HUVECs in polymer-saturated cell culture medium. Whereas cells treated with alkane-saturated cell culture medium did not prosper well, the comparison of cells kept in siloxane-saturated medium showed no difference to cells kept in pure cell culture medium.

HUVECs (4×10^4 cells) were plated onto the collagen -coated cover slips and grown in the cell culture medium saturated with the polymer oils for 3–4 days with a sample grown with pure cell culture medium as a reference measurement. Each different condition was tested using two cover slips in separate containers.

Then the density of the cells was evaluated. Cells treated with alkane saturated cell culture medium did not prosper well, whereas cells kept in siloxane saturated medium showed no difference in appearance and density to cells kept in pure cell culture medium.

As HUVECs are very sensitive to changes in their environment, this is a clear indication that the used polydimethylsiloxanes are bio-compatible.

Appendix B

Surface Tests

As wetting experiments with PDMS in an aqueous environment had not been done before, it was an important first step to identify a surface that would allow experiments near the wetting transition.

A multitude of different surfaces were tested for the wetting behaviour of PDMS oil in ambient water. The aim was to find a substrate that facilitates wetting near the wetting transition, i.e., with small contact angles of only a few degrees.

This was checked by testing the behaviour of a thin film of fluid PDMS on the substrate upon immersion in water. For dewetting films of the same viscosity, the rate of dewetting is proportional to the spreading parameter S [Martin et al., 1994] and with Eq. 3.15 $S = \gamma_{LF}(\cos\theta_{LF} - 1)$ connected to the contact angle θ_{LF}. So if the thin film dewetted fast and therefore with a large contact angle, the substance was rejected for further use, whereas a desired substrate would exhibit no dewetting or a slow dewetting with a small contact angle.

As water is a strongly polar liquid, the fluid PDMS which was put on top of the substrates was mixed with siloxanes with different side groups to check for the influence of the thus altered interfacial energies. All polydimethylsiloxanes were purchased from ABCR (Karlsruhe, Germany). The used mixtures were:

- Polydimethylsiloxane (DMS-T22)
- PDMS (DMS-T22) with fractions of polar (carboxylate-pyrolidonepropyl)-methylsiloxane-dimethylsiloxane random co-polymer (YBD-125)
- PDMS (DMS-T22) with a fraction of dimethylsiloxane-ethyleneoxide block copolymer (DBE-224)
- PDMS (DMS-T22) with a fraction of polyoctylmethylsiloxane (ALT-143)

Some relevant physical parameters of the used polymers and the mixing ratio of the used mixtures are shown in Table B.1.

	Viscosity in cSt.	Refractive index	Fraction of polymer in DMS-T22
DMS-T22	200	1.4030	
YBD-125	400-600	1.4052	$10^{-2}, 10^{-3}$
DBE-224	400	1.4140	10^{-5}
ALT-143	600-1000	1.445	10^{-6}

Table B.1: Shown here are the physical properties of the different fluid batches of PDMS used in the experiments and the mixing ratio of the used mixtures. All data is taken from the manufacturer's handbook.

The solid substances were either put on a cover slip or used as bulk material. The substrate was put on the stage of a microscope and observed by phase contrast microscopy. Then water was put on top of the cover slip and it was checked whether the thin film of PDMS was stable or started dewetting. If the velocity of the dewetting fronts was low enough, it was roughly determined by watching a dewetting front on a monitor and measuring the distance travelled by the front versus time.

Tested surfaces, that were rejected because of rapid dewetting of all mixtures of PDMS oils are described below:

- Glass cleaned with various procedures

  PDMS oil dewets glass very quickly, regardless of the cleansing procedure. The used methods of cleaning were: cleaning with Piranha solution (7 parts 98% sulfuric acid and 3 parts 30% hydrogen peroxide), by plasma treatment, KOH solution (2.5 M) and a procedure using a 2% Hellmanex solution (Hellma, Müllheim, Germany) (see also [Müller-Buschbaum, 2003])
  The influence of different cleansing procedures on the wetting properties of PDMS on a glass cover slip coated with Aquaphobe™ CM (ABCR) was also tested. The dewetting of PDMS oil on cover slips cleaned using Piranha solution and afterwards coated with Aquaphobe generally showed a lot of dewetting defects and pinning points. Cover slips cleaned by plasma treatment also showed these defects. Better results could be obtained using a KOH solution and the most homogenous dewetting was achieved using cover slips cleaned with Hellmanex using the cleansing procedure as described on page 31.

- Glass coated with Aquaphobe™ CM in various concentrations

  Aquaphobe™ CM (ABCR, Karlsruhe, Germany) is a chlorine-terminated polydimethylsiloxane oligomer. By reaction of the chlorines with hydroxy and silanol groups of glass it produces a chemically bound "siliconized" surface. To enhance the wetting properties by forming a more brush-like surface, different amounts of a long chlorine-terminated polydimethylsiloxane ($M_W = 15-20$ kDa, DMS-K26, ABCR, Karlsruhe, Germany) were added.

Clean cover slips were either dipped into or wiped with a solution of Aquaphobe™ CM and then cured at 100°C. PDMS dewets all tested coatings quickly as shown in TableB.2.

Aquaphobe	Long chlorinated PDMS	Velocity of dewetting front upon immersion
5%	5×10^{-5}	App. $0.5\,\mu m/s$
5%	1×10^{-4}	App. $0.6\,\mu m/s$
5%	5×10^{-4}	App. $0.6\,\mu m/s$
5%	2.5×10^{-2}	App. $10\,\mu m/s$
1%		Dewets instantaneously
5%		

Table B.2: Dewetting properties of different Aquaphobe™ coatings.

- Glass with a covalently bound layer of silanes

  Clean glass cover slides were silanized with n-octyltrimethoxysilane (ABCR, Karlsruhe, Germany) using the procedure described in [Steinmaßl, 2000]. All used PDMS mixtures show fast dewetting under water with a velocity of the dewetting fronts of $v > 10\,\mu$m/s on this substrate.

- glass coated with a thin film of polystyrene, polymethylmethacrylate, polycarbonate

  Clean glass was coated with a film of polystyrene using a 1 mg/ml solution of polystyrene 500000 (standard, Sigma-Aldrich Chemie GmbH, Steinheim, Germany) in toluene that was spin-coated onto the glass at 1000 cycles/second for 40 seconds and afterwards dried in vacuum for at least 4 hours. Substrates covered with this films of polymethylmethacrylate (PMMA, M_W = 120.000,Sigma-Aldrich, Steinheim, Germany) and polycarbonate (Dow Deutschland Inc., Schwalbach, Germany) were prepared in an analogous manner from 5 mg/ml solutions. All used mixtures of PDMS dewet those substrates instantaneously.

- Glass coated with a thin film of TOPAS™

  TOPAS™ (5013 pellets, Ticona GmbH, Frankfurt am Main, Deutschland) is a recently developed, highly hydrophobic material that consists of a cyclic olefin copolymer. It was dissolved in toluene to give a 5 mg/ml solution and afterwards spin-coated onto the glass at 1000 cycles/second for 40 seconds and dried in vacuum for at least 4 hours. All used mixtures of PDMS dewet this substrate instantaneously.

The only substrate that would allow a film of fluid PDMS to be stable under water for a reasonable time and showed a small contact angle of only a few degrees was a cross-linked film of PDMS:

- Glass coated with a thin film of cross-linked PDMS

  Clean glass cover slips were coated with a thin film of cross-linked PDMS as described on page 31. A thin film of PDMS oil that was spin-coat onto the substrates and then immersed in water would only show dewetting fronts after several days with contact angles of only a few degrees.

Appendix C

Interfacial Energy Determination – The Drop Weight Method

The drop weight method of Harkins and Brown [1919] is one of the classic methods for determining the interfacial tension between two phases (fluid/fluid or fluid/vapour). Even though today the axis-symmetric drop shape analysis (ASDA), which determines the interfacial energy from the profile of a pendant drop using digital image processing, is now the state-of-art method [Río and Neumann, 1997; Song and Springer, 1996a,b], it fails in situations where the difference in density of the used liquids is low. The drop weight method is less accurate, but will perform well even in these cases.

A drop of a fluid is slowly formed at the tip of a capillary. When the volume of the drop exceeds a certain limit, the drop detaches from the tip. This happens when the interfacial tension at the rim cannot support the drop weight anymore. The

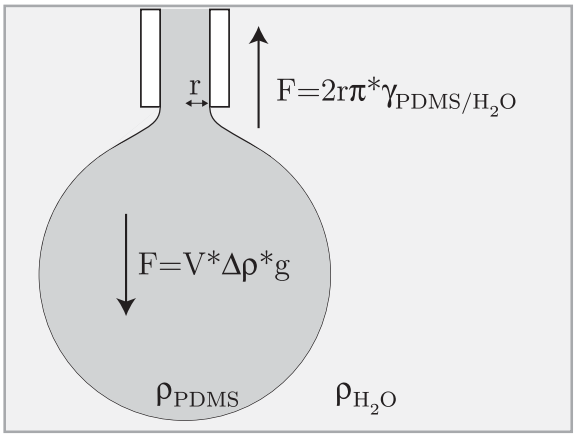

Figure C.1: Sketch of the setup used for determining the interfacial energy by the drop weight method. The equilibrium of forces that act at the rim of the drop shortly before detachment is used to calculate the interfacial energy.

equilibrium of forces before detachment can then be used to calculate the interfacial tension (see Fig. C.1):

$$2r\pi\ \gamma_{PDMS/H_2O} \;=\; V_{max}\ \Delta\rho\ g \qquad \text{with} \quad \Delta\rho = \rho_{H_2O} - \rho_{PDMS} \tag{C.1}$$

Here r is the inner radius of the tip, γ_{PDMS/H_2O} is the interfacial energy between the two phases, V_{max} is the maximal volume of the drop as measured shortly before

detachment, and $\Delta\rho = \rho_{H_2O} - \rho_{PDMS}$ is the difference in density between the two phases.

Not the whole volume that expands out of the tip will separate and form the falling drop; a part of the drop will either stay attached to the tip or will disintegrate into small satellite drops. This effect has been first dealt with in detail by Harkins and Brown [1919] who introduced a correction term Ψ int the form $\Psi = f(r/V^{1/3})$:

$$\Psi\, 2r\pi\, \gamma_{PDMS/H_2O} \;=\; V\, \Delta\rho\, g \tag{C.2}$$

where V is the liquid detached from the tip.

The correction term Ψ is regarded to be independent of the used liquids and several empirical correlations for it have been established [Boucher and Evans, 1975; Gunde et al., 2001; Lando and Oakley, 1967; Wilkinson and Kidwell, 1971]. For the measurement of the interfacial tension between PDMS oil and water the correlation of Zhang and Mori [1993] was used as it gives a good fit to a multitude of measured data without introducing too many independent factors:

$$\Psi \;=\; 0.6 + 0.4\left(1 - \frac{r}{V^{1/3}}\right) \tag{C.3}$$

The correction factor for the performed measurements was in the region of $\Psi \sim 0.96$.

To measure the interfacial tension between two different batches of PDMS oil (DMS-T21, DMS-T22 + 0.1% YBD-125) and water a tensiometer setup (DSA-10, Krüss, Hamburg, Germany) was used. A glass container was filled with the respective PDMS oil and a capillary (teflon, $r = 0.25\,\mathrm{mm}$, Krüss, Hamburg, Germany) connected to a water reservoir (double deionised water, Millipore, Molsheim, France) was immersed so that the tip ended beneath the water surface. Now water was pumped out of the tip with a very slow speed ($v = 25\,\mu\mathrm{l/min}$). The maximal drop volume was read from the digital volume control of the tensiometer at the time of detachment. The volume of up to seven drops was measured for each of the two tested substances.

Images of the capillary taken with the digital camera of the tensiometer were used to calculate the inner diameter of the tip from the known outer diameter. Values for the respective densities were taken from the manufacturer (see Table 4.1).

The values of the measured interfacial energies are:

$$\gamma \;=\; 36.8 \pm 1.4\,\mathrm{mJ/m^2} \quad \text{for DMS-T21} \tag{C.4}$$

$$\gamma \;=\; 27.7 \pm 1.7\,\mathrm{mJ/m^2} \quad \text{for DMS-T22 + 0.1\% YBD-125} \tag{C.5}$$

Even though the scatter in the volume data is considerable, the measured value $\gamma = 36.8 \pm 1.4\,\mathrm{mJ/m^2}$ of the interfacial energy of the pure polydimethylsiloxane DMS-T21 against water is close to $\gamma = 38.4\,\mathrm{mJ/m^2}$ as measured by Reiter and Khanna [2000]. This agreement of data strongly supports the validity of the above measurements.

Appendix D

Diffusion Measurements – Continuous Bleaching

Continuous bleaching is a convenient technique to measure diffusion coefficients in two dimensions using a standard fluorescence microscope setup. It was introduced by Dietrich et al. [Dietrich et al., 1997; Dietrich and Tampe, 1995] to measure the diffusion coefficient of a fluorescently labelled lipid membrane.

The aperture of the microscope defines an area within the object plane that is continuously and homogenously illuminated. This results in photobleaching of the dye molecules and a continuous decrease in brightness. Nevertheless unbleached dye molecules will diffuse into the illuminated area and thus lead to a spatial concentration profile at the edges of the illuminated area.

In this type of experiment, the diffusion equation Eq. 3.32 for the visible molecules has to be extended by an additional term which describes photobleaching:

$$\frac{\mathrm{d}c(x,y)}{\mathrm{d}t} = D \cdot \nabla^2 c(x,y) - B(x,y) \cdot c(x,y) \tag{D.1}$$

where c denotes the concentration of tracers, D is the diffusion constant, and $B(x,y)$ is the rate of photobleaching, which is dependent on the light intensity, the chemical nature of the dye and its environment. In the experiments performed in this study, photobleaching can be treated as a stochastic decomposition process with a constant decomposition rate B_0.

Assuming an illuminated half-plane and a constant B_0, the concentration $c(x,t)$ of dyes within the illuminated area after long times can be written as

$$c(x,t) = A(t) \cdot e^{-\frac{x}{\lambda}} + e^{-B_0 \cdot t} \tag{D.2}$$

where

$$\lambda = \sqrt{\frac{D}{B_0}} \tag{D.3}$$

is the characteristic decay length and x is the distance from the edge. Note that only the form of the profile is stationary (exponential with a decay length λ), whereas

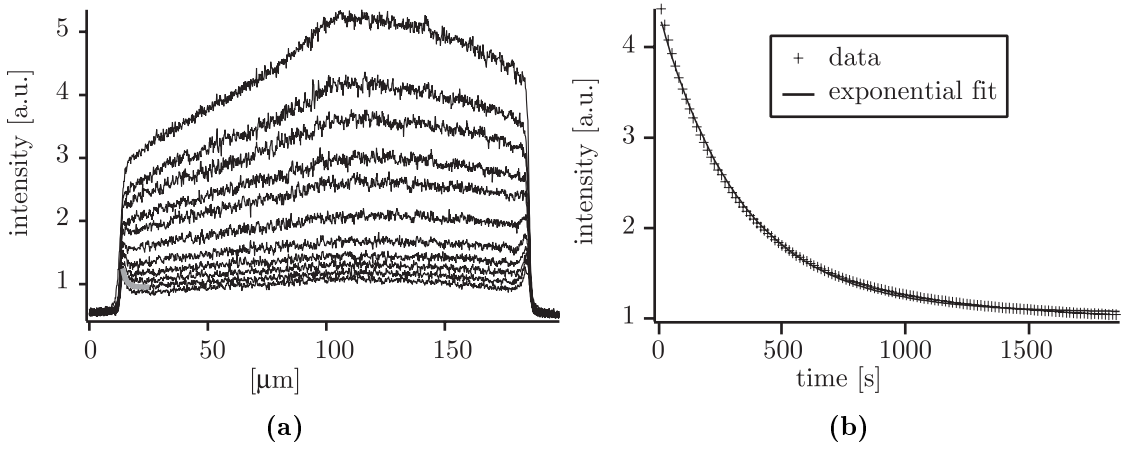

Figure D.1: a) Line profiles across the illuminated area taken at different times. The overall decrease in intensity is clearly visible. The decay at the rim at large times allows an exponential fit (grey line) to determine λ.
b) The average brightness of a small area at the center of the illuminated substrate is evaluated for different times. The bleaching rate B_0 is determined as the decay rate of the exponential fit.

the coefficient $A(t)$ never approaches a stationary value. If the bleaching rate B_0 is known, the diffusion constant D can be calculated from the decay length λ.

In these experiments the bleaching rate B_0 was taken from the decrease in average brightness at a region ($\sim 500\,\mu\text{m}^2$) at the center of the aperture area (see Fig. D.1(b)). The decay length λ was then extracted from the exponential decrease of fluorescence intensity at the rim (see Fig. D.1(a)). The average brightness and the line profiles were extracted with the imaging software Open Box.

To evaluate the diffusion coefficient of fluid PDMS, flourescently labelled PDMS was used. Aminopropyl terminated PDMS (DMS-A21, Gelest, ABCR, Karlsruhe) was labelled with TRITC (tetramethylrhodamine isothiocyanate) by Bernd Hoffmann (Forschungszentrum Jülich, Germany). Approximately every sixth endgroup was labelled.

The labelled PDMS was then diluted with PDMS of the same viscosity (DMS-T21) and deposited onto the substrate of cross-linked PDMS with long cross-linker with a thin hypodermic needle (Sterican, Size 18, $0.45\times25\,\text{mm}$, Braun, Melsungen) in air. Afterwards millipore water was put on top of this with the sample holder being held in a tilted position. This was done to avoid smearing out the drop of PDMS with the flow of the water. Only the region of the substrate that was immersed before the water reached the drop was used for any measurements.

The self diffusion constant of the fluid PDMS was determined at the middle of a drop where the fluid PDMS was resting on top of the substrate. The so determined value of $D_S = 39 \pm 9\,\mu\text{m}^2/\text{s}$ matches the order of magnitude of data from literature (app. $30\,\mu m^2/s$ for a PDMS oil of comparable viscosity [Cosgrove et al., 1996]).

The diffusion constant was measured on three substrates at eight different spots,

which were all within 50–200 μm distance of the respective drops. The resulting value was determined to be $D = 3.5 \pm 0.8\,\mu m^2/s$. This is in good agreement with data from literature for the diffusion constant in cross-linked networks D_{NW}. Garrido et al. [1988] measured the diffusion of PDMS in a polymer network of cross-linked PDMS with the pulsed field gradient NMR technique and determined diffusion coefficients of around $D_{NW} = 3.3\,\mu m^2/s$ for systems of similar dimensions. Mazan et al. [1995] measured a diffusion constant for a similar system of $D_{NW} = 2.64 \pm 0.02\,\mu m^2/s$.

This indicates that the drop of PDMS deposited onto a substrate of cross-linked PDMS loses volume by diffusing into the substrate rather than forming a precursor that moves on top of the substrate.

Appendix E

Tables of Experimental Quantities

PDMS Used for the Drop	Cross-linker Used for the Substrate	Experiment Numbers
DMS-T22 with Polar Fraction	DMS-V31, long	1–13
DMS-T22	DMS-V31, long	14–20
DMS-T22 with Polar Fraction	DMS-V21, short	21–25
DMS-T22	DMS-V21, short	26–31
DMS-T21	DMS-V31, long	32–43

Table E.1: Experiment numbers of the different sets of experiments.

Figure	Experiment Numbers
4.7	4
4.8	4
5.14	15
5.17	34
5.19	15
5.20	15
5.21	3
5.23	12
5.24	12
5.25	12

Figure	Experiment Numbers
6.1	36
6.2	15
6.4	15
6.5	3, 7, 12, 1, 2
6.6	42, 41, 36, 40, 35
6.8	a)-b) 34 c)-d) 42
6.9	a) 8, b) 9, c) 12, d) 6

Figure	Experiment Numbers
6.11	a) 26, b) 34, c) 36
6.12	7
6.13	7
6.14	33, 37, 36, 34, 38, 32, 35
6.15	27, 31, 22, 30, 28, 24, 21, 26
6.16	19
6.18	a) 4, b) 4, c) 26, d) 15

Table E.2: Experiment numbers of all figures shown in this work. If data from more than one experiment is shown in the graph, the respective experiment numbers are listed from top to bottom.

Experiment Number	Initial Radius [µm]	Initial Angle [°]	Initial Volume [fl]	Ratio a/b $t = 0\,\mathrm{s}$	Ratio a/b $t = 60\,\mathrm{s}$	Time of reversal t_r [s]	Maximum Radius R_r [µm]	B ($\theta \propto t^B$)
1	13.1	7.1	126	1.08	1.04	56	19.3	-0.334 ± 0.004
2	7.2	6.7	56	1.02	1.05	29	9.8	-0.314 ± 0.011
3	44.4	5.4	70960	1.16	1.09	2409	63.1	-0.329 ± 0.007
6	9.1	3.9	38	1	1	52.09	9.7	-0.289 ± 0.011
7	30.3	5.3	1945	1.01	1.01	560	39.3	-0.280 ± 0.003
8	37.6	2.4	13313	1.01	1.01	1387	54.8	-0.426 ± 0.008
9	24.0	5.7	4947	1.1	1.06	423	36.8	-0.340 ± 0.010
12	21.7	8.1	743	1	1.01	104.4	27.2	-0.243 ± 0.007
13	26.1	10.3	1407	1.01	1.01	716	40.3	-0.295 ± 0.009
14	46.0	3.4	3863	1.03	1.01	3800	50.9	-0.210 ± 0.005
15	28.0	6.2	1875	1.03	1.02	369	34.7	-0.220 ± 0.007
16	26.9	6.1	1727	1.03	1.01	491	36	-0.329 ± 0.006
18	13.5	11.2	559	1.05	1.04	66	16	-0.329 ± 0.015
19	15.9	8.5	1200	1.03	1.02	332	17.8	-0.313 ± 0.023
20	14.0	9.3	223	1.07	1.06	96	15.3	-0.324 ± 0.027
21	20.8	6.3	26	1.04	1.02	11	24.5	-0.125 ± 0.004
22	20.8	12.1	1560	1.01	1.01		21.8	-0.0370 ± 0.0008
23	21.6	11.2	665	1.01	1.01	48	29.5	
24	24.6	6.9	1798	1.01	1.01	1316	27	-0.0574 ± 0.0020

Table E.3

Experiment Number	Initial Radius [µm]	Initial Angle [°]	Initial Volume [fl]	Ratio a/b $t = 0\,\mathrm{s}$	Ratio a/b $t = 60\,\mathrm{s}$	Time of reversal t_r [s]	Maximum Radius R_r [µm]	B ($\theta \propto t^B$)
26	31.4	4.6	2326	1.04	1.03	471	33.1	-0.088793 ± 0.0023
27	32.2	15.8	8585	1.04	1.04	1505	34.3	-0.031264 ± 0.003
28	16.6	9.8	1147	1.01	1.02	8	18.9	-0.057777 ± 0.004
30	22.2	10.9	1332	1.01	1.01	33	22.7	-0.021522 ± 0.0021
31	14.2	14.5	446	1.01	1.01	10	14.6	-0.026233 ± 0.0018
32	10.2	4.6	54.7	1	1	39	11	-0.294 ± 0.011
33	21.5	8.6	996	1.01	1	365	26.8	-0.2319 ± 0.0026
34	9.0	7.8	84	1.06	1.02	24	11.7	-0.342 ± 0.004
35		4.3	86	1.05	1			-0.379 ± 0.012
36	14.5	6.6	331	1.02	1.01	72	17.7	-0.3164 ± 0.0018
37	13.7	9.6	84.4	1	1.01	85	17.6	-0.3077 ± 0.0026
38	9.4	6.7	115	1.01	1.02	26	11.3	-0.294 ± 0.007
39	14.0	14.3	541	1.06	1.05	340	14.9	
40	12.8	13.1	140	1.03	1.04	229	13.9	
41	13.9	12.1	522	1.02	1.02	276	15.2	
42	15.5	10.7	790	1.02	1	400	15.8	
43	13.9	12.9	940	1.03	1.02	315	14.3	

Table E.4

Bibliography

A. W. Abercrombie and E. J. Ambrose. Interference reflection microscopy studies of cell contacts in tissue culture. *Experimental Cell Research*, 15(2):332–345, 1958.

M. Abramowitz and I. A. Stegun. *Pocketbook of Mathematical Functions*. Harri Deutsch, Frankfurt am Main, 1984.

U. Albrecht, A. Otto, and P. Leiderer. Two-dimensional liquid polymer diffusion: Experiment and simulation. *Physical Review Letters*, 68(21):3192–3195, 1992.

D. Ausserré, A. M. Picard, and L. Leger. Existence and role of the precursor film in the spreading of polymer liquids. *Physical Review Letters*, 57(21):2671–2674, 1986.

L. Bacri and F. Brochard-Wyart. Droplet suction on porous media. *The European Physical Journal E - Soft Matter*, 3(1):87–97, 2000.

L. Bacri and F. Brochard-Wyart. Dewetting on porous media. *Europhysics Letters*, 56(3):414–419, 2001.

G. Beaucage, S. Sukumaran, and S. J. Clarson. Symmetric, isotopic blends of poly(dimethylsiloxane). *Macromolecules*, 29(26):8349–8356, 1996.

A. Be'er and Y. Lereah. Time-resolved, three-dimensional quantitative microscopy of a droplet spreading on solid substrates. *Journal of Microscopy*, 208(2):148–152, 2002.

J. C. Berg. Role of acid-base interactions in wetting and related phenomena. In J. C. Berg, editor, *Wettability*. Marcel Dekker, Inc., Seattle, Washington, 1993a.

J. C. Berg, editor. *Wettability*. Marcel Dekker, Inc, Seattle, Washington, 1993b.

M. V. Berry. Waves amd Thom's theorem. *Advances in Physics*, 25(1):1–16, 1976.

B. P. Binks, J. F. Dong, and N. Rebol. Equilibrium phase behaviour and emulsion stability in silicone oil plus water plus AOT mixtures. *Physical Chemistry Chemical Physics*, 1(9):2335 – 2344, 1999.

T. D. Blake. Dynamic contact angles and wetting kinetics. In J. C. Berg, editor, *Wettability*. Marcel Dekker, Inc., Seattle, Washington, 1993.

T. D. Blake, A. Clarke, J. De Coninck, and M. J. de Ruijter. Contact angle relaxation during droplet spreading: Comparison between molecular kinetic theory and molecular dynamics. *Langmuir*, 13(7):2164 – 2166, 1997.

T. D. Blake and J. D. Coninck. The influence of pore wettability on the dynamics of imbibition and drainage. *Colloids and Surfaces A: Physicochemical and Engineering Aspects*, 250(1-3):395–402, 2004.

C. J. Bolgers and A. S. Michaels, editors. *Interface Conversion for Polymer Coatings*. Elsevier, New York, 1968.

M. Born and E. Wolf. *Principles of Optics*. Pergamon Press, Oxford, 6^{th} edition, 1980.

E. A. Boucher and M. J. B. Evans. Pendent drop profiles and related capillary phenomena. *Proceedings of the Royal Society of London Series A-Mathematical Physical and Engineering Sciences*, 346(1646):349–374, 1975.

E. A. Boucher and H. J. Kent. Capillary phenomena VII. Equilibrium and stability of pendent drops. *Journal of Colloid and Interface Science*, 67(1):10–15, 1978.

F. Brochard-Wyart, J. M. Di Meglio, D. Quere, and P. G. De Gennes. Spreading of nonvolatile liquids in a continuum picture. *Langmuir*, 7(2):335 – 338, 1991.

I. C. Callaghan, D. H. Everett, and A. J. P. Fletcher. Liquid/liquid/solid contact angles measured by interference microscopy. *Journal of the Chemical Society - Faraday Transactions I*, 79(11):2723–2728, 1983.

A. Carré, J. C. Gastel, and M. E. R. Shanahan. Viscoelastic effects in the spreading of liquids. *Nature*, 379:432 – 434, 1996.

H. S. Carslaw and J. C. Jaeger. Some two-dimensional problems in conduction of heat with circular symmetry. *London Mathematical Society. Proceedings.*, 46: 361–388, 1940.

A. M. Cazabat, N. Fraysse, F. Heslot, and P. Carles. Spreading at the microscopic scale. *Journal of Physical Chemistry*, 94(19):7581 – 7585, 1990.

A. M. Cazabat, S. Gerdes, M. P. Valignat, and S. Villette. Dynamics of wetting: From theory to experiment. *Interface Science*, 5(2-3):129–139, 1997.

M. K. Chaudhury and G. M. Whitesides. Direct measurement of interfacial interactions between semispherical lenses and flat sheets of poly(dimethylsiloxane) and their chemical derivatives. *Langmuir*, 7(5):1013–1025, 1991.

J. D. Chen and N. Wada. Wetting dynamics of the edge of a spreading drop. *Physical Review Letters*, 62(26):3050–3053, 1989.

E. Chibowski. Surface free energy of a solid from contact angle hysteresis. *Advances in Colloid and Interface Science*, 103(2):149–172, 2003.

E. Chibowski and R. Perea-Carpio. Problems of contact angle and solid surface free energy determination. *Advances in Colloid and Interface Science*, 98(2):245–264, 2002.

A. Clarke, T. D. Blake, K. Carruthers, and A. Woodward. Spreading and imbibition of liquid droplets on porous surfaces. *Langmuir*, 18(8):2980 –2984, 2002.

A. E. Conrady. *Applied Optics and Optical Design, Part I.* Oxford University Press; Dover Publications, 1957.

T. Cosgrove, M. J. Turner, P. C. Griffiths, J. Hollingshurst, M. J. Shenton, and J. A. Semlyen. Self-diffusion and spin-spin relaxation in blends of linear and cyclic polydimethylsiloxane melts. *Polymer*, 37(9):1535–1540, 1996.

J. Crank. *The mathematics of diffusion.* Clarendon Press, Oxford, 2^{nd} edition, 1975.

H. Darcy. *Les fontaines publiques de la ville de Dijon.* Dalmont, Paris, 1856.

P. G. de Gennes. Wetting: statics and dynamics. *Reviews of Modern Physics*, 57 (3):827–863, 1985.

M. J. de Ruijter, M. Charlot, M. Voué, and J. De Coninck. Experimental evidence of several time scales in drop spreading. *Langmuir*, 16(5):2363–2368, 2000.

M. J. de Ruijter, J. De Coninck, and G. Oshanin. Droplet spreading: Partial wetting regime revisited. *Langmuir*, 15(9):2209–2216, 1999.

C. Della Volpe, D. Maniglio, M. Brugnara, S. Siboni, and M. Morra. The solid surface free energy calculation: I. In defense of the multicomponent approach. *Journal of Colloid and Interface Science*, 271(2):434–453, 2004.

C. Della Volpe, D. Maniglio, S. Siboni, and M. Morra. Recent theoretical and experimental advancements in the application of van Oss-Chaudury-Good acid-base theory to the analysis of polymer surfaces - I. General aspects. *Journal of Adhesion Science and Technology*, 17(11):1477–1505, 2003.

B. Demé, D. Hess, M. Tristl, L.-T. Lee, and E. Sackmann. Binding of actin filaments to charged lipid monolayers: Film balance experiments combined with neutron reflectivity. *The European Physical Journal E - Soft Matter*, 2(2):125–136, 2000.

M. Denesuk, G. L. Smith, B. J. J. Zelinski, N. J. Kreidl, and D. R. Uhlmann. Capillary penetration of liquid droplets into porous materials. *Journal of Colloid and Interface Science*, 158(1):114–120, 1993.

C. Dietrich, R. Merkel, and R. Tampe. Diffusion measurement of fluorescence-labeled amphiphilic molecules with a standard fluorescence microscope. *Biophysical Journal*, 72:1701–1710, 1997.

C. Dietrich and R. Tampe. Charge determination of membrane molecules in polymer-supported lipid layers. *Biochimica et Biophysica Acta*, 1238:183–191, 1995.

C. J. Drummond and D. Y. C. Chan. Van der Waals interaction, surface free energies, and contact angles: Dispersive polymers and liquids. *Langmuir*, 13(14): 3890 – 3895, 1997.

A. Einstein. Über die von der molekularkinetischen Theorie der Wärme geforderte Bewegung von in ruhenden Flüssigkeiten suspendierten Teilchen. *Annalen der Physik*, IV(17):549–560, 1905.

C. W. Extrand. A thermodynamic model for contact angle hysteresis. *Journal of Colloid and Interface Science*, 207(1):11–19, 1998.

J. Felber, R. Gähler, R. Golub, and K. Prechtel. Coherence volumes and neutron scattering. *Physica B*, 252:34–43, 1998.

A. Fick. Ueber Diffusion. *Annalen der Physik*, 170:59–86, 1855.

F. M. Fowkes, D. C. McCarthy, and M. A. Mostafa. Contact angles and the equilibrium spreading pressures of liquids on hydrophobic solids. *Journal of Colloid and Interface Science*, 78(1):200–206, 1980.

L. Garrido, J. E. Mark, J. L. Ackerman, and R. A. Kinsey. Studies of self-diffusion of poly(dimethylsiloxane) chains in PDMS model networks by pulsed field gradient NMR. *Journal of Polymer Science Part B: Polymer Physics*, 26(11):2367–2377, 1988.

C. Gerthsen. *Gerthsen Physik*. Springer, Berlin, 19^{th} edition, 1997.

J. W. Gibbs. *Gibbs, The Collected Works of J. Willard Gibbs*, volume 1. Yale Univ. Press, New Haven, 1928.

D. Gingell and I. Todd. Interference reflection microscopy. A quantitative theory for image interpretation and its application to cell-substratum separation measurement. *Biophys. J.*, 26(3):507–526, 1979.

S. Goldstein. Some two-dimensional diffusion problems with circular symmetry. *Proceedings of the London Mathematical Society*, XXXIV:51–88, 1931.

M. Graessmann and A. Graessmann. Microinjection of tissue culture cells. In *Methods in Enzymology*, volume 101, pages 482–492. 1983.

Y. Gu. Drop size dependence of contact angles of oil drops on a solid surface in water. *Colloids and Surfaces A-Physicochemical and Engineering Aspects*, 181 (1-3):215–224, 2001.

R. Gunde, A. Kumar, S. Lehnert-Batar, R. Mader, and E. J. Windhab. Measurement of the surface and interfacial tension from maximum volume of a pendant drop. *Journal of Colloid and Interface Science*, 244(1):113–122, 2001.

S. Haferl, D. Poulikakos, and Z. Zhao. Employing scanning force microscopy to investigate the free surface of liquid microstructures and their wetting behavior on smooth surfaces: Gathered experiences. *Experimental Heat Transfer*, 14(1): 1–25, 2001.

H. G. Hansma and J. H. Hoh. Biomolecular imaging with the atomic force microscope. *Annual Review of Biophysics and Biomolecular Structure*, 23:115–140, 1994.

W. D. Harkins and F. E. Brown. The determination of surface tension (free surface energy), and the weight of falling drops: The surface tension of water and benzene by the capillary height method. *Journal of the American Chemical Society*, 41(4): 499–524, 1919.

E. Hecht. *Optik*. Oldenbourg, München, 3^{rd} edition, 2001.

F. Heslot, A. M. Cazabat, and P. Levinson. Dynamics of wetting of tiny drops: Ellipsometric study of the late stages of spreading. *Physical Review Letters*, 62 (11):1286–1289, 1989.

H. Hillborg, J. F. Ankner, U. W. Gedde, G. D. Smith, H. K. Yasuda, and K. Wikstrom. Crosslinked polydimethylsiloxane exposed to oxygen plasma studied by neutron reflectometry and other surface specific techniques. *Polymer*, 41(18): 6851–6863, 2000.

J. N. Israelachvili. *Intermolecular and Surface Forces*. Academic Press Inc., London, 1985.

J. C. Jaeger. Heat flow in the region bounded internally by a circular cylinder. *Proceedings of the Royal Society Edinburgh A*, 61:223–228, 1942.

J. C. Jaeger and M. Clarke. A short table of I(0,1,x). *Proceedings of the Royal Society Edinburgh A*, 61:229–230, 1942.

J. F. Joanny and P. G. de Gennes. A model for contact angle hysteresis. *Journal of Chemical Physics*, 81(1):552–562, 1984.

R. E. Johnson and R. H. Dettre. Wetting of low-energy surfaces. In J. C. Berg, editor, *Wettability*. Marcel Dekker, Inc., Seattle, Washington, 1993.

M. Keller, J. Schilling, and E. Sackmann. Oscillatory magnetic bead rheometer for complex fluid microrheometry. *Review of Scientific Instruments*, 72(9):3626–3634, 2001.

M. Kühner. *Präparation und Charakterisierung von Polysaccharid- Monofilmen, Lipid-Doppelschichten und Polysaccharid-Lipid-Verbundfilmen auf Festkörperoberflächen*. Dissertation, Technische Universität München, 1996.

S. Kim, G. Y. Choi, A. Ulman, and C. Fleischer. Effect of chemical functionality on adhesion hysteresis. *Langmuir*, 13:6850–6856, 1997.

D. Y. Kwok and A. W. Neumann. Contact angle interpretation in terms of solid surface tension. *Colloids and Surfaces A: Physicochemical and Engineering Aspects*, 161(1):31–48, 2000.

L. M. Lander, L. M. Siewierski, W. J. Brittain, and E. A. Vogler. A systematic comparison of contact angle methods. *Langmuir*, 7(8):2237 – 2239, 1993.

J. L. Lando and H. T. Oakley. Tabulated correction factors for the drop-weight-volume determination of surface and interracial tensions. *Journal of Colloid and Interface Science*, 25(4):526–530, 1967.

L. Leger, M. Erman, A. M. Guinet-Picard, D. Ausserre, and C. Strazielle. Precursor film profiles of spreading liquid drops. *Physical Review Letters*, 60(23):2390–2393, 1988.

L. Leger and J. F. Joanny. Liquid spreading. *Reports on Progress in Physics*, 55(4): 431–486, 1992.

R. J. LeVeque, D. Mihalas, E. A. Dorfi, and E. Müller, editors. *Computational Methods for Astrophysical Fluid Flow*, volume 27 of *Saas-Fee Advanced Courses*. Springer, Heidelberg, 1998.

T. Lindl and J. Bauer. *Zell- und Gewebekultur*. Gustav Fischer Verlag, 3^{rd} edition, 1994.

F. Linke. *Development of Ellipsometric Microscopy as a Quantitative High-Resolution Technique for the Investigation of Thin Films at Glass-Water and Silicon-Air Interfaces*. Dissertation, Technische Universität, 2004.

J. Lyklema. The surface tension of pure liquids: Thermodynamic components and corresponding states. *Colloids and Surfaces A: Physicochemical and Engineering Aspects*, 156(1-3):413–421, 1999.

F. Malchiodi-Albedi, A. Morgillo, G. Formisano, S. Paradisi, R. Perilli, G. C. Scalzo, G. Scorcia, and S. Caiazza. Biocompatibility assessment of silicone oil and perfluorocarbon liquids used in retinal reattachment surgery in rat retinal cultures. *Journal of Biomedical Material Research*, 60(4):548–555, 2002.

V. Marchi-Artzner, B. Lorz, U. Hellerer, M. Kantlehner, H. Kessler, and E. Sackmann. Selective adhesion of endothelial cells to artificial membranes with a synthetic RGD-lipopeptide. *Chemistry-a European Journal*, 7(5):1095–1101, 2001.

A. Marmur. Line tension and the intrinsic contact angle in solid-liquid-fluid systems. *Journal of Colloid and Interface Science*, 186(2):462–466, 1997.

P. Martin, A. Buguin, and F. Brochard-Wyart. Bursting of a liquid-film on a liquid substrate. *Europhysics Letters*, 28(6):421–426, 1994.

S. Marx, J. Schilling, E. Sackmann, and R. Bruinsma. Helfrich repulsion and dynamical phase separation of multicomponent lipid bilayers. *Physical Review Letters*, 88(13), 2002.

L. Masaro and X. X. Zhu. Physical models of diffusion for polymer solutions, gels and solids. *Progress in Polymer Science*, 24:731–775, 1999.

J. Mazan, B. Leclerc, N. Galandrin, and G. Couarraze. Diffusion of free polydimethylsiloxane chains in polydimethylsiloxane elastomer networks. *European Polymer Journal*, 31(8):803–807, 1995.

G. McHale, H. Y. Erbil, M. I. Newton, and S. Natterer. Analysis of shape distortions in sessile drops. *Langmuir*, 17(22):6995–6998, 2001.

A. I. Milchev and A. A. Milchev. Wetting behavior of nanodroplets: The limits of Young's rule validity. *Europhysics Letters*, 56(5):695–701, 2001.

P. Müller-Buschbaum. Influence of surface cleaning on dewetting of thin polystyrene films. *The European Physical Journal E - Soft Matter*, 12(3):443–448, 2003.

I. D. Morrison. Does the phase rule for capillary systems really justify an equation of state for interfacial tensions? *Langmuir*, 7(8):1833 – 1836, 1991.

P. Nelson. Random walks, friction and diffusion. In *Biological Physics : Energy, Information, Life*, pages 108–157. W H Freeman & Co., 2003.

M. I. Newton, G. McHale, S. M. Rowan, and M. Banerjee. A surface acoustic wave technique for the observation of dynamic wetting. *Journal of Physics D: Applied Physics*, 28(9):1930–1936, 1995.

J. Nissen, S. S. Gritsch, G. Wiegand, and J. O. Rädler. Wetting of phospholipid membranes on hydrophilic surfaces - concepts towards self-healing membranes. *The European Physical Journal B - Condensed Matter*, 10(2):335 – 344, 1999.

M. A. Olshanskii and A. Reusken. Convergence analysis of a multigrid method for a convection-dominated model problem. *SIAM Journal on Numerical Analysis*, 42(3):1261–1291, 2004.

J. S. Ploem. Reflection contrast microscopy as a tool for investigation of the attachment of living cells to a glass surface. In *Mononuclear Phagocytes in Immunity, Infection, Pathology*. Blackwell Scientific Publications, Oxford, 1975.

M. Pluta. *Principles and Basic Properties*, volume 1 of *Advanced Light Microscopy*. Elsevier Science Publishers, Amsterdam, 1988.

A. Pouchelon, C. George, and P. Menez. The swelling behaviour of siloxane elastomers in relation to their microscopic structure. *Macromolecular Symposia*, 171 (1):233–242, 2001.

W. H. Press, B. P. Flannery, S. A. Teukolsky, and W. T. Vetterling. *Numerical Recipes in Fortran 77: The Art of Scientific Computing*, volume 1 of *Fortran Numerical Recipes*. Press Syndicate of the University of Cambridge, Cambridge, 2^{nd} edition, 1992.

H. Radelczuk, L. Holysz, and E. Chibowski. Comparison of the Lifshitz-van der Waals/acid-base and contact angle hysteresis approaches for determination of solid surface free energy. *Journal of Adhesion Science and Technology*, 16(12): 1547–1568, 2002.

J. Rädler and E. Sackmann. Imaging optical thicknesses and separation distances of phospholipid vesicles at solid surfaces. *Journal de Physique II*, 3(5):727–748, 1993.

K. Razi Naqvi. Diffusion-controlled reactions in two-dimensional fluids: discussion of measurements of lateral diffusion of lipids in biological membranes. *Chemical Physics Letters*, 28(2):280–284, 1974.

G. Reiter and R. Khanna. Enhanced instability in thin liquid films by improved compatibility. *Physical Review Letters*, 85(7):1432–1435, 2000.

O. I. Río and A. W. Neumann. Axisymmetric drop shape analysis: Computational methods for the measurement of interfacial properties from the shape and dimensions of pendant and sessile drops. *Journal of Colloid and Interface Science*, 196 (2):136–147, 1997.

P. Roura and J. Fort. Local thermodynamic derivation of Young's equation. *Journal of Colloid and Interface Science*, 272(2):420–429, 2004.

B. B. Sauer and G. T. Dee. Molecular weight and temperature dependence of polymer surface tension: comparison of experiment with theory. *Macromolecules*, 24(8):2124 – 2126, 1991.

L. J. M. Schlangen, L. K. Koopal, M. Stuart, and J. Lyklema. Wettability - thermodynamic relationships between vapor adsorption and wetting. *Colloids And Surfaces A-Physicochemical And Engineering Aspects*, 89(2-3):157–167, 1994.

J. Schoelkopf, P. A. C. Gane, C. J. Ridgway, and G. P. Matthews. Practical observation of deviation from Lucas-Washburn scaling in porous media. *Colloids and Surfaces A: Physicochemical and Engineering Aspects*, 206(1-3):445–454, 2002.

M. E. R. Shanahan and A. Carre. Glissement de gouttes de liquide sur des solides mous. *Comptes Rendus de l'Académie des Sciences - Series IV - Physics*, 1(2): 263–268, 2000.

R. N. Shimizu and N. R. Demarquette. Evaluation of surface energy of solid polymers using different models. *Journal of Applied Polymer Science*, 76(12):1831–1845, 2000.

C.-W. Shu. Essentially non-oscillatory and weighted essentially non-oscillatory schemes for hyperbolic conservation laws. *ICASE Technical Reports*, 97-65, 1997.

S. Siboni, C. Della Volpe, D. Maniglio, and M. Brugnara. The solid surface free energy calculation: II. The limits of the Zisman and of the "equation-of-state" approaches. *Journal of Colloid and Interface Science*, 271(2):454–472, 2004.

P. Silberzan, S. Perutz, E. J. Kramer, and M. K. Chaudhury. Study of the self-adhesion hysteresis of a siloxane elastomer using the JKR method. *Langmuir*, 10: 2466–2470, 1994.

B. Song and J. Springer. Determination of interfacial tension from the profile of a pendant drop using computer-aided image processing. 1. Theoretical. *Journal of Colloid and Interface Science*, 184(1):64–76, 1996a.

B. Song and J. Springer. Determination of interfacial tension from the profile of a pendant drop using computer-aided image processing. 2. Experimental. *Journal of Colloid and Interface Science*, 184(1):77–91, 1996b.

M. Spiegelman. *Myths & Methods in Modelling*. Lecture Notes. Columbia University, 2000.

V. M. Starov, S. R. Kostvintsev, V. D. Sobolev, M. G. Velarde, and S. A. Zhdanov. Spreading of liquid drops over dry porous layers: Complete wetting case. *Journal of Colloid and Interface Science*, 252(2):397–408, 2002a.

V. M. Starov, S. R. Kosvintsev, V. D. Sobolev, M. G. Velarde, and S. A. Zhdanov. Spreading of liquid drops over saturated porous layers. *Journal of Colloid and Interface Science*, 246(2):372–379, 2002b.

V. M. Starov, S. A. Zhdanov, S. R. Kosvintsev, V. D. Sobolev, and M. G. Velarde. Spreading of liquid drops over porous substrates. *Advances in Colloid and Interface Science*, 104(1-3):123–158, 2003.

F. Steinmaßl. *Benetzung in Flüssig-Flüssig-Substrat-Systemen: Eine mikroskopische Untersuchung der Ausbreitung von Decan auf modifizierten Substraten unter Wasser.* Diploma thesis, 2000.

L. H. Tanner. The spreading of silicone oil drops on horizontal surfaces. *Journal of Physics D: Applied Physics*, 12(9):1473, 1979.

L. P. Thomas, R. Gratton, B. M. Marino, and J. A. Diez. Droplet profiles obtained from the intensity distribution of refraction patterns. *Applied Optics*, 34(25): 5840–5848, 1995.

C. J. Van Oss, R. F. Giese, Z. Li, K. Murphy, J. Norris, M. K. Chaudhury, and R. J. Good. Determination of contact angles and pore sizes of porous-media by column and thin-layer wicking. *Journal of Adhesion Science and Technology*, 6 (4):413–428, 1992.

C. J. Van Oss, R. J. Good, and M. K. Chaudhury. Additive and nonadditive surface tension components and the interpretation of contact angles. *Langmuir*, 4(4): 884–891, 1988.

R. D. Vold and M. J. Vold. *Colloid and Interface Chemistry.* Addison-Wesley Publishing Company, Inc., Reading, Massachusetts, 1983.

E. Waluschka. Polarization ray trace. *Optical Engineering*, 28(2):86–89, 1989.

E. W. Washburn. The dynamics of capillary flow. *The Physical Review*, 17(3): 273–283, 1921.

G. Wiegand, T. Jaworek, G. Wegner, and E. Sackmann. Studies of structure and local wetting properties on heterogeneous, micropatterned solid surfaces by microinterferometry. *Journal of Colloid and Interface Science*, 196(2):299–312, 1997.

G. Wiegand, K. R. Neumaier, and E. Sackmann. Microinterferometry: three-dimensional reconstruction of surface microtopography for thin-film and wetting studies by reflection interference contrast microscopy (RICM). *Applied Optics*, 37 (29):6892–6905, 1998.

M. C. Wilkinson and R. L. Kidwell. A mathematical description of the Harkins and Brown correction curve for the determination of surface and interfacial tensions. *Journal of Colloid and Interface Science*, 35(1):114–119, 1971.

T. Yasuda, M. Miyama, and H. K. Yasuda. Effect of water immersion on surface configuration of an ethylene-vinyl alcohol copolymer. *Langmuir*, 10(2):583 – 585, 1994.

E. K. Yeh, J. Newman, and C. J. Radke. Equilibrium configurations of liquid droplets on solid surfaces under the influence of thin-film forces. Part I. Thermodynamics. *Colloids and Surfaces A: Physicochemical and Engineering Aspects*, 156(1-3):137–144, 1999a.

E. K. Yeh, J. Newman, and C. J. Radke. Equilibrium configurations of liquid droplets on solid surfaces under the influence of thin-film forces. Part II. Shape calculations. *Colloids and Surfaces A: Physicochemical and Engineering Aspects*, 156(1-3):525–546, 1999b.

I. Yildirim. *Surface Free Energy Characterization of Powders*. Dissertation, Virginia Polytechnic Institute and State University, 2001.

T. Young. *Philosophical Transactions of the Royal Society*, 95:65, 1805.

N. Zhang and D. F. Chao. Caustics and caustic-diffraction in laser shadowgraphy of a sessile drop and identification of profile near contact line. *Optics & Laser Technology*, 35(3):155–161, 2003.

Z.-Q. Zhang and Y. H. Mori. Formulation of the Harkins-Brown correction factor for drop-volume description. *Industrial & engineering chemistry research*, 32(11): 2950 – 2952, 1993.

S. A. Zhdanov, V. M. Starov, V. D. Sobolev, and M. G. Velarde. Spreading of aqueous SDS solutions over nitrocellulose membranes. *Journal of Colloid and Interface Science*, 264(2):481–489, 2003.

W. A. Zisman. Contact angle, wettability and adhesion. In R. F. Gould, editor, *Advances in Chemistry Series*, volume 43, pages 1–51. American Chemical Society, Washington, DC, 1964.

and the Thank-you goes to ...

Ein grosses Dankeschön an:

- Professor R. 'Rudi' Merkel, für seine grenzenlose Geduld als Fernbetreuer.

- Prof. Erich Sackmann und Prof. Matthias Rief, für die Möglichkeit diese Dissertation an ihrem Lehrstuhl durchzuführen.

- Motomu Tanaka, der mich an seinem besten Mikroskop arbeiten ließ.

- Felix Linke, dem besten Mitdoktoranden, für seine Simulationen, Tipps, Tricks, Spass, Spannung und für seinen gundlegenden Optimismus das Ende jeglicher Doktorabeiten betreffend.

- alle fleissigen Helfer in E22 und in Jülich: Gabi Chmel, Rudi Lehrhuber, Dirk Mayer, Bernd Hoffmann und Marianne Hanzlik.

- alle E22ger, die mit munteren Mittagsgesprächen, Tee- und Kaffeepausen für gute Stimmung sorgten.

- Sheridon for the tea. Und für die Dr. Seuss Aufkleber und unermüdliches Korrekturlesen.

- Daniel *'Doctor Acidic'*, für Erfahrungsaustausch.

- Johannas zwei liebe Omas und an Shoma, ohne deren unermüdlichen Einsatz diese Doktorarbeit nicht hätte entstehen können.

- meinen besten Ehefreund und Johanna.